RESEARCH MEMORANDUM

AN AERODYNAMIC AND HYDRODYNAMIC INVESTIGATION OF TWO MULTIJET WATER-BASED AIRCRAFT HAVING LOW TRANSONIC DRAG RISE

By Roland E. Olson and Ralph P. Bielat

Langley Aeronautical Laboratory
Langley Field, Va.

NATIONAL ADVISORY COMMITTEE
FOR AERONAUTICS

WASHINGTON

February 15, 1955
Declassified May 29, 1959

NACA RM L55A11a

NATIONAL ADVISORY COMMITTEE FOR AERONAUTICS

RESEARCH MEMORANDUM

AN AERODYNAMIC AND HYDRODYNAMIC INVESTIGATION OF TWO MULTIJET WATER-BASED AIRCRAFT HAVING LOW TRANSONIC DRAG RISE

By Roland E. Olson and Ralph P. Bielat

SUMMARY

Two multijet seaplanes for high-speed operation incorporating some recent aerodynamic and hydrodynamic research have been investigated. The aerodynamic layout of the configurations was based on a transonic-area-rule concept. Results of the wind-tunnel and tank tests have indicated that seaplane configurations can be designed which have low subsonic drag, relatively high Mach number for drag rise, low transonic drag-rise increment, and satisfactory hydrodynamic qualities.

INTRODUCTION

Recent NACA research (ref. 1) has shown that the drag rise of aircraft configurations at transonic speeds is closely related to their cross-sectional area distributions. This area rule not only has been useful in correlating the large amount of available data on wing-body combinations in the transonic speed range, but also has provided a valuable design tool for obtaining efficient transonic aircraft configurations. The area rule has been applied with great success in the design of a number of military airplanes operating in the transonic and supersonic speed ranges.

As a part of the general research on aircraft capable of operation at transonic speeds, the NACA has made wind-tunnel and tank tests of two configurations for large high-speed water-based airplanes. These airplanes are envisioned as taking off from sheltered water in a forward area, cruising at a high subsonic speed to the target area, being capable of making a supersonic dash over the target, and returning to their bases at cruise speed.

In order to insure delayed drag rise and low drag-rise increment near the speed of sound, the transonic-area-rule concept of reference 1 was used. In addition to adherence to the area-rule concept, aerodynamic

cleanness, low frontal area, and high fineness ratio were considered of primary importance.

The design of the planing surfaces (which are necessary for operation on the water), the forebody-afterbody proportions, and the hydrodynamic length-beam ratios were based on the information presented in references 2 to 5. The high fineness ratio, favorable for reduced aerodynamic drag at transonic speeds, is compatible with requirements for satisfactory hydrodynamic characteristics.

Two powerplant installations were considered, both of which were thought to be favorable for intake spray clearance: one with a nose inlet and the engines in the hull and the other with the inlet in the wing root and the engines in wing nacelles. Both configurations appeared to have definite aerodynamic or hydrodynamic advantages and also to present different problems in the layout of the configurations.

The purpose of this investigation was to determine whether or not the design procedure, based on the transonic area-rule concept, results in a hydrodynamically acceptable water-based aircraft having transonic drag comparable with that of land-based aircraft. The aerodynamic tests were confined principally to the determination of the zero-lift drag characteristics. The hydrodynamic tests included brief evaluations of the take-off resistance, spray characteristics, and the smooth-water take-off and landing behavior.

COEFFICIENTS AND SYMBOLS

The results of the wind-tunnel investigation are presented in terms of standard NACA coefficients and are referred to the wind axes.

Aerodynamic

A	duct area
c	local wing chord
$\bar{c}$	mean aerodynamic chord of wing
C_D	drag coefficient, D/qS
C_{D_o}	drag coefficient at zero lift
ΔC_{D_o}	incremental drag rise at zero lift, $\Delta C_{D_o} = C_{D_{o_M}} - C_{D_{o_{M=0.80}}}$

C_{D_I} internal drag coefficient of ducts based on wing area

C_L lift coefficient, L/qS

C_{L_α} lift-curve slope, $dC_L/d\alpha$

C_m pitching-moment coefficient, $M_{cg}/qS\bar{c}$

$C_{m_{C_L}}$ pitching-moment-curve slope, dC_m/dC_L

D drag

L lift

L/D lift-drag ratio

m mass-flow rate, ρAV

M Mach number

M_{cg} pitching moment of aerodynamic forces about lateral axis which passes through center-of-gravity location at $0.25\bar{c}$

p static pressure

q free-stream dynamic pressure, $\frac{1}{2}\rho V^2$

R Reynolds number based on $\bar{c}$

S wing area

V velocity

α angle of attack referred to forebody keel at step

δ_e elevator deflection referred to stabilizer chord, positive when trailing edge is down

δ_f flap deflection, positive downward

δ_s stabilizer incidence referred to forebody keel at step, positive when trailing edge is down

ρ air density

γ ratio of specific heats, 1.40 for air

Subscripts:

e	duct exit
i	duct inlet
o	free stream
max	maximum

Hydrodynamic

AP	after perpendicular
b	hull beam
C_{Δ_o}	gross-load coefficient, Δ_o/wb^3
FP	forward perpendicular
L_a	afterbody length
L_f	forebody length
w	specific weight of water, 63.3 lb/cu ft for these tests
Δ_o	gross load
τ	trim referred to forebody keel at step

DESCRIPTION OF THE CONFIGURATIONS

General-arrangement drawings of the wing-root-inlet configuration and the nose-inlet configuration are presented in figures 1 and 2, respectively. The hull lines for these configurations are presented in figures 3 and 4. Pertinent dimensions and particulars are presented in table I. A few of the considerations used in arriving at these configurations are discussed in detail.

Basic Assumptions

The gross weight of 160,000 pounds, wing area of 1,882 square feet, a bomb load of 30,000 pounds, and a rotating type of bomb bay were assumed. Four Curtiss-Wright J-67 jet engines were selected as the powerplants for which a take-off thrust of 88,000 pounds with afterburning was assumed.

Engine location.- For the wing-root-inlet configuration, the engines were located in nacelles in the inboard wing panels (fig. 1). The engine nacelles were placed symmetrically above and below the wing and extended forward for additional spray clearance. The leading edge of the elliptical inlet was swept back approximately parallel with the wing leading edge. The inlet had a stagger of 30° and was drooped 6° over a length equal to one-half the minor axis of the inlet ellipse.

For the nose-inlet configuration, the jet engines were located in the hull (fig. 2). The two engines forward of the center of gravity were angled outward 9° and the end of the exhaust tube was turned down 5° to exhaust under the wing. The two engines aft of the center of gravity were placed parallel to the center line and exhausted behind the vertical tail. Ducting for all four engines was fed from a single inlet at the nose. The ducting for the aft engines was designed for low losses.

Wing.- The wing selected for both model configurations had an aspect ratio of 4.0, taper ratio of 0.3, 45° sweepback of the quarter-chord line, and an NACA 65A006 airfoil section parallel to the plane of symmetry. Since primary emphasis was on the zero-lift drag characteristics, no camber or twist was incorporated. Flaps and leading-edge slats were installed to obtain necessary lift for take-off for the hydrodynamic tests.

For the engine-in-wing configuration, a gull wing permitted a lower wing-fuselage juncture while maintaining adequate spray clearance for the inlets. For the engine-in-hull configuration, a wing with the root at approximately three-quarters of the height of the hull was used. The incidence of the wing was 4°, so that the fuselage was at approximately zero angle of attack for the cruise condition.

Planing bottom.- The hydrodynamic planing surfaces were laid out so that the ratio of the forebody-to-afterbody length and the length-beam ratio were approximately the same as those for the seaplane described in reference 3. The width of the bomb bay established the beam. A simple dead-rise bottom with sharp chines was used in conjunction with vertical chine strips. From tests described in reference 5, such strips have been shown to increase the lift of the planing bottom and to reduce the height of the spray.

By the use of a vee plan form for the step, with ventilation ducts just aft of the step, a depth equivalent to one-half of that used for the seaplane described in reference 3 was considered adequate. The angle of afterbody keel and the height of the chines at the bow were kept low to avoid increase in drag due to warping the hull upward at the ends.

Tail group.- With the high beam loadings employed, a high horizontal-tail position was considered necessary for spray clearance.

Tip floats.- Since the floats were so far outboard from the fuselage, they were given a high fineness ratio, on the assumption that they might be treated as independent bodies. The planing bottoms had simple dead rise and sharp chines to assure positive lift.

Area Curves

Total-cross-sectional-area curves, and the contributions to this area by the component parts of the airplane, are shown in figures 5 and 6 for the wing-root-inlet configuration and for the nose-inlet configuration, respectively. An equivalent free-stream tube area of 80 percent of the inlet area was subtracted to account for the mass flow through the ducts.

These area curves which were developed for a Mach number of 1 are compared with those for a parabolic body of revolution with the maximum area at the midlength. The equivalent-body fineness ratio for the wing-root-inlet configuration was 10.9, as compared with 12.5 for the nose-inlet configuration.

Wind-Tunnel Models

The wind-tunnel models employed for the aerodynamic investigations were 1/47.19 scale. Three-view drawings and physical characteristics (full scale) are shown in figures 1 and 2 and in table I. Photographs of the two models are given in figures 7 and 8. The models were constructed primarily of paraplex-impregnated fiber-glass-cloth skin. The wings and horizontal tail surfaces had steel cores in order to increase the stiffness. Steel and mahogany were used in the hulls to add stiffness and strength at critical points in the models. It was necessary to modify the models at the aft end of the hulls for the sting supports.

The jet-engine inlets were simulated on each model configuration. The design and construction of the ducting were such as to provide the proper mass flow. Constrictions were placed in the duct exits for the purpose of evaluating the mass-flow and internal drag characteristics of each model configuration.

Provisions were made so each model could be tested with and without the wing tip floats. In addition, the nose-inlet model configuration could be tested with the tip floats off but with the equivalent tip-float area added to the hull according to the transonic area-rule concept of reference 1. The effects of chine strips, breaker strips, and a 10 to 1 step fairing were also tested on the nose-inlet configuration. The breaker strips, which were 3/32 inch in width, were located between hull stations 15 and 21 at the maximum hull cross section.

Tank Models

Photographs of the 1/15-size dynamic models of the wing-root-inlet and nose-inlet configurations are presented in figures 9 and 10, respectively. These models have hulls of plastic-impregnated fiber glass. The wings and tail surfaces are of built-up wood construction covered with silk.

Leading-edge slats, 0.15c, were used to prevent premature wing stall usually encountered at the low Reynolds numbers of the tank tests. Full-span, 0.30c, single-slotted flaps were installed on the nose-inlet model, and 62-percent-span, 0.30c, double-slotted flaps were installed on the wing-root-inlet model. The double-slotted flap was required for the latter model, since the flaps did not extend over the inboard portion of the wing. The flaps were designed to give a lift coefficient of approximately 1.2 at a trim of 10° with full deflection without ground effect. Provision was made so that the flaps could be fixed at deflections up to 40° in the case of the single slotted flaps and 50° for the double slotted flaps. No air flow was permitted through the ducts.

The deflection of the horizontal stabilizer was continuously variable from 5° to $-13\frac{1}{2}^{\circ}$ and could be controlled from the towing carriage by a Bowden cable, bell-crank mechanism. The elevators could be fixed at angles from 20° to -20°.

Electric contacts, which were located on the keel at the bow, step, and sternpost, were used to indicate when these portions of the hull were in the water and to release the trim brake used in the landing tests.

APPARATUS AND PROCEDURES

Wind Tunnel

Tunnel.- The aerodynamic investigations were conducted in the Langley 8-foot transonic tunnel which has a dodecagonal cross section and is a slotted-throat, single-return type of wind tunnel. This tunnel is designed to obtain aerodynamic data through the speed of sound without the usual effects of choking and blockage. The tunnel operates at atmospheric stagnation pressures. A more complete description of the tunnel can be found in reference 6.

Reynolds number.- The Reynolds number based on the mean aerodynamic chord of the wing is shown in figure 11 as a function of test Mach number.

The Reynolds number varied from 1.64×10^6 to 2.00×10^6 for the present investigation.

Measurements.- Lift, drag, and pitching moment were determined by means of an electrical strain-gage balance located inside the hull. The measurements were taken over a limited angle-of-attack range because of strength limitations of the models. The Mach number range varied from 0.60 to 1.13. Static-pressure measurements were taken at two locations in the duct exits: one upstream and one downstream of the constriction in area, to determine the mass-flow and internal drag coefficient. The base pressure at the aft end of the hull was also measured.

Corrections and accuracy.- No corrections to the free-stream Mach number and dynamic pressure for the effects of model and wake blockage are necessary for tests in the slotted test section of the Langley 8-foot transonic tunnel (ref. 7). There is a range of Mach numbers above a Mach number of 1.00 where the data are affected by reflected compressions and expansions from the test section boundary. From considerations of the results of reference 8, it is believed that for Mach numbers up to approximately 1.03 the effects of these disturbances on the measurements made in the present investigation would be negligible. No test data, however, were taken in the range ($M > 1.03$ and $M < 1.12$) where the reflected boundary disturbances impinged upon the models.

The drag data have been corrected for base pressure such that the drag corresponds to conditions where the base pressure is equal to the free-stream static pressure. The internal drag has been also subtracted from the drag data so that a net external drag was obtained. The method for obtaining internal drag is presented in the appendix. The variation with Mach number of the internal-drag coefficient for the two configurations is shown in figure 12. This drag coefficient is the total value of the four nacelles for each configuration.

No corrections for the forces and moments produced by the sting interference have been applied to the data. As indicated in reference 9, the significant corrections would be limited to small increments in pitching moment and drag.

The angle of attack has been corrected for the deflection of the sting support system under load. The angle of attack is estimated to be accurate to within $\pm 0.1^\circ$.

The estimated consistency of the data at a Mach number of 0.90, based on the static calibrations and the repeatability of the data, is as follows:

C_L	± 0.003
C_D	± 0.0006
C_m	± 0.002

These errors would be inversely proportional to the dynamic pressure and therefore would be lower at the higher Mach numbers.

Tank Tests

The hydrodynamic tests were made in Langley tank no. 1, which is described in reference 10. The apparatus and procedure generally used for testing dynamic models are described in reference 11. A photograph of the setup of the model on the towing carriage is presented in figure 13.

For these tests the model was free to trim and free to rise but was otherwise restrained. Slide-wire pickups were used to obtain records of the trim and rise. All tests were made at the design gross weight corresponding to 160,000 pounds. The center of gravity was at $0.25\bar{c}$ unless otherwise specified. Rise was set zero with the step touching the water with the hull at zero trim. Trim was referenced to the forebody keel at the step.

The resistance of the complete model, including air drag, was determined for a range of constant speeds. A flap deflection of 0° was used up to the speed at which hump trim occurred. At higher speeds, full flap deflection was used. The air drag of the towing staff was subtracted as a tare from the total resistance. Spray observations and photographs were obtained during these runs.

Take-offs were simulated using an acceleration which approximated that expected on the basis of the available excess thrust. Observations and motion pictures were made during these runs. The longitudinal stability was observed during constant-speed runs for the range of trims available from the aerodynamic controls.

Landings were made with full flaps for a range of initial landing trims. With the model just clear of the water at a speed slightly above flying speed, the model was trimmed in the air to the desired landing trim and the trim brake set. The carriage was then decelerated (approximately 5 feet per second per second) and the model glided onto the water. At contact the trim brake was automatically released. The trim and rise were recorded and motion pictures were taken during the landing runout.

RESULTS AND DISCUSSION

Wind-Tunnel Tests

Throughout this part of the discussion, unless otherwise noted, the nose-inlet or the wing-root-inlet model configuration refers to the complete model; that is, the model having the hull, wings, wing-tip floats, horizontal tail ($\delta_s = 0^{\circ}$), and the vertical tail.

The basic aerodynamic data for the two model configurations are presented in figures 14 to 21. The design inlet mass-flow ratio for the two model configurations was 0.80. The variation of mass-flow ratio with Mach number for the two configurations is given in figure 22 and thus it can be seen that the experimental results are in good agreement with the design value.

Drag characteristics.- A comparison of the drag characteristics at zero lift for the two configurations is presented in figure 23. The subsonic drag coefficient of the nose-inlet configuration was about 0.0167. The drag at subsonic speeds of the wing-root-inlet model was 0.0190, or about 13 percent higher compared with the nose-inlet model. This increase in the subsonic drag level of the wing-root-inlet model would be expected, because the wetted area of the wing-root-inlet model was 11 percent higher than that of the nose-inlet model. (See table I.) The drag rise of both model configurations occurred at approximately a Mach number of 0.92. It is interesting to note the low values of the zero-lift drag coefficients for both configurations at Mach number of 1.00. The low values of drag coefficient for both of the present models measured near Mach number 1.00 are due to the application of the transonic area rule and the use of a moderately low wing thickness which results in a high equivalent-body fineness ratio that is compatible for low transonic drag.

A comparison of the incremental drag-rise curves at zero-lift coefficient for the two model configurations without the wing-tip floats is made in figure 24. The drag-rise curves were started at a Mach number of 0.80 in order to minimize any skin-friction effects. It will be noted that the nose-inlet model had the lower drag rise of the two models throughout the Mach number range. Theoretical calculations were made of the wave drag for the equivalent parabolic body of revolution at a Mach number of 1.00 using the methods of reference 12. The results of these calculations are also included in figure 24. Good agreement exists between the experimental and calculated wave drags for the two configurations.

It is also of interest to make comparisons of the performance characteristics of the models. Unfortunately, the strength of the models was limited and, as a result, complete data necessary to define the maximum lift-drag ratios could not be obtained. From available information, calculations of the maximum lift-drag ratios can be made for the nose-inlet configuration using the experimental zero-lift drag characteristics of the model and the drag due to lift for the plane wing of reference 13. It is known that twist and camber applied to a wing can improve the performance characteristics. Therefore, similar calculations of the maximum lift-drag ratios can be made using the drag due to lift for the twisted and cambered wing of reference 14. The results of these calculations are presented in figure 25. The nose-inlet model configuration with the plane wing had a value of maximum lift-drag ratio of 10.0 at a cruise Mach number of 0.90. At the same Mach number, applying twist and camber to the wing increased the value of the maximum lift-drag ratio to 12.3. As the

Mach number was increased to 1.13, the calculated $(L/D)_{max}$ values decreased to 6.0 and 6.3 for the configuration with the plane wing and the twisted and cambered wing, respectively.

These results merely indicate procedures which can be taken to improve the lift-drag ratios. However, this is always a subject for continued research. Furthermore, it should be remembered that the present models were designed according to the transonic area rule of reference 1. It is believed that if the models were designed for higher supersonic speeds according to the methods of reference 15, the lift-drag ratios, particularly at supersonic speeds, could be improved further.

The effects on the zero-lift drag coefficient of adding chine strips, breaker strips, and of fairing out the step in the hull with a 10 to 1 step fairing on the nose-inlet configuration is shown in figure 26. In general, each of the components caused small increases in the zero lift-drag coefficient of the nose-inlet model for Mach numbers up to about 1.03. The step fairing caused a drag reduction of approximately 4 percent for the nose-inlet model at a Mach number of 1.13.

The effects of the wing-tip floats on the zero lift-drag coefficients of the nose-inlet model and the wing-root inlet model are presented in figures 27 and 28, respectively. Both models with the wing-tip floats off exhibited lower zero-lift drag characteristics throughout the Mach number range even though the removal of the tip floats caused deviations in the area curves. The equivalent area of the floats was added to the hull of the nose-inlet model according to the transonic area-rule concept of reference 1. The results of these tests, which are shown in figure 27, indicated no differences in zero-lift drag between the nose-inlet configuration with tip floats off and the configuration with tip floats off but with the equivalent area added.

Longitudinal stability characteristics.- A comparison of the lift-curve slopes for both models is made in figure 29. The lift-curve slope of the wing-root-inlet model was approximately 3 to 5 percent higher than the nose-inlet model throughout the Mach number range. Removal of the wing-tip floats generally reduced the lift-curve slopes of each model. (Compare fig. 14(a) with fig. 18(a), for instance.)

The pitching-moment-curve slopes $C_{m_{C_L}}$ at low lift coefficients have been determined and are given in figure 30 for the two model configurations. The usual rearward movement of the aerodynamic-center location is indicated for the nose-inlet model; however, it is interesting to note that the aerodynamic center moved rearward only 13 percent of the mean aerodynamic chord for the Mach number range shown. The wing-root-inlet model also showed a rearward movement of aerodynamic-center

location up to a Mach number of 1.03; however, with an increase in Mach number to 1.13, the aerodynamic center moved forward rapidly.

Hydrodynamic Tests

Wing-root-inlet configuration.- Typical photographs of the low-speed bow spray are presented in figure 31. In general, the low-speed spray characteristics were considered excellent. The bow blisters were formed at relatively low speeds, with the spray breaking clear at the chines. There was no tendency for spray to enter the inlets at any speed. The flaps, in the fully deflected position, and the nacelles were wetted by the bow blister over a speed range from 50 to 80 knots. The horizontal tail was clear of spray at all speeds.

At high speeds the wake from the forebody moved inboard and wetted the sides of the afterbody. This narrowing of the forebody wake is particularly characteristic of high-length-beam-ratio hulls with heavy loads. The increase in width of the hull above the afterbody chines increased the wetting by this wake.

The total resistance, and the corresponding trim and rise, with 0° flaps (low speed) are presented in figure 32. Little change in trim or rise was noted up to a speed of about 50 knots. Beyond this speed, the trim increased rapidly to a value slightly greater than the sternpost angle and there was a marked increase in rise. The delay in the tendency to increase trim at low speeds is associated with the long afterbody and is similar to that found for the length-beam-ratio-15 hull with a long afterbody, described in reference 3. The maximum resistance, with 0° flaps, occurred at approximately 60 knots; the corresponding gross-load—total-resistance ratio is about 4.5.

The resistance, trim, and rise with 50° flaps are presented in figure 33. These data were obtained with the center of gravity at $0.32\bar{c}$. The positive aerodynamic trimming moment with the center of gravity at $0.25\bar{c}$ was insufficient to raise the bow at high speeds with this flap deflection. Comparison of the data for the two flap positions indicates that full deflection of these flaps is of no advantage insofar as the resistance is concerned, until high speeds are reached.

At high speeds, approaching getaway, the resistance increased and the afterbody sides were heavily wetted. The flow over the curved portion of the afterbody caused erratic but small-amplitude oscillations in trim. Ample excess thrust was available for acceleration at all speeds.

The trim and rise during a simulated take-off with 50° flaps and with the center of gravity at $0.32\bar{c}$ are presented in figure 34. The

acceleration was approximately $4\frac{1}{2}$ feet per second per second, except near getaway, where it was reduced to about 2 feet per second per second. Slight upper-limit porpoising was encountered at a speed of about 100 knots, but the amplitudes of the motion were negligible. This porpoising, as well as the erratic trim oscillations due to wetting of the afterbody sides, does not appear to be a take-off problem, inasmuch as the long afterbody limited the amplitude of the oscillations to less than 3°.

The variation of trim and rise during typical landings at 8° and 14° are presented in figure 35. Landings were made with the center of gravity at 0.32$\bar{c}$. Upper-limit porpoising occurred during these landings because the landing trims were above the upper trim limits of stability. The motions, which were damped as the speed decreased, were not violent. Again the long afterbody effectively restricted the motions in trim. Since the porpoising motions are not violent, landings at high trims might be preferable because of the reduced landing speed.

Nose-inlet configuration.- Typical photographs of the bow spray are presented in figure 36. Although there was no spray in the inlets at any speed, the sides of the ducts on the forebody were heavily wetted at low speeds. The spray did not break completely clear at the chines, but flowed around the curved surface of the ducts and over the top of the wing until a speed of approximately 50 knots, above which speed the forebody chines became effective. The under surface of the wing was heavily wetted by bow spray at speeds up to 70 knots. The horizontal tail was clear of spray at all speeds. The sides of the afterbody above the chines and the sides of the rear ducts were wetted as the forebody wake became narrow at high speeds.

The total resistance and the corresponding trim and rise, with 0° flaps, are presented in figure 37. The trim remained low and the rise appeared to decrease slightly up to a speed of about 50 knots. The resistance increased rapidly to a maximum at about 50 knots. At this point the gross-load—total-resistance ratio was 2.3 as compared with 4.5 for the wing-root-inlet configuration. Above 50 knots, the resistance decreased and the trim increased as the water broke away from the sides of the forebody. The high resistance is associated with the extremely low trim. Although low trims may be expected for this configuration with a long afterbody, it is believed that improving the flow around the bow and an increase in forebody length would permit sufficient trimming up to appreciably reduce the hump resistance and bow spray.

The total resistance, trim, and rise with 40° flaps is presented in figure 38. Comparison of the resistance obtained with the two flaps positions shows that full deflection of the flaps is of no advantage insofar as the resistance is concerned, until high speeds are reached. Ample excess thrust was available for acceleration at high speeds.

The variation in trim and rise during take-off is shown in figure 39. A flap deflection of 0° and a high acceleration (approximately 5 feet per second per second) were used at low speeds. The rate of acceleration was decreased to about 1 foot per second per second over the hump. The high-speed portion of the take-off was made with 40° flaps with an acceleration of approximately 4 feet per second per second.

Upper-limit porpoising was encountered as the trim crossed the upper trim limit at about 100 knots. The motions were not violent and the amplitude did not exceed 3°. By holding a lower trim at high speeds and pulling up near getaway speed, this porpoising could be avoided.

The trim and rise during landing are presented in figure 40 for typical landings at trims of 8° and 14°. The landing behavior was similar to that of the wing-root-inlet configuration.

CONCLUDING REMARKS

Two multijet seaplanes for high-speed operation incorporating some recent aerodynamic and hydrodynamic research have been investigated. The aerodynamic layout of the configurations was based on a transonic area-rule concept. Results of the wind-tunnel and tank tests have indicated that seaplane configurations can be designed which have low subsonic drag, relatively high Mach number for drag rise, low transonic drag-rise increment, and satisfactory hydrodynamic qualities. Further improvement can be made in the aerodynamic and the hydrodynamic characteristics of seaplane configurations.

Langley Aeronautical Laboratory,
National Advisory Committee for Aeronautics,
Langley Field, Va., January 10, 1955.

APPENDIX

METHOD FOR OBTAINING INTERNAL DRAG

Several assumptions must be made before the two static orifices which were installed upstream and downstream of the constriction in the nacelle duct exits can be used to compute the internal drag. The stagnation pressure and temperature must be assumed to be the same at the two stations, and the flow across the duct must be assumed to be uniform. The latter assumption appears to be the more questionable, particularly at angles of attack. It should be remembered, however, that the errors which may be introduced by the above assumptions will have only a minor influence on the external drag of the two model configurations because the absolute magnitude of the internal drag is small.

The internal drag D_I is defined as

$$D_I = A_e(p_o - p_e) + m_e(V_o - V_e)$$

By using the assumptions discussed above, the following equation for the internal drag coefficient of each nacelle duct can be derived:

$$C_{D_I} = \frac{2}{\gamma M_o^2}\frac{A_e}{S}\left\{1 - \frac{p_e}{p_o} + \frac{p_e}{p_o}\gamma M_e^2\left[\frac{M_o}{M_e}\left(\frac{1 + \frac{\gamma - 1}{2}M_e^2}{1 + \frac{\gamma - 1}{2}M_o^2}\right)^{1/2} - 1\right]\right\}$$

REFERENCES

1. Whitcomb, Richard T.: A Study of the Zero-Lift Drag-Rise Characteristics of Wing-Body Combinations Near the Speed of Sound. NACA RM L52H08, 1952.

2. Carter, Arthur W., and Haar, Marvin I.: Hydrodynamic Qualities of a Hypothetical Flying Boat With a Low-Drag Hull Having a Length-Beam Ratio of 15. NACA TN 1570, 1948.

3. Kapryan, Walter J., and Clement, Eugene P.: Effect of Increase in Afterbody Length on the Hydrodynamic Qualities of a Flying-Boat Hull of High Length-Beam Ratio. NACA TN 1853, 1949.

4. Whitaker, Walter E., Jr., and Bryce, Paul W., Jr.: Effect of an Increase in Angle of Dead Rise on the Hydrodynamic Characteristics of a High-Length-Beam-Ratio Hull. NACA TN 2297, 1951.

5. Kapryan, Walter J., and Boyd, George M., Jr.: The Effect of Vertical Chine Strips on the Planing Characteristics of V-Shaped Prismatic Surfaces Having Angles of Dead Rise of 20° and 40°. NACA TN 3052, 1953.

6. Wright, Ray H., and Ritchie, Virgil A.: Characteristics of a Transonic Test Section With Various Slot Shapes in the Langley 8-Foot High-Speed Tunnel. NACA RM L51H10, 1951.

7. Wright, Ray H., and Ward, Vernon G.: NACA Transonic Wind-Tunnel Test Sections. NACA RM L8J06, 1948.

8. Ritchie, Virgil S., and Pearson, Albin O.: Calibration of the Slotted Test Section of the Langley 8-Foot Transonic Tunnel and Preliminary Experimental Investigation of Boundary-Reflected Disturbances. NACA RM L51K14, 1952.

9. Osborne, Robert S.: High-Speed Wind-Tunnel Investigation of the Longitudinal Stability and Control Characteristics of a 1/16-Scale Model of the D-558-2 Research Airplane at High Subsonic Mach Numbers and at a Mach Number of 1.2. NACA RM L9C04, 1949.

10. Truscott, Starr: The Enlarged N.A.C.A. Tank, and Some of Its Work. NACA TM 918, 1939.

11. Olson, Roland E., and Land, Norman S.: Methods Used in the NACA Tank for the Investigation of the Longitudinal-Stability Characteristics of Models of Flying Boats. NACA Rep. 753, 1943. (Supersedes NACA WR L-409.)

12. Holdaway, George H.: Comparison of Theoretical and Experimental Zero-Lift Drag-Rise Characteristics of Wing-Body-Tail Combinations Near the Speed of Sound. NACA RM A53H17, 1953.

13. Morgan, Francis G., Jr., and Carmel, Melvin M.: Transonic Wind-Tunnel Investigation of the Effects of Taper Ratio, Body Indentation, Fixed Transition, and Afterbody Shape on the Aerodynamic Characteristics of a 45° Sweptback Wing-Body Combination. NACA RM L54A15, 1954.

14. Cooper, J. Lawrence: A Transonic Wind-Tunnel Investigation of the Effects of Twist and Camber With and Without Incidence, Twist, and Body Indentation on the Aerodynamic Characteristics of a 45° Sweptback Wing-Body Configuration. NACA RM L54B15, 1954.

15. Whitcomb, Richard T., and Fischetti, Thomas L.: Development of a Supersonic Area Rule and an Application to the Design of a Wing-Body Combination Having High Lift-to-Drag Ratios. NACA RM L53H31a, 1953.

TABLE I.- PARTICULARS OF CONFIGURATIONS

	Nose-inlet	Wing-root-inlet
General:		
Gross weight, lb	160,000	160,000
Wing area, sq ft	1,882	1,882
Engines, Curtiss-Wright J-67	4	4
Take-off thrust (with afterburner), lb	88,000	88,000
Wing loading, lb/sq ft	85	85
Take-off thrust-weight ratio	0.55	0.55
Wing:		
Span, ft	86.9	86.9
Airfoil section	NACA 65A006	NACA 65A006
Aspect ratio	4.0	4.0
Taper ratio	0.3	0.3
Sweepback (0.25$\bar{c}$), deg	45	45
Dihedral, deg	-2	Inboard 25.5 Outboard -13.5
Length, mean aerodynamic chord, ft	23.8	23.8
Forward perpendicular to L.E. of M.A.C., ft	60.6	66.4
Incidence, deg	4	4
Horizontal tail:		
Span, ft	31.7	31.7
Airfoil section	NACA 65A006	NACA 65A006
Area, sq ft	250	250
Aspect ratio	4.0	4.0
Taper ratio	0.3	0.3
Sweepback (0.25$\bar{c}$), deg	45	45
Dihedral, deg	0	0
Arm, between quarter-chord, ft	81.3	81.3
Height above base line, ft	31.4	31.4
$\frac{\text{Elevator chord}}{\text{Stabilizer chord}}$	0.36	0.36
Vertical tail:		
Airfoil section	NACA 65A008	NACA 65A008
Aspect ratio	1.19	1.19
Sweepback (0.25$\bar{c}$), deg	48	48
Bullet fairing	NACA 64A012	NACA 64A012
Hull:		
Forebody length (chines at bow to step centroid), ft	58.4	75.8
Afterbody length (step centroid to after perpendicular), ft	89.7	83.0
Length, overall, ft	160	158.8
Beam at chines, maximum, ft	8.9	8.9
Width, maximum, ft	11.4	12.7
Height, maximum, ft	15.5	17.1
Step plan form	60° vee	60° vee
Step depth at keel, ft	0.5	0.5
Step depth at chine, ft	1.02	1.02
Ventilation area, inboard and aft of step, sq ft	1.6	1.6
Dead rise at bow, basic, deg	38	45
Dead rise at step, basic, deg	25	25
Dead rise at after perpendicular, basic, deg	37.2	37.2

TABLE I.- PARTICULARS OF CONFIGURATIONS - Concluded

	Nose-inlet	Wing-root-inlet
Vertical spray strips, max.depth, ft	0.55	0.55
Afterbody keel angle, deg	5.4	5.4
Sternpost angle, deg	5.7	5.7
Center of gravity, 0.25$\bar{c}$ above base line, ft	8.2	9.9
Forward of step centroid, ft	3.6	3.6
Step centroid to 0.25$\bar{c}$, angle to vertical, deg	23.7	20.0
Hull volume (vol. of ducts subtracted for nose-inlet design), cu ft	5,660	10,560
Ratio of hull excess buoyancy to gross load	2.90	3.22
Surface area, sq ft	4,250	4,420
$\frac{L_f}{b_{max}}$	6.6	8.5
$\frac{L_a}{b_{max}}$	10.1	9.4
$\frac{L_f + L_a}{b_{max}}$	16.7	17.9
C_{Δ_o}	3.55	3.55
$K = \frac{C_{\Delta_o}}{\left(\frac{L_f + L_a}{b}\right)^2}$	0.013	0.011
$k = \frac{C_{\Delta_o}}{\left(\frac{L_f}{b}\right)^2}$	0.082	0.049
Tip floats:		
Length, ft	26.6	26.6
Beam, maximum, ft	3.18	3.18
Height, maximum, ft	2.83	2.83
Volume, each float, cu ft	97.9	97.9
Dead rise, deg	20	20
Length-beam ratio	8.37	8.37
Area curves:		
Maximum net cross-sectional area, sq ft	131	167
Maximum diameter of equivalent parabolic body, ft	12.9	14.5
Length, ft	160	159
Fineness ratio of equivalent parabolic body	12.5	10.95
$\frac{\text{Maximum hull cross-sectional area}}{\text{Wing area}}$	0.058	0.070
$\frac{\text{Duct area}}{\text{Maximum hull cross-sectional area}}$	0.156	0.124
Position of maximum cross section of equivalent parabolic body	0.50L	0.50L
Total surface area, sq ft	8,970	9,960

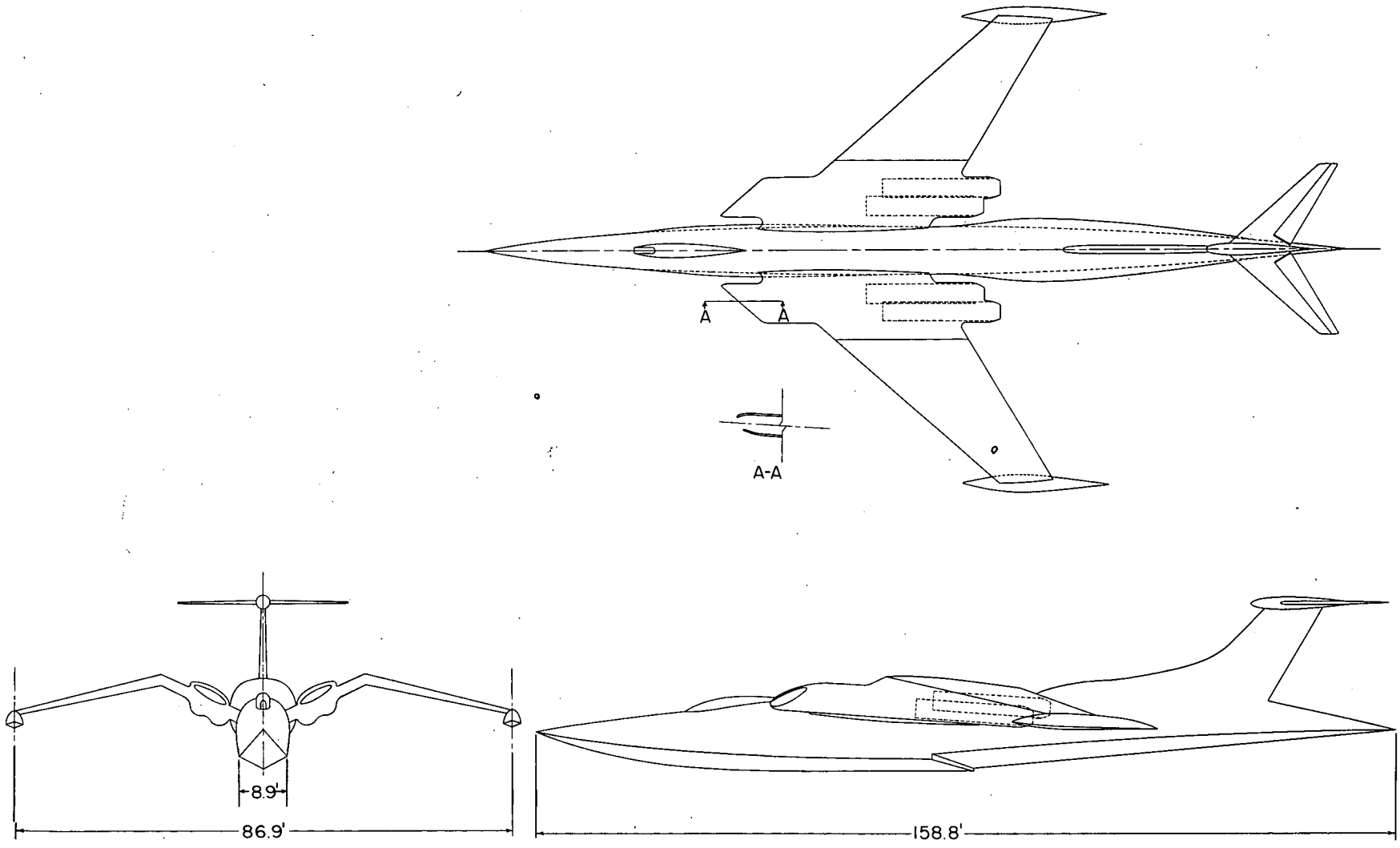

(a) General arrangement.

Figure 1.- Wing-root-inlet configuration.

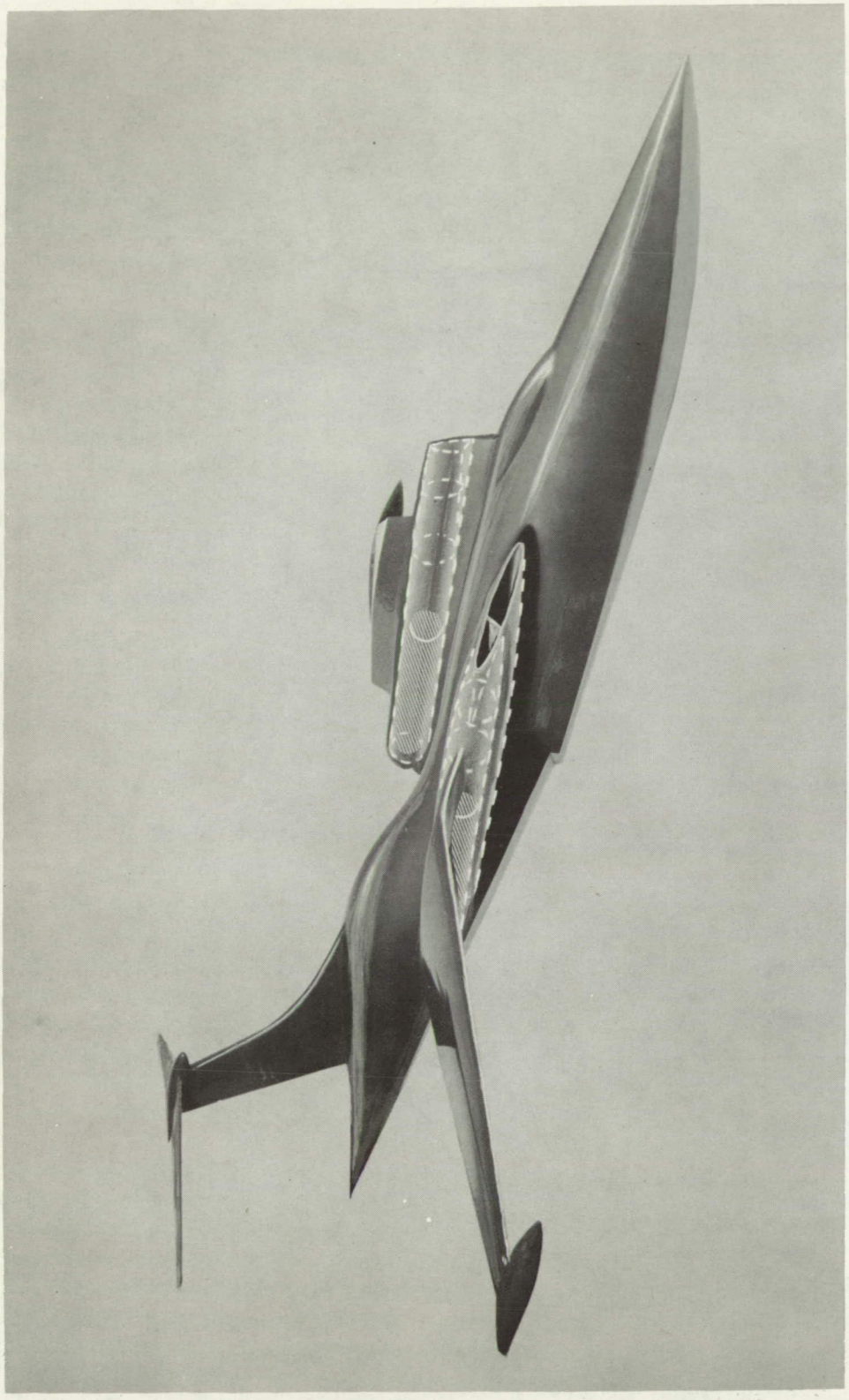

L-87491.1

(b) Ducting.

Figure 1.- Concluded.

(a) General arrangement.

Figure 2.- Nose-inlet configuration.

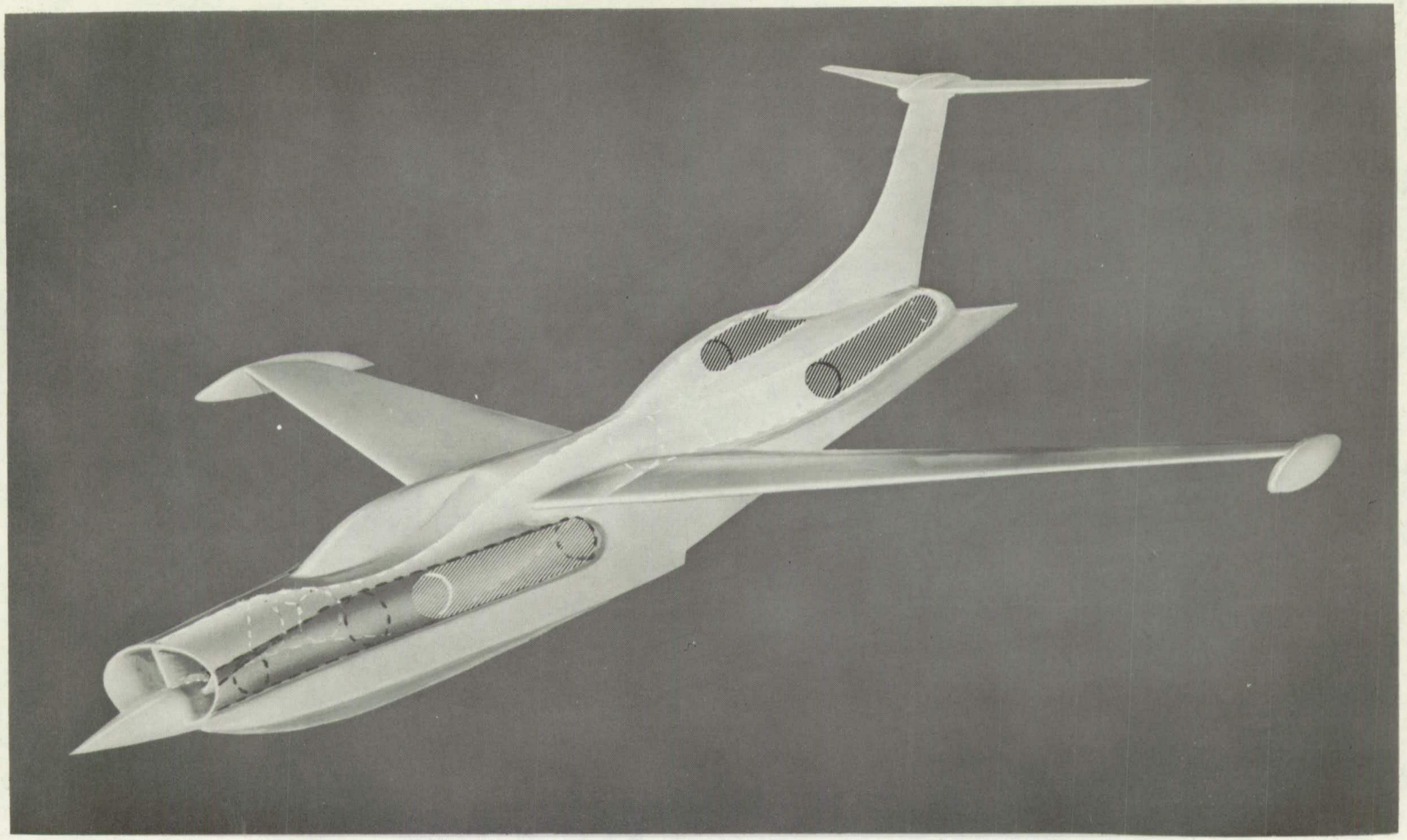

L-87767.1

(b) Ducting.

Figure 2.- Concluded.

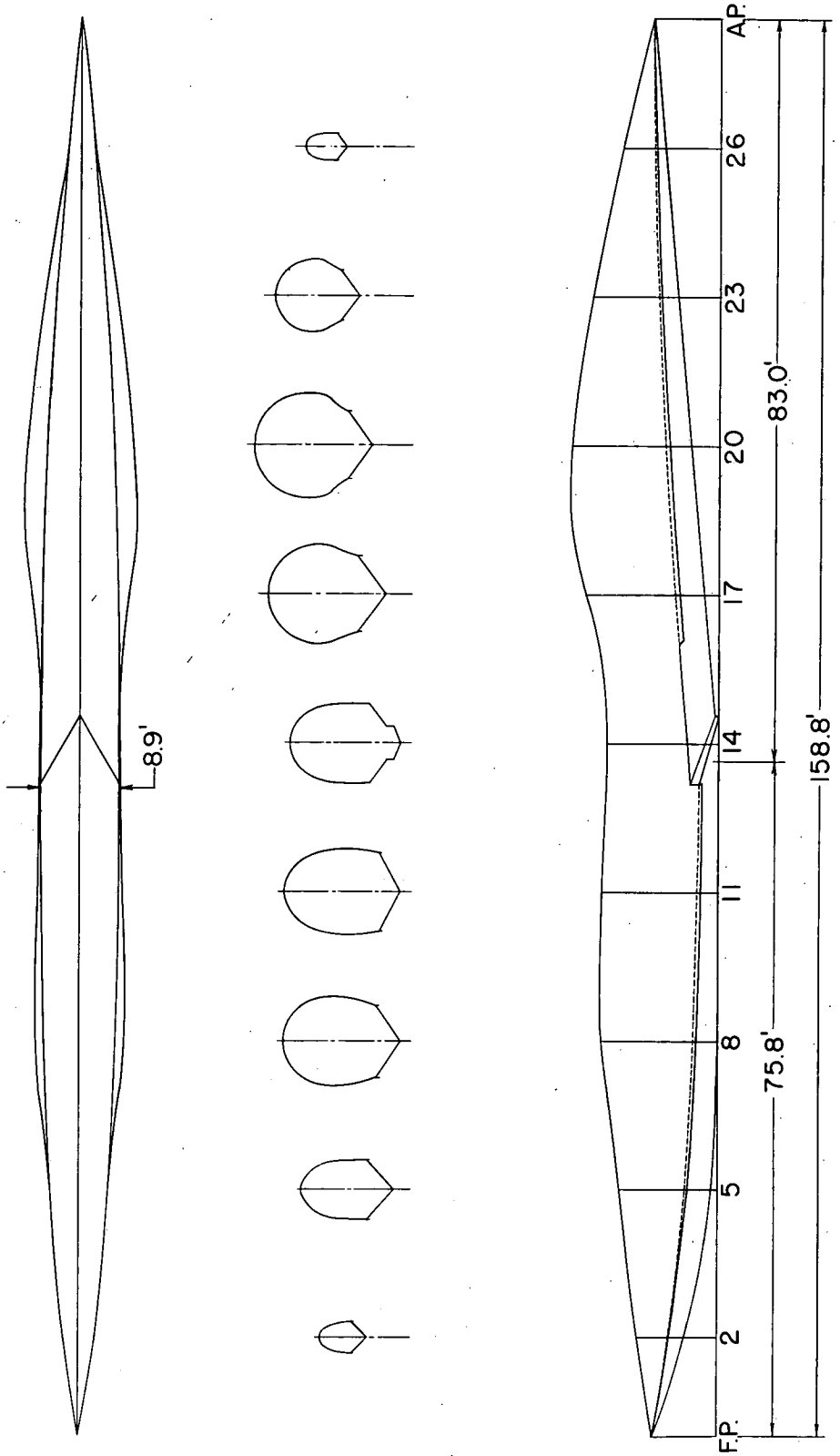

Figure 3.- Hull lines. Wing-root-inlet configuration.

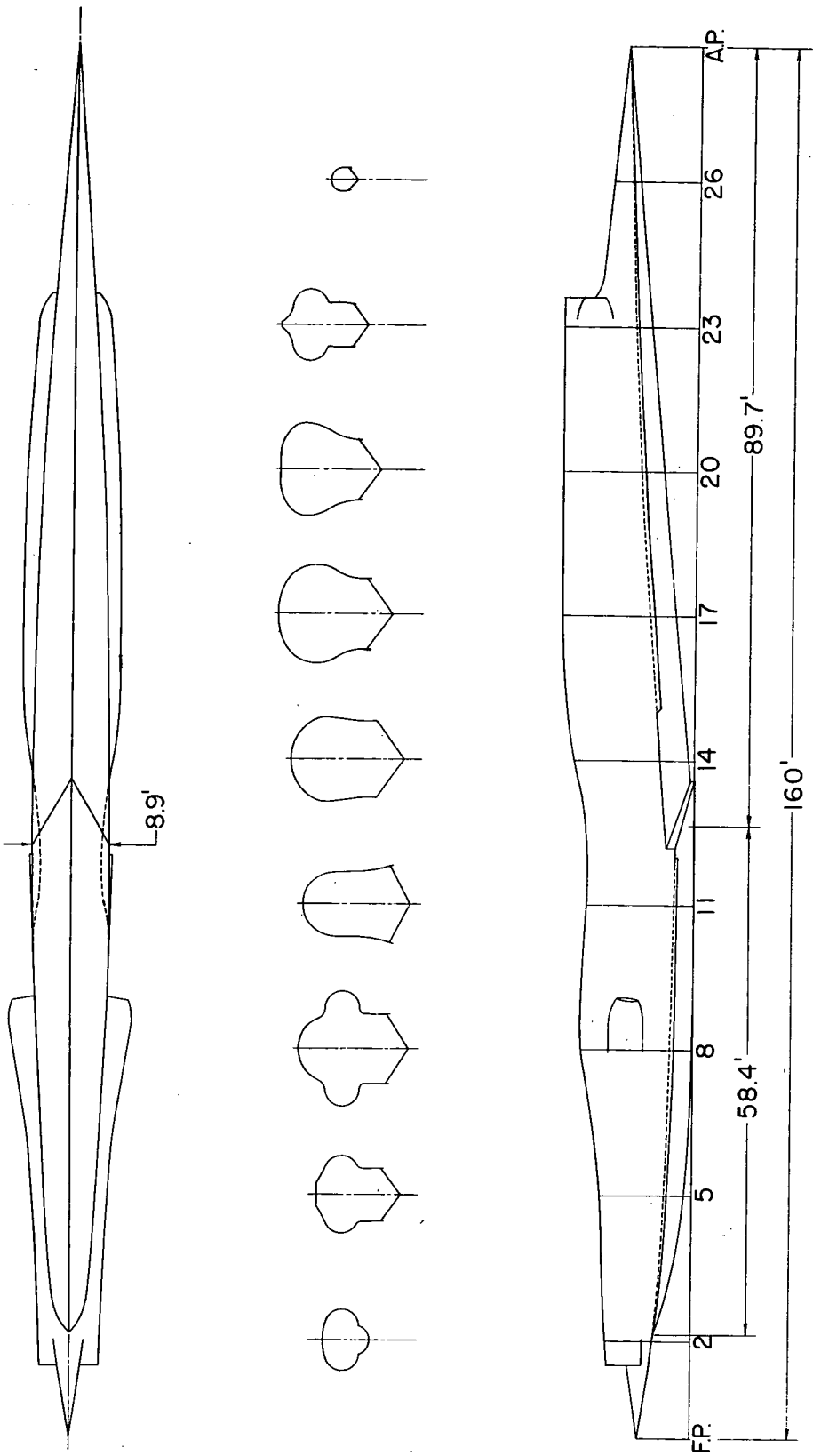

Figure 4.- Hull lines. Nose-inlet configuration.

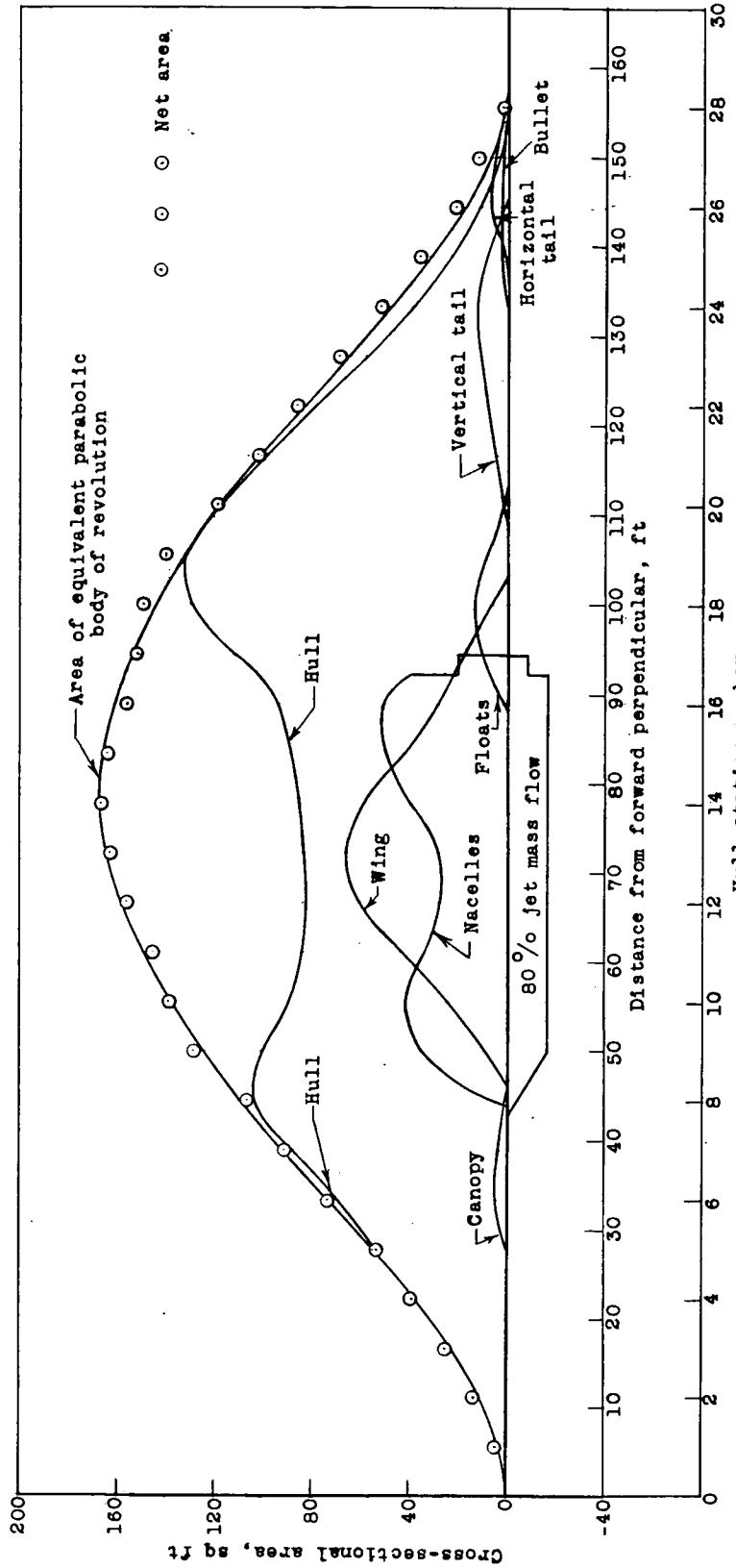

Figure 5.- Cross-sectional-area curves of wing-root-inlet configuration.

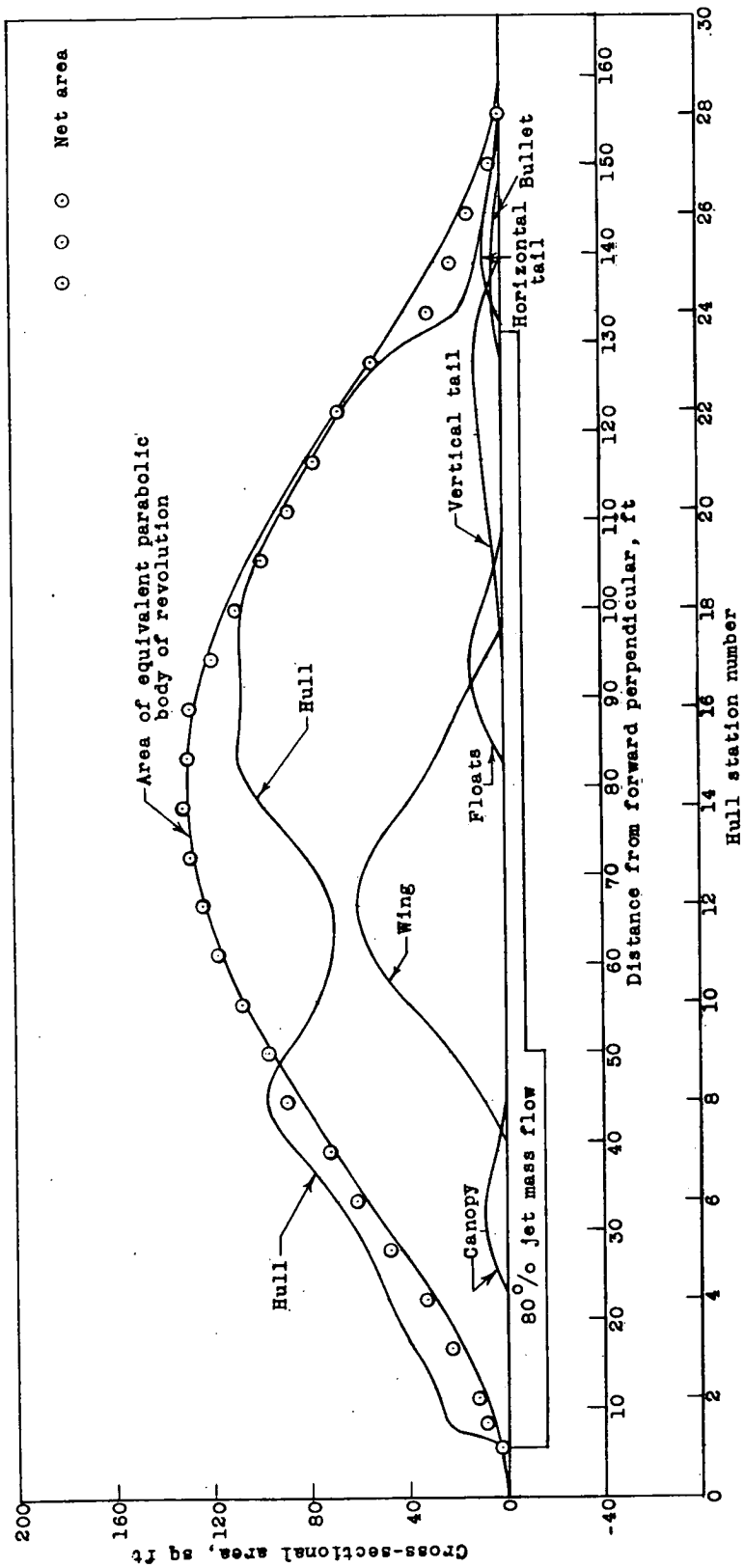

Figure 6.- Cross-sectional-area curves of nose-inlet configuration.

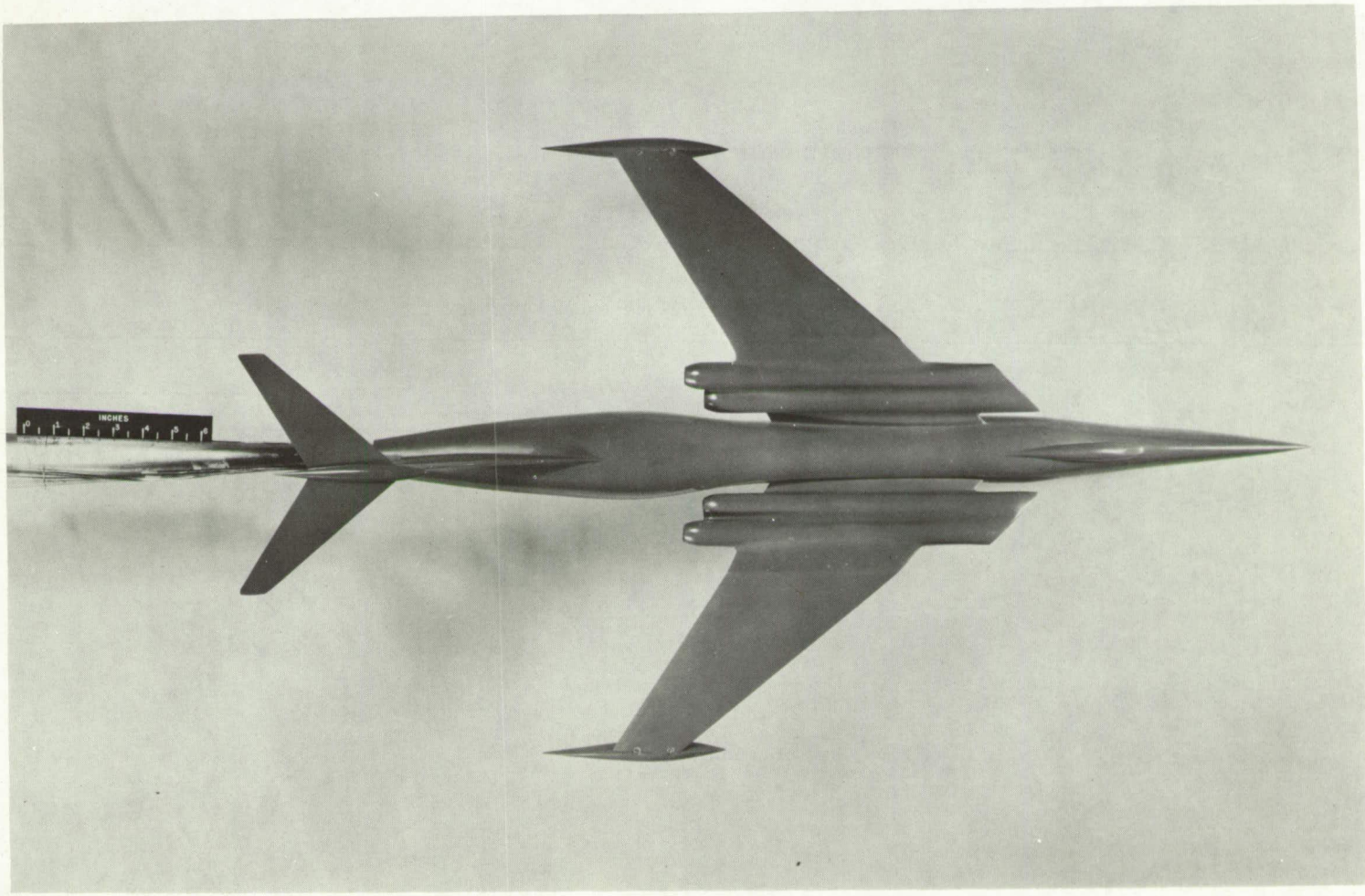

(a) Plan view.

L-87489

Figure 7.- Wing-root-inlet configuration tested in the Langley 8-foot transonic tunnel.

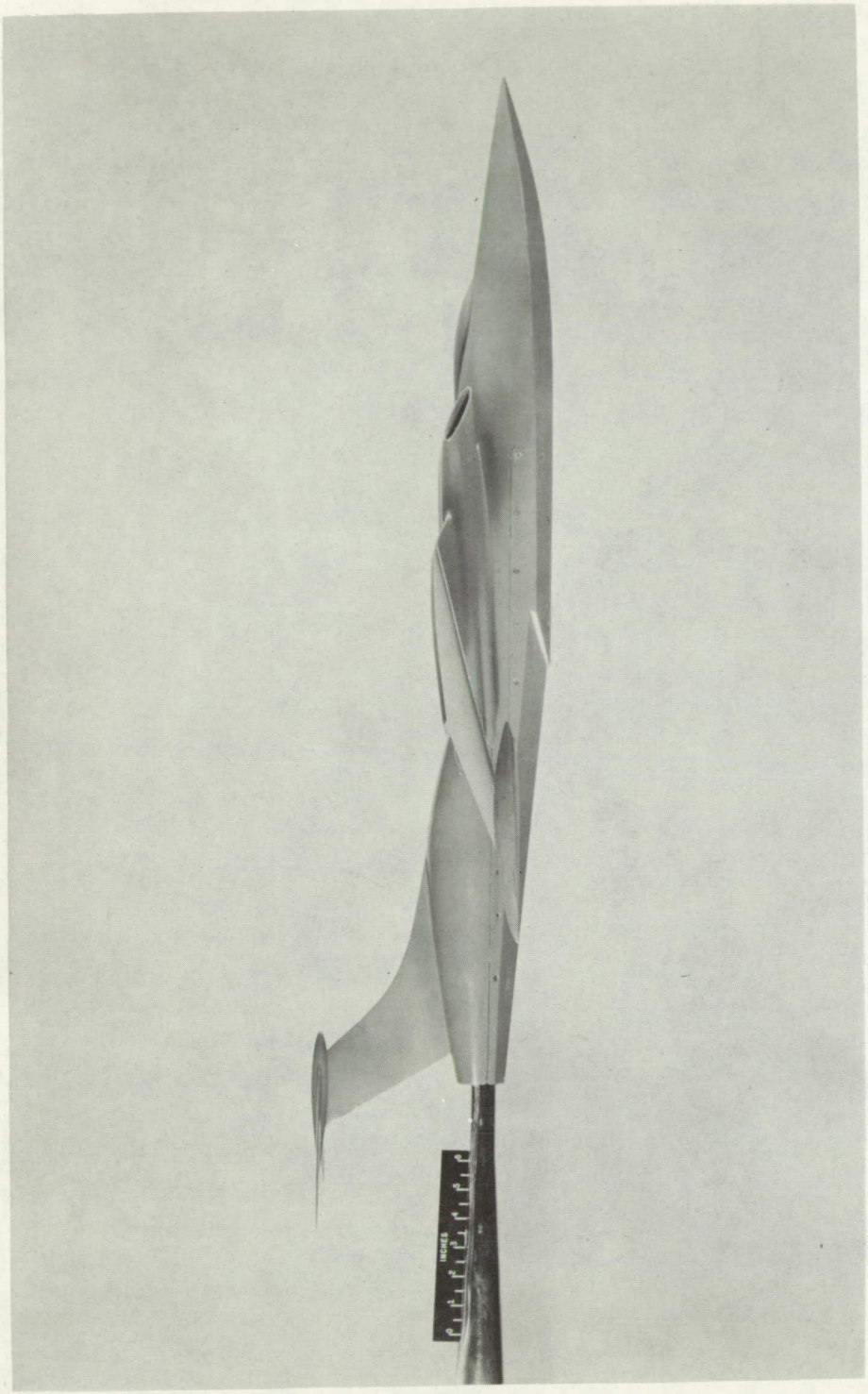

L-87490

(b) Side view.

Figure 7.- Continued.

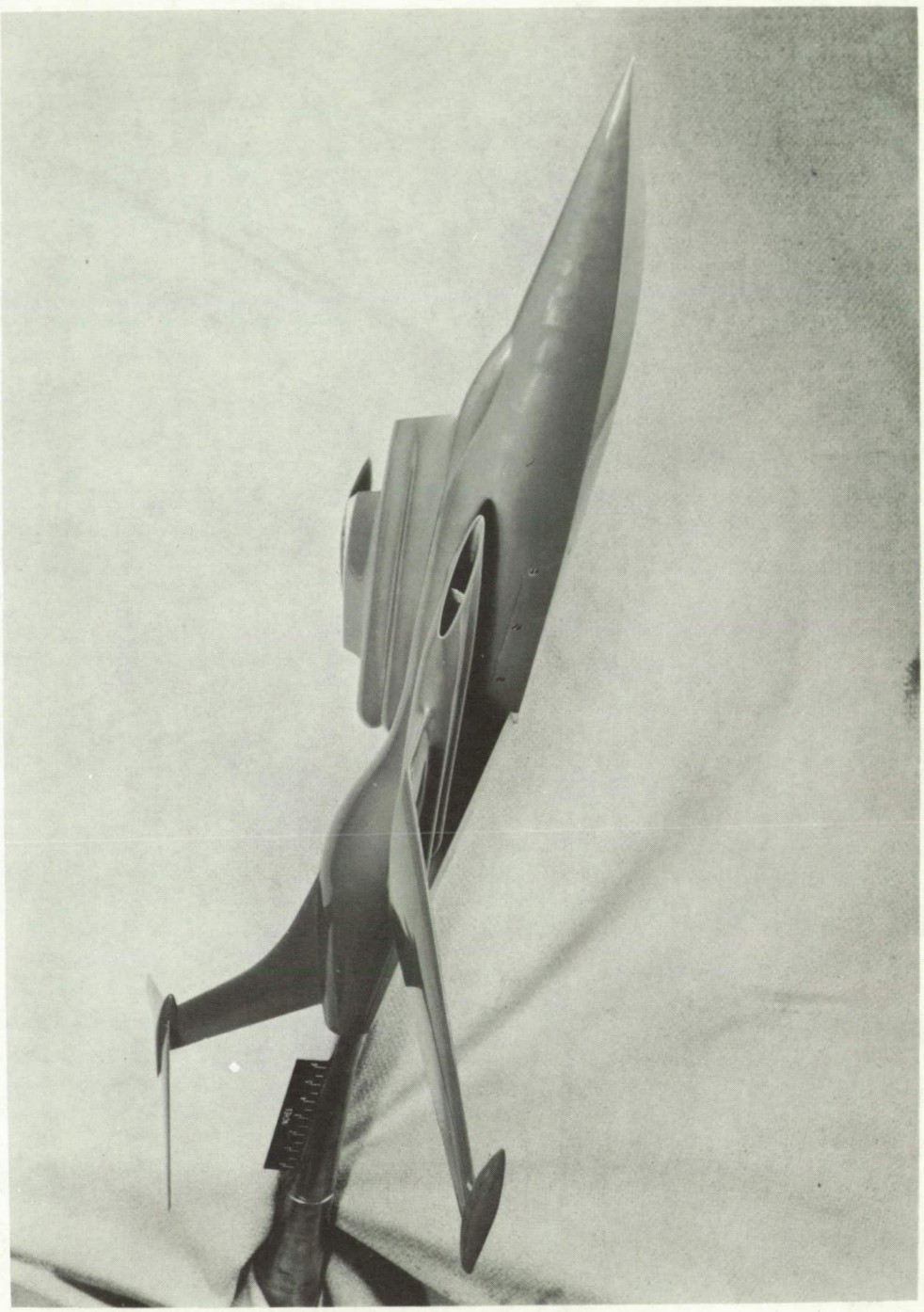

L-87491

(c) Three-quarter front view.

Figure 7.- Concluded.

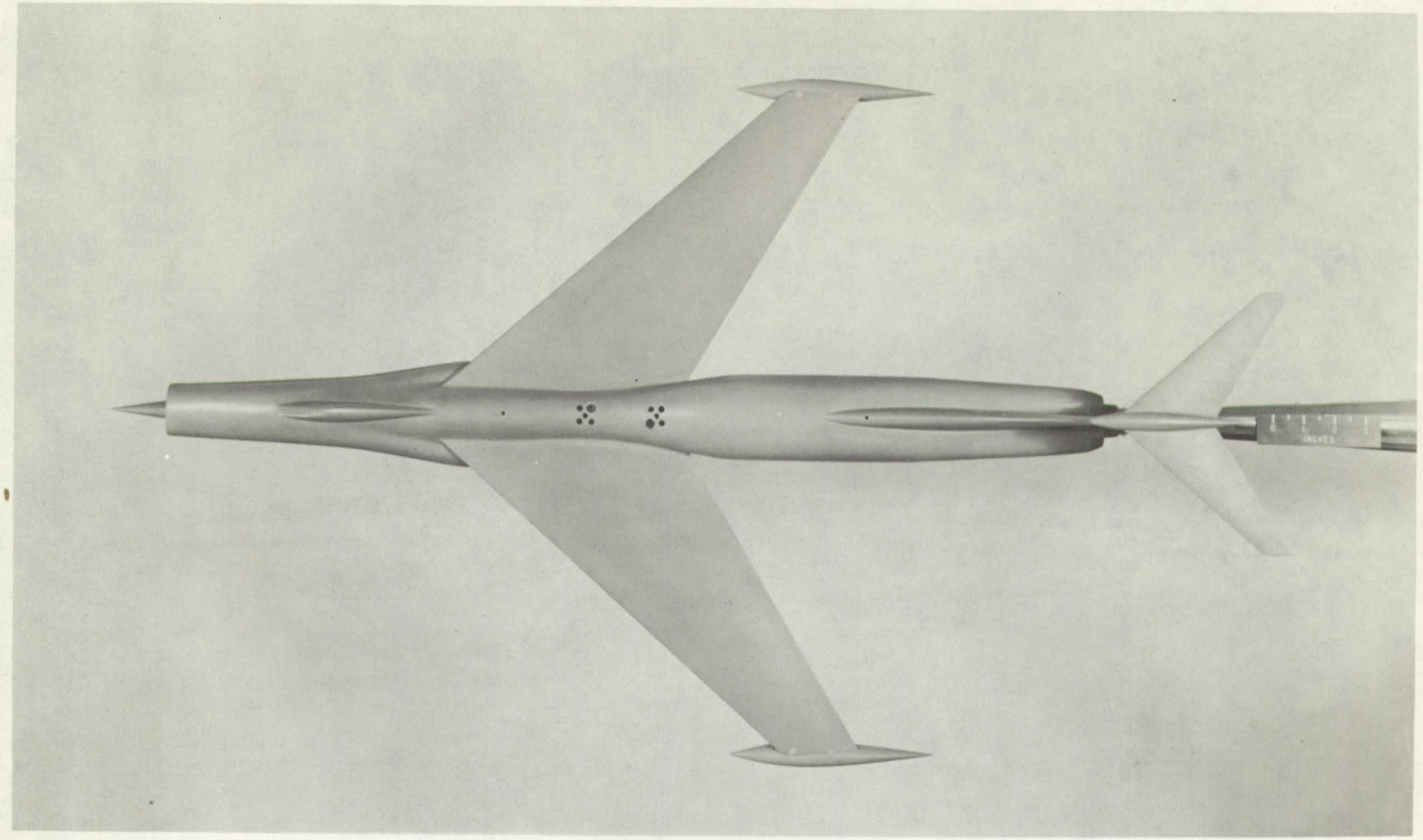

(a) Plan view.

L-87249

Figure 8.- Nose-inlet configuration tested in the Langley 8-foot transonic tunnel.

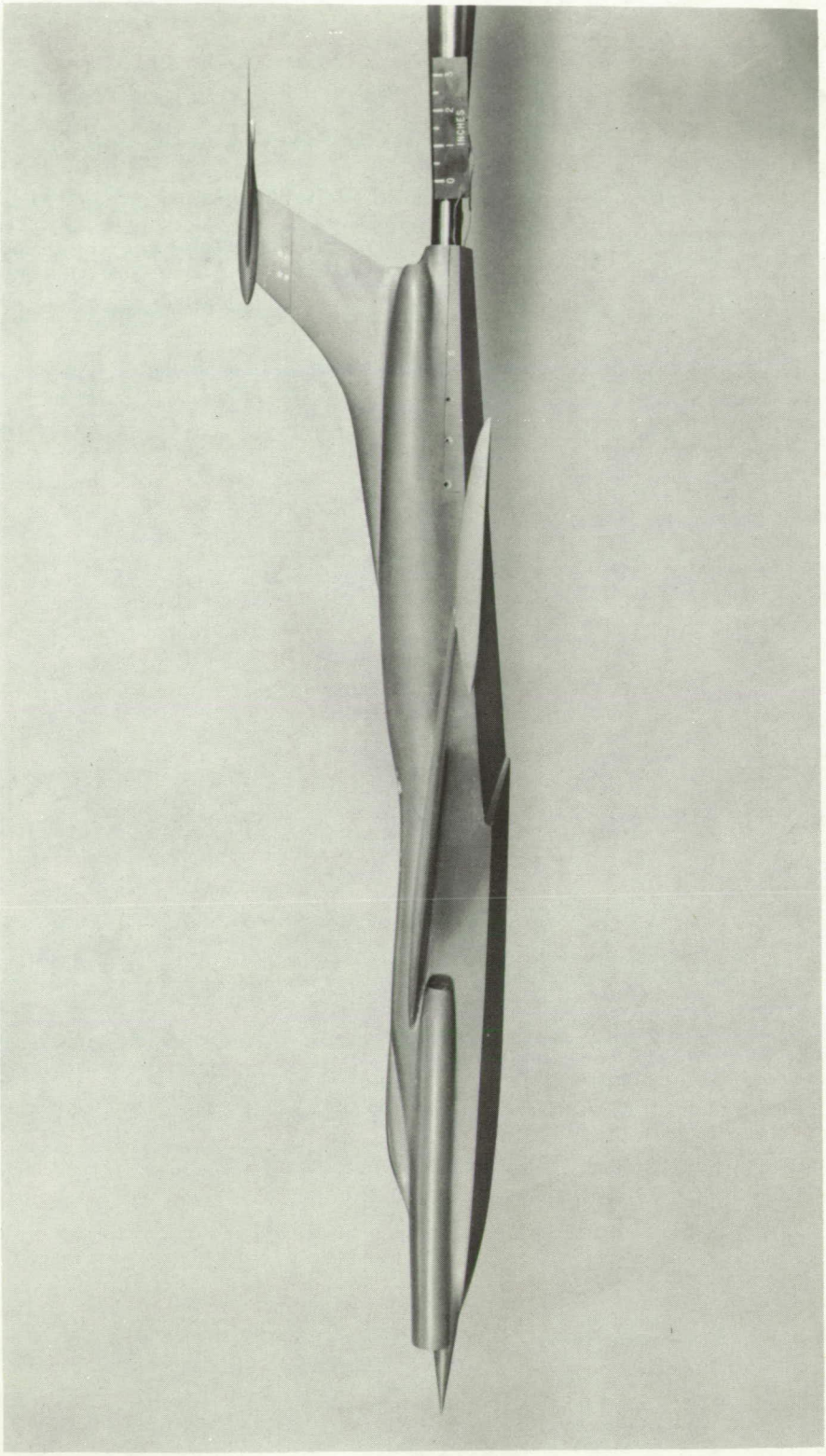

L-87247

(b) Side view.

Figure 8.- Continued.

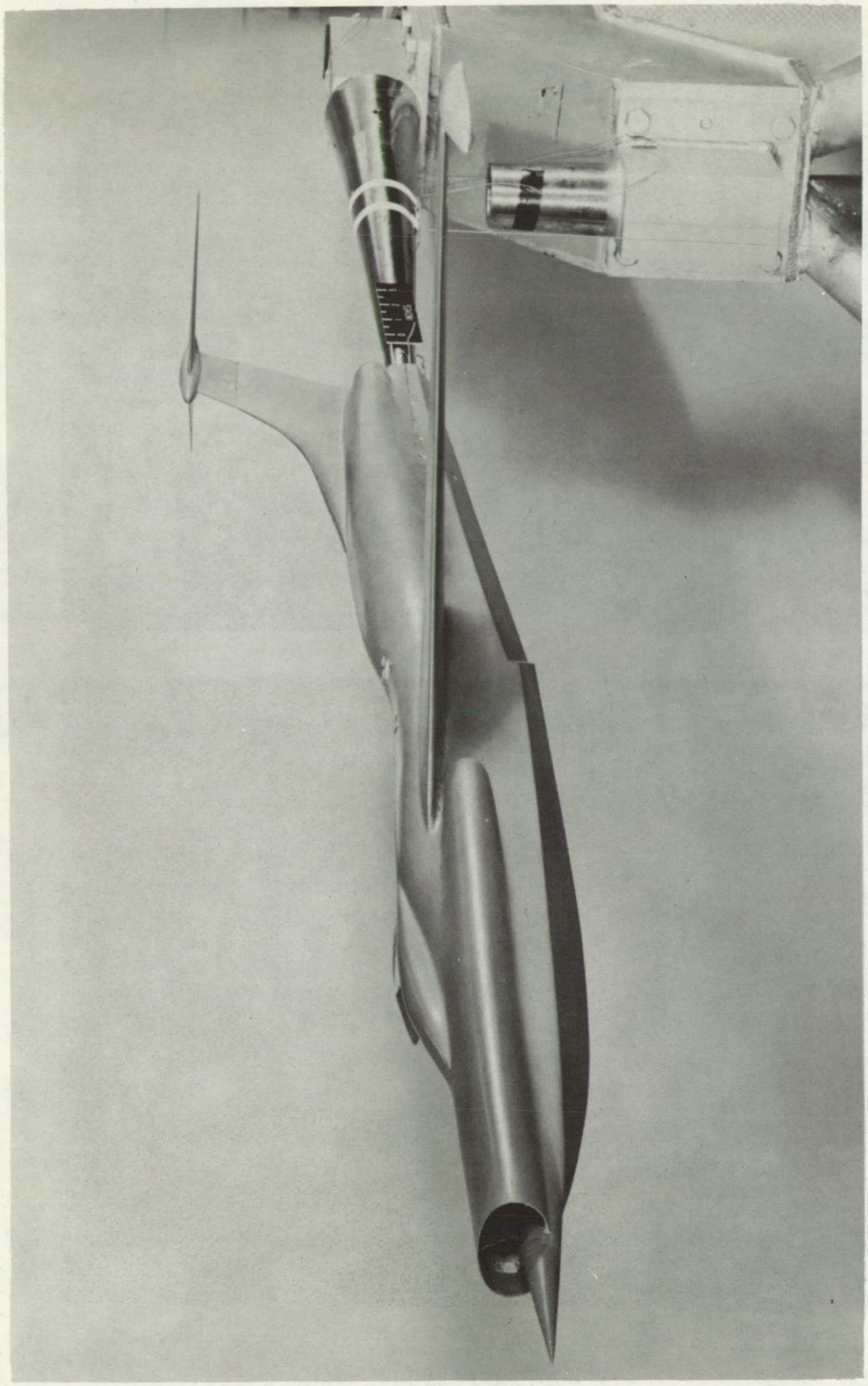

L-87248

(c) Three-quarter front view.

Figure 8.- Concluded.

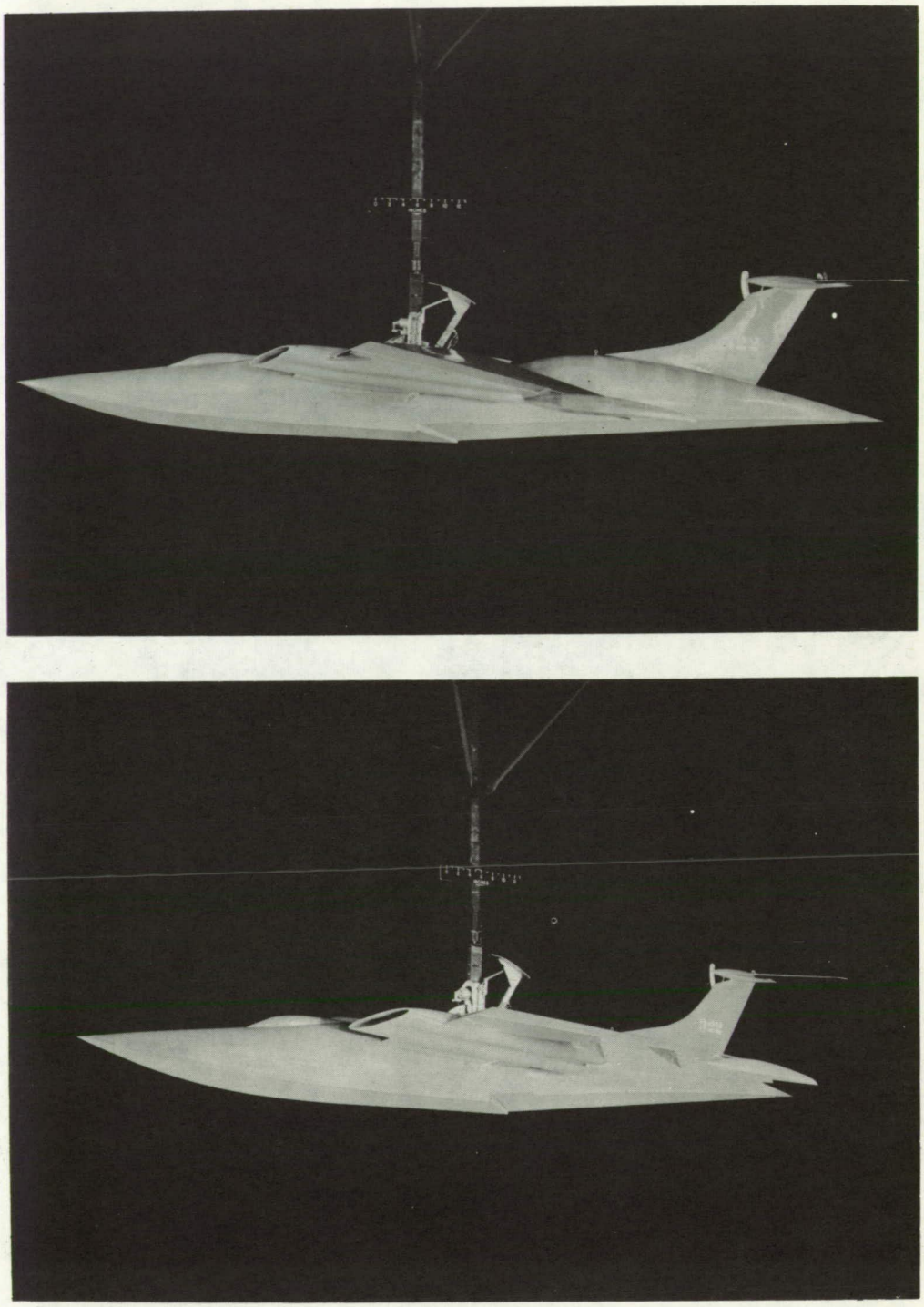

Figure 9.- Wing-root-inlet configuration. Tank model. L-87531

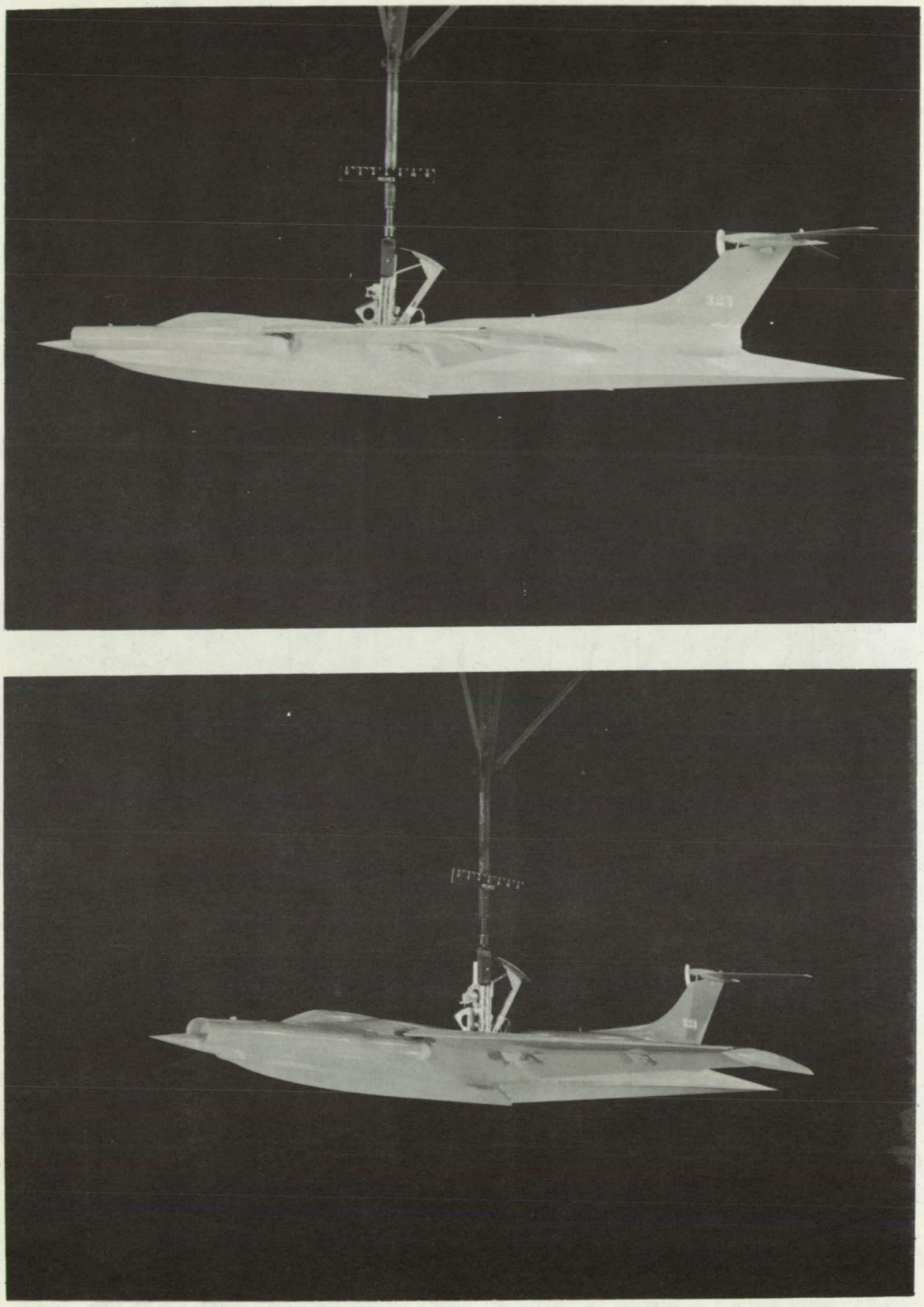

Figure 10.- Nose-inlet configuration. Tank model. L-87532

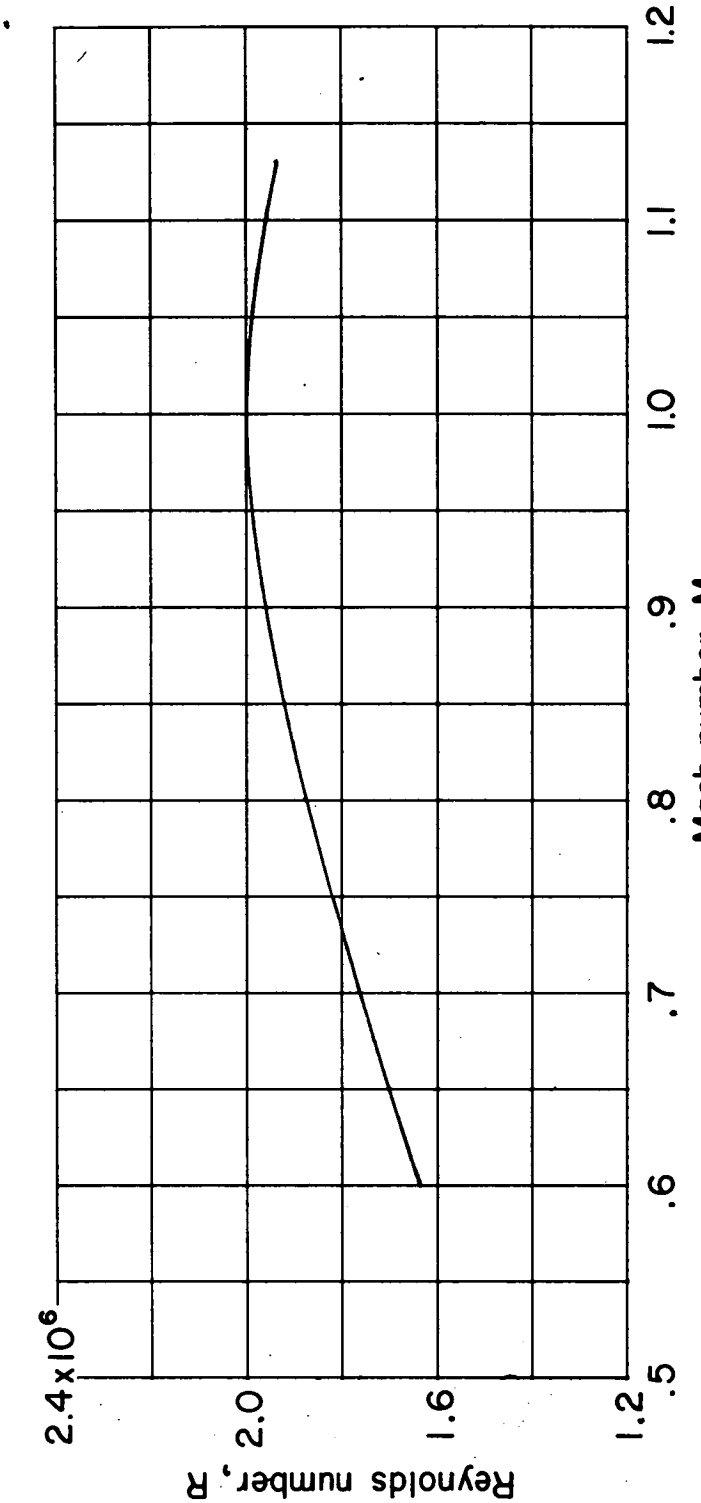

Figure 11.- Variation with Mach number of test Reynolds number based on wing mean aerodynamic chord.

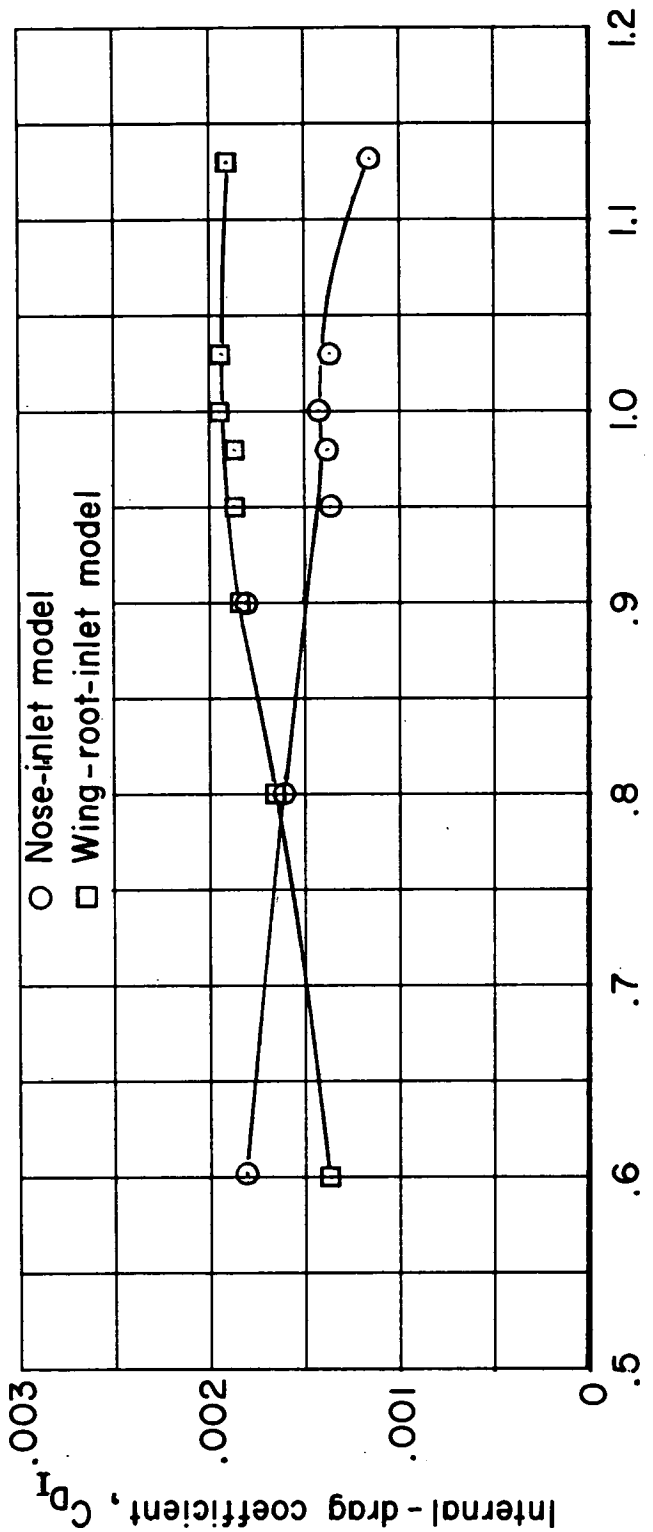

Figure 12.- Variation of internal-drag coefficient with Mach number for the two configurations. $\alpha \approx -2.5^{\circ}$.

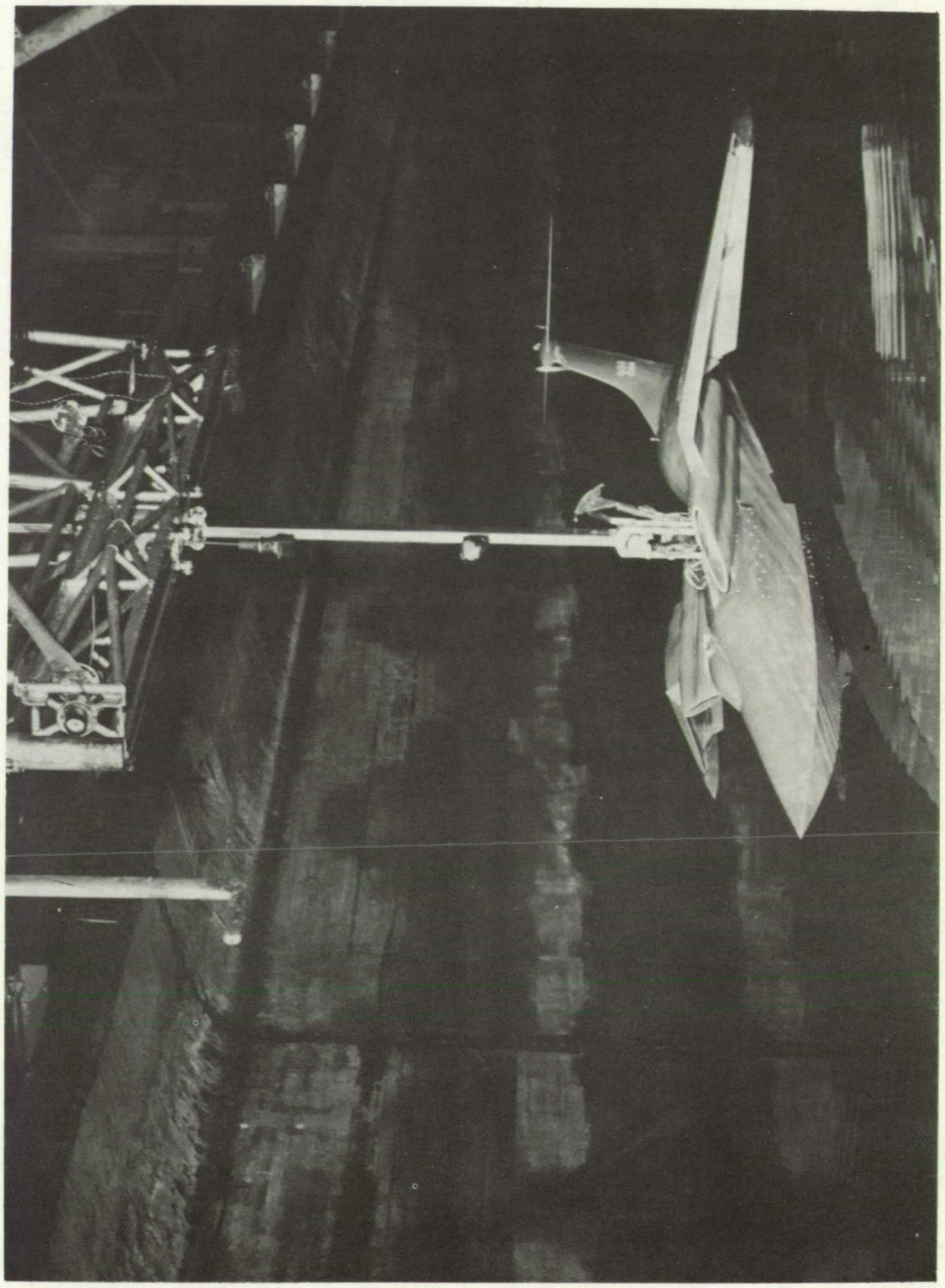

Figure 13.- Setup of model on towing carriage. L-87533

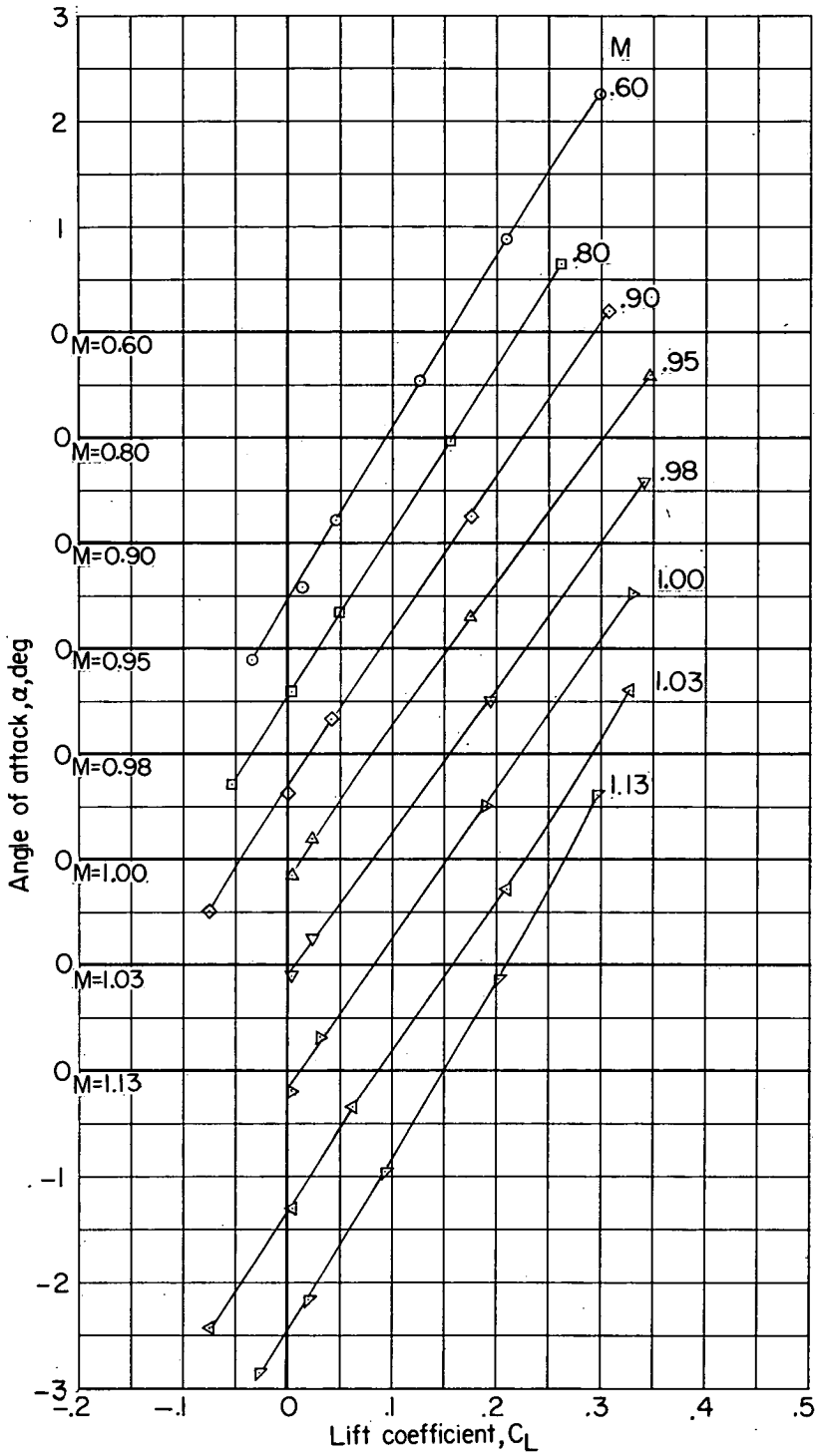

(a) Angle of attack.

Figure 14.- Aerodynamic characteristics of nose-inlet configuration. $\delta_s = 0^o$.

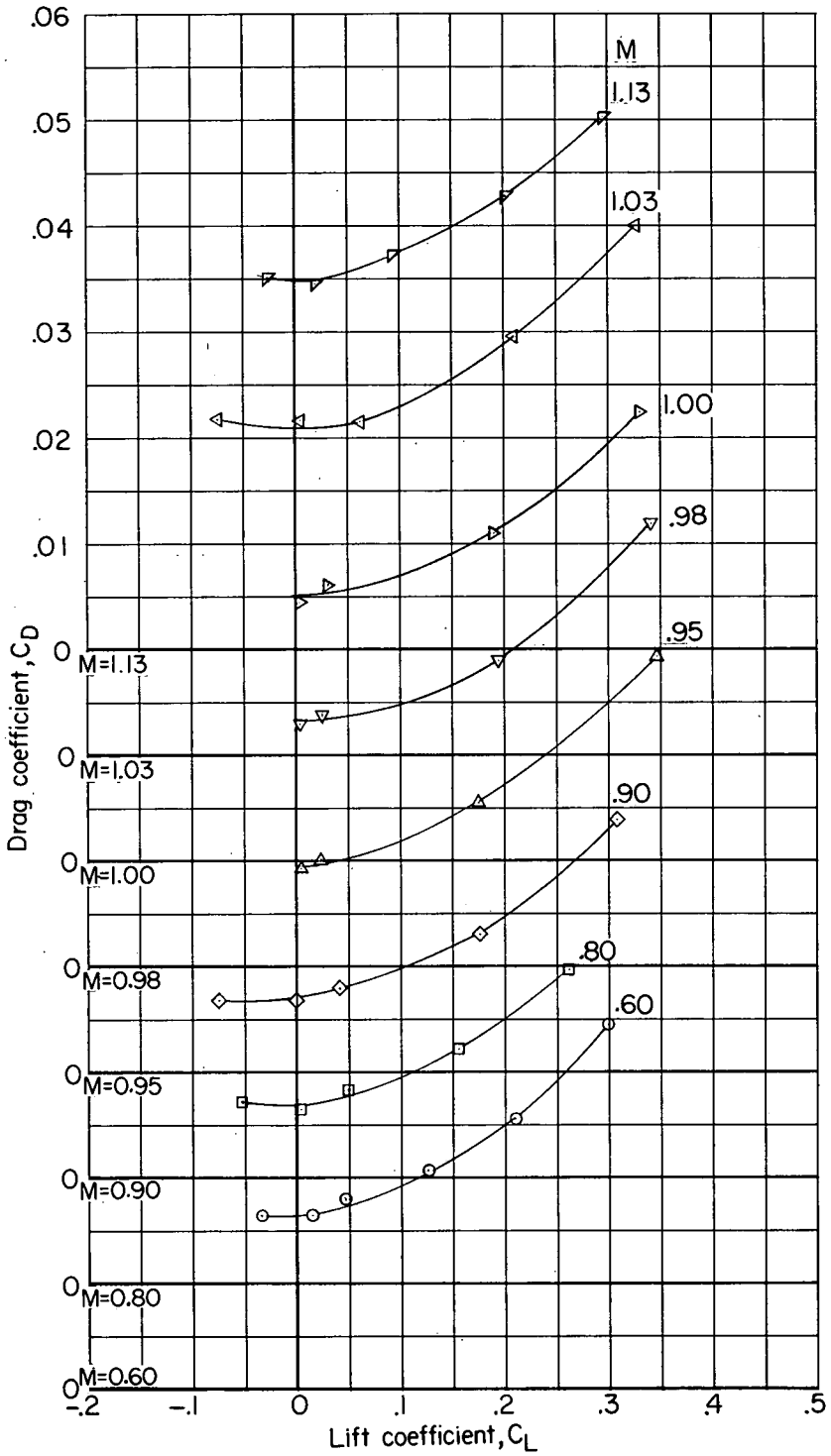

(b) Drag coefficient.

Figure 14.- Continued.

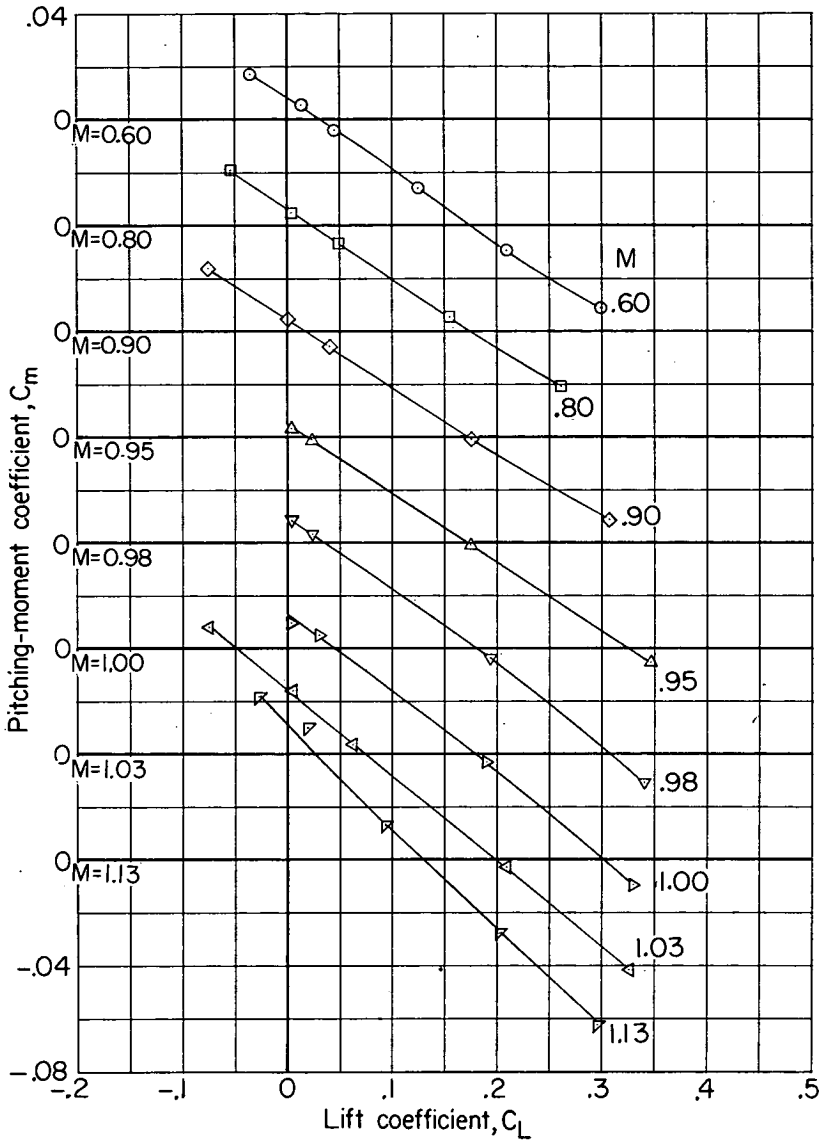

(c) Pitching-moment coefficient.

Figure 14.- Concluded.

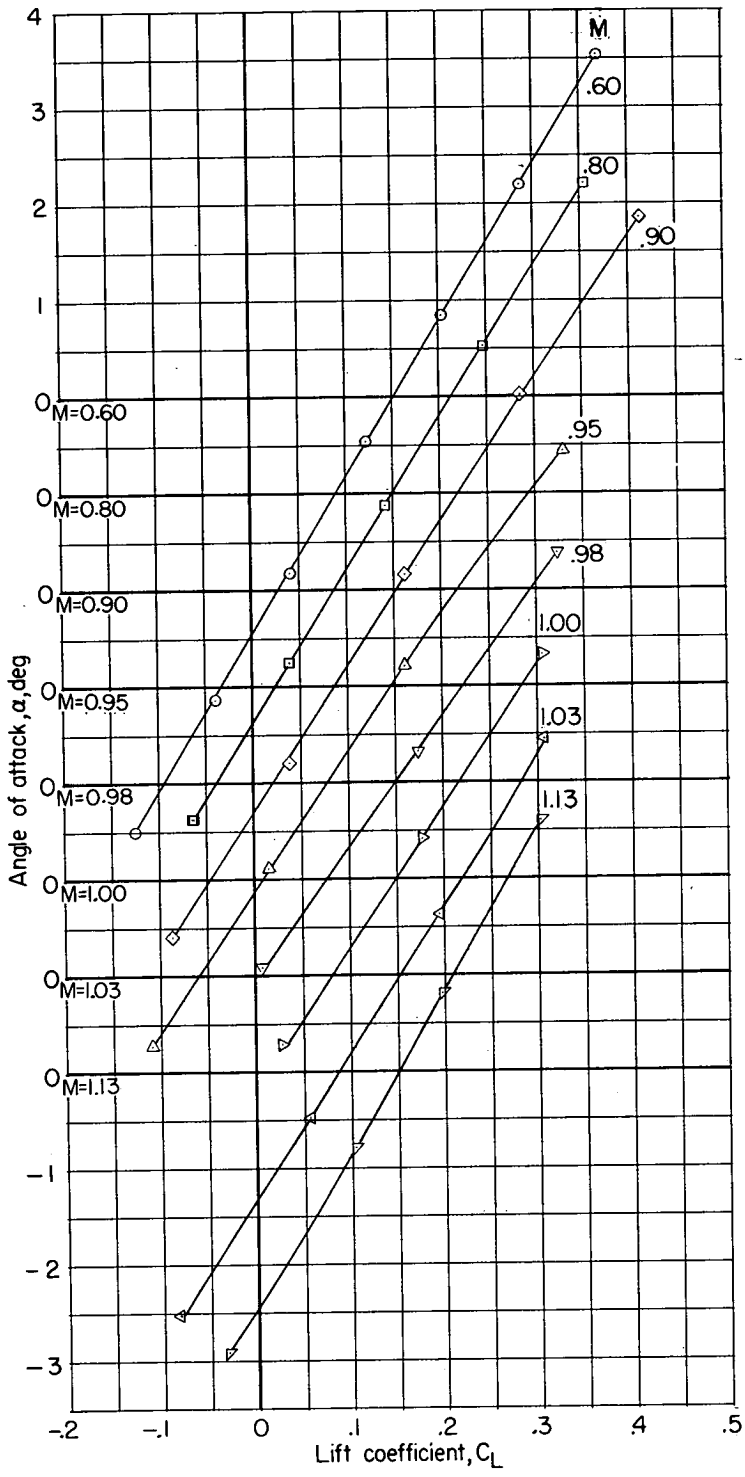

(a) Angle of attack.

Figure 15.- Aerodynamic characteristics of nose-inlet configuration with chine strips. $\delta_s = 0^o$.

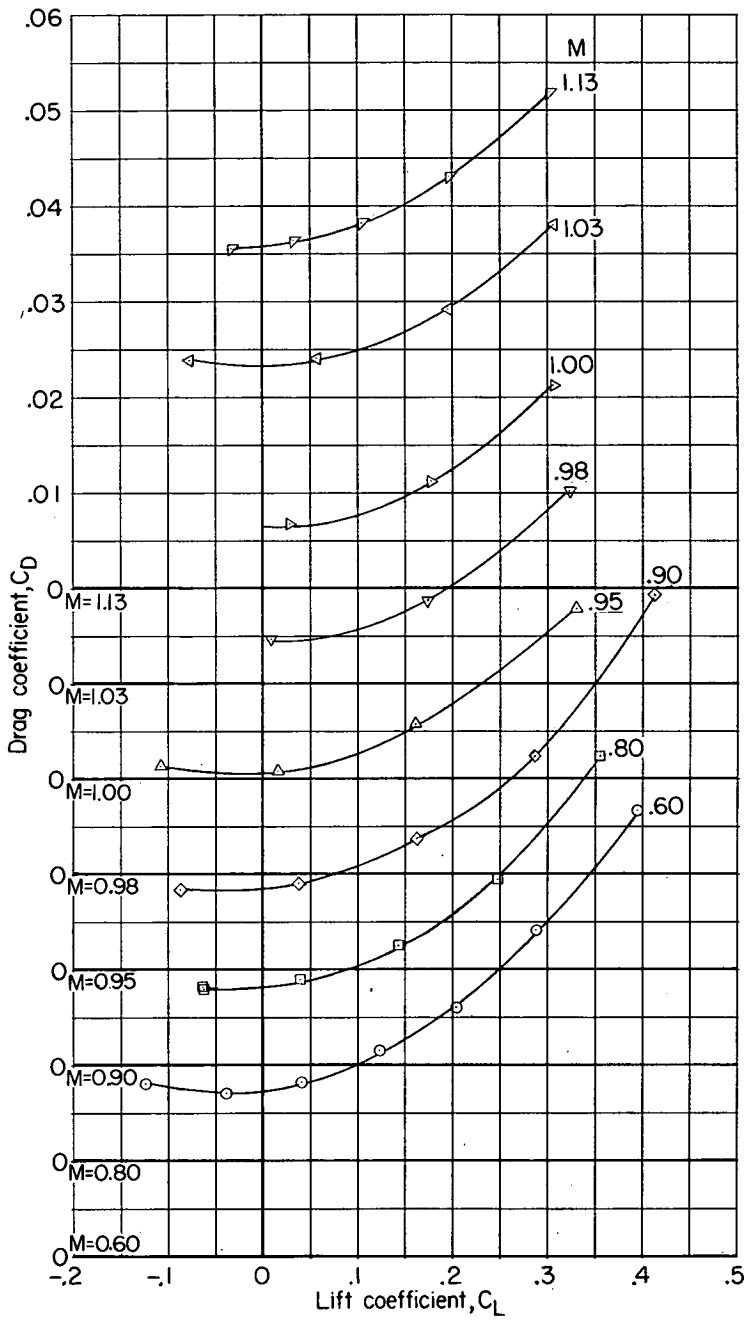

(b) Drag coefficient.

Figure 15.- Continued.

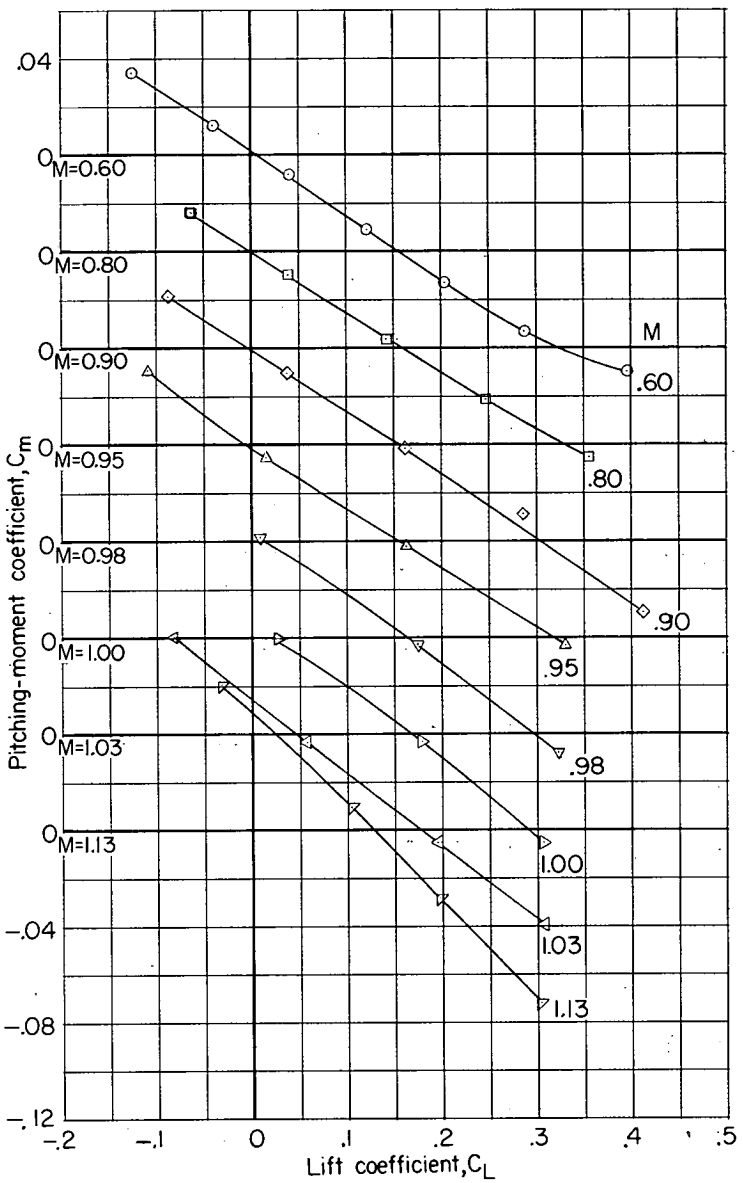

(c) Pitching-moment coefficient.

Figure 15.- Concluded.

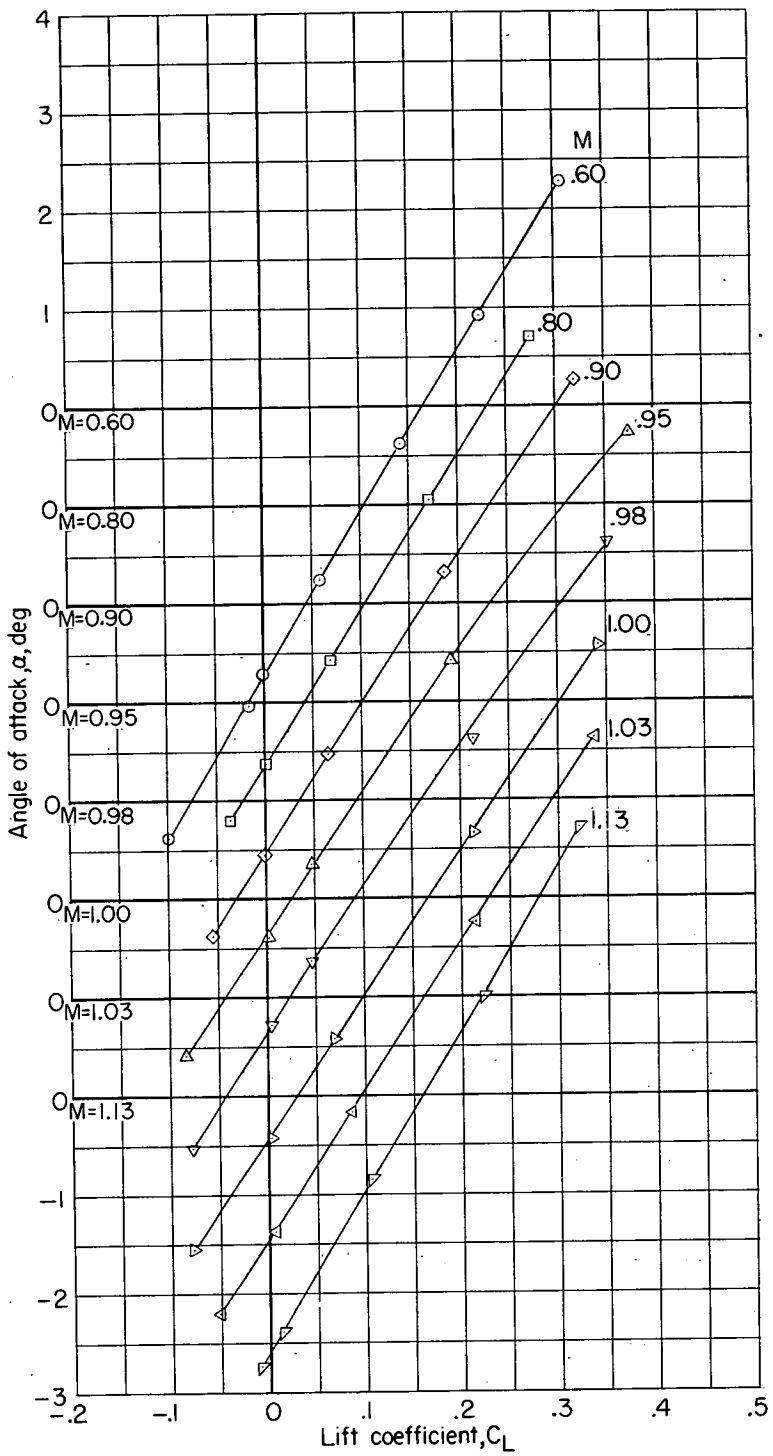

(a) Angle of attack.

Figure 16.- Aerodynamic characteristics of nose-inlet configuration with breaker strips. $\delta_s = 0^\circ$.

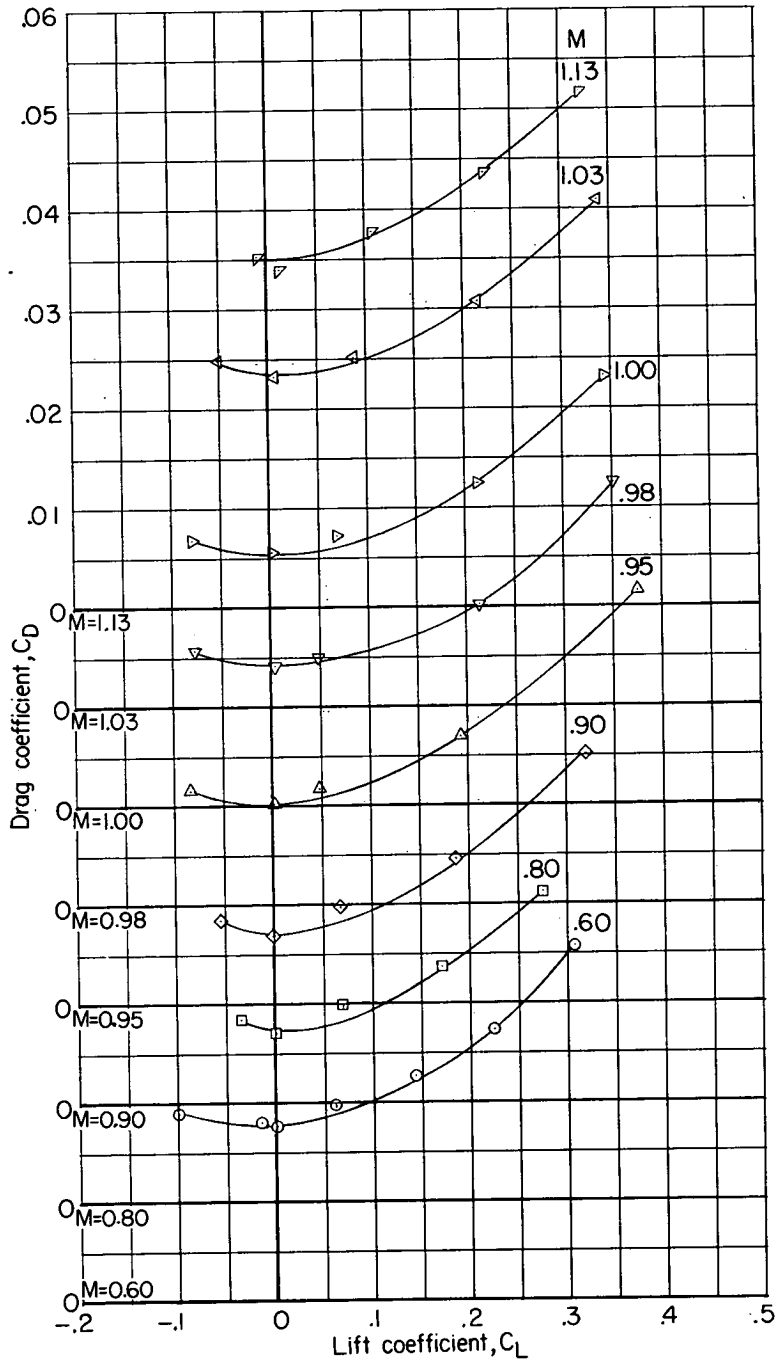

(b) Drag coefficient.

Figure 16.- Continued.

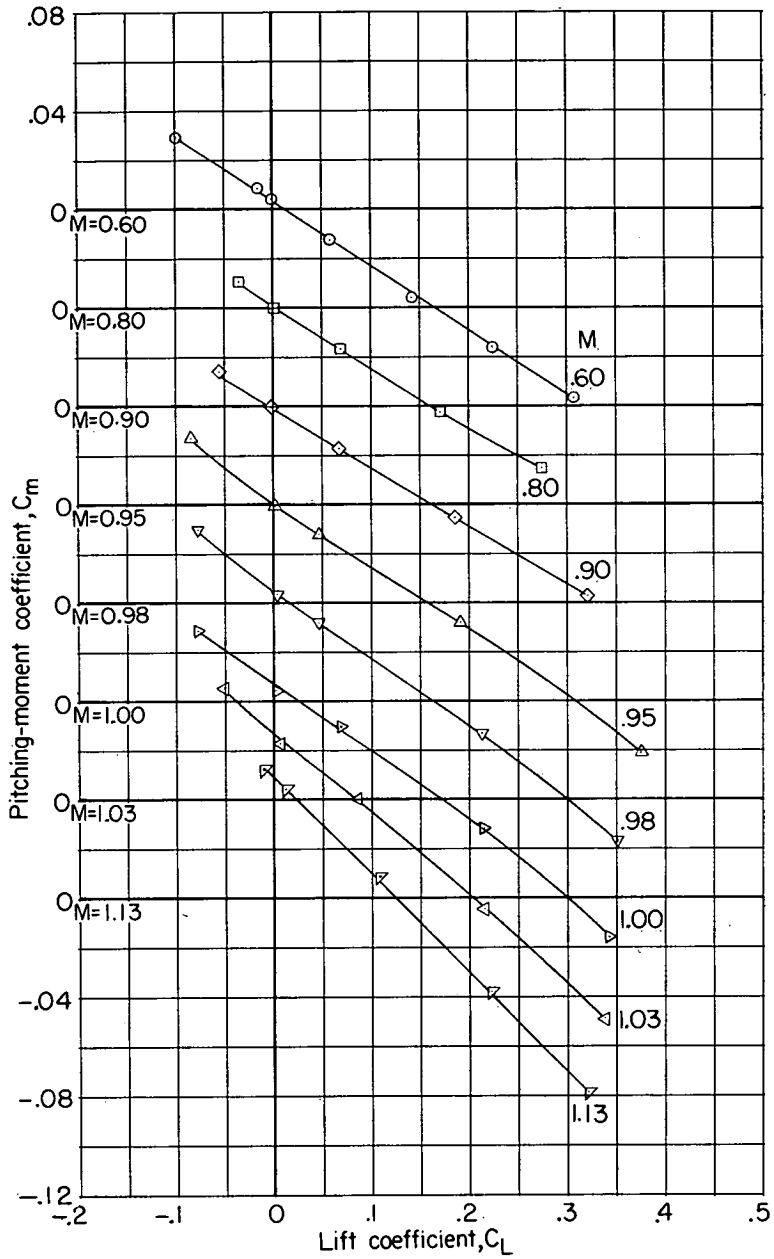

(c) Pitching-moment coefficient.

Figure 16.- Concluded.

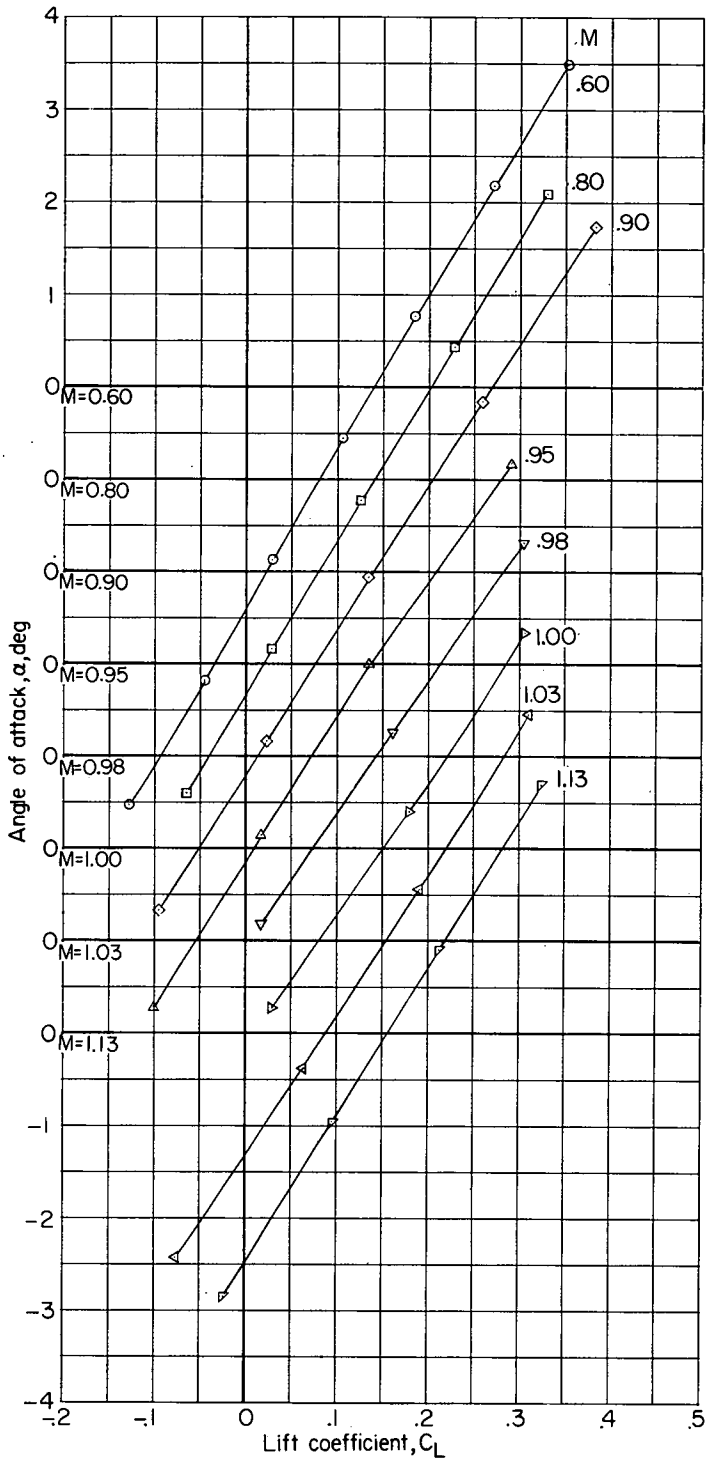

(a) Angle of attack.

Figure 17.- Aerodynamic characteristics of nose-inlet configuration with step fairing. $\delta_s = 0^o$.

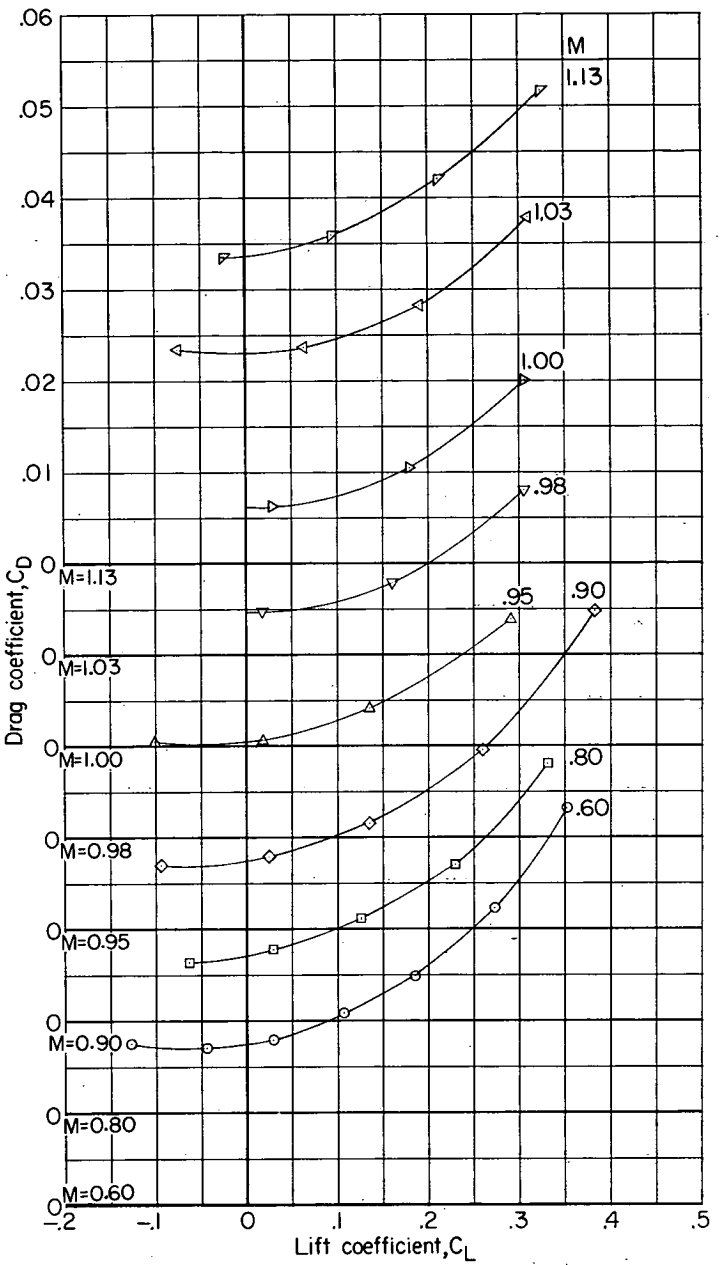

(b) Drag coefficient.

Figure 17.- Continued.

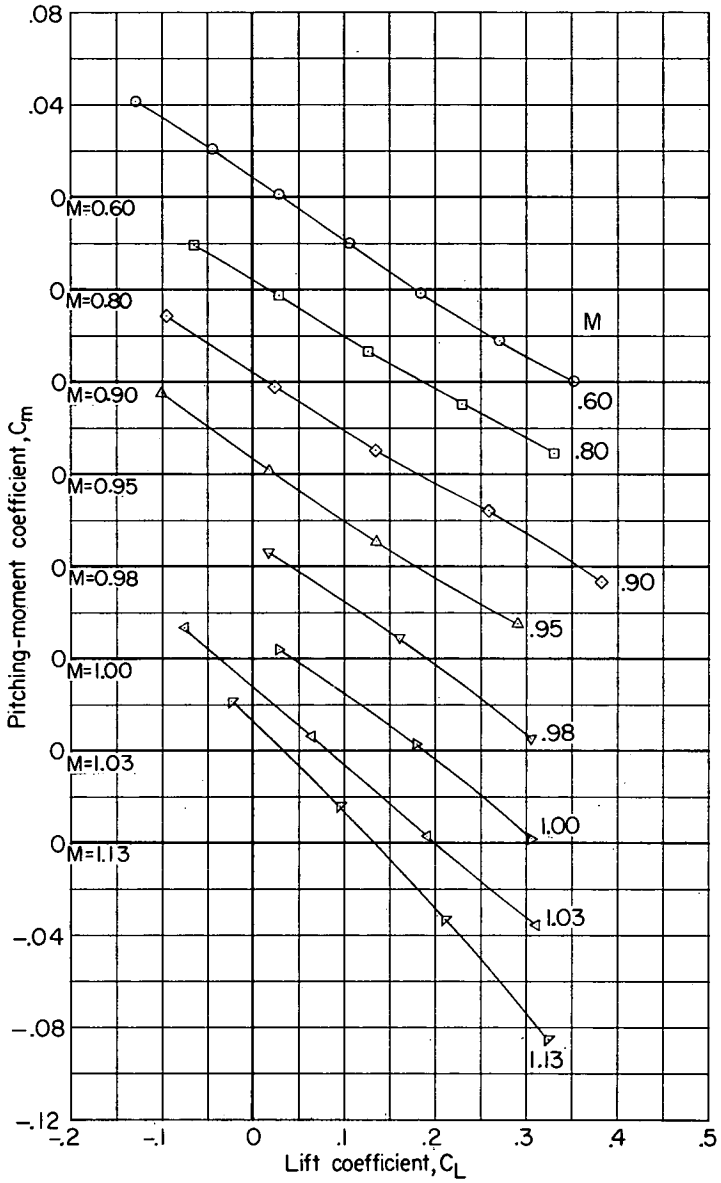

(c) Pitching-moment coefficient.

Figure 17.- Concluded.

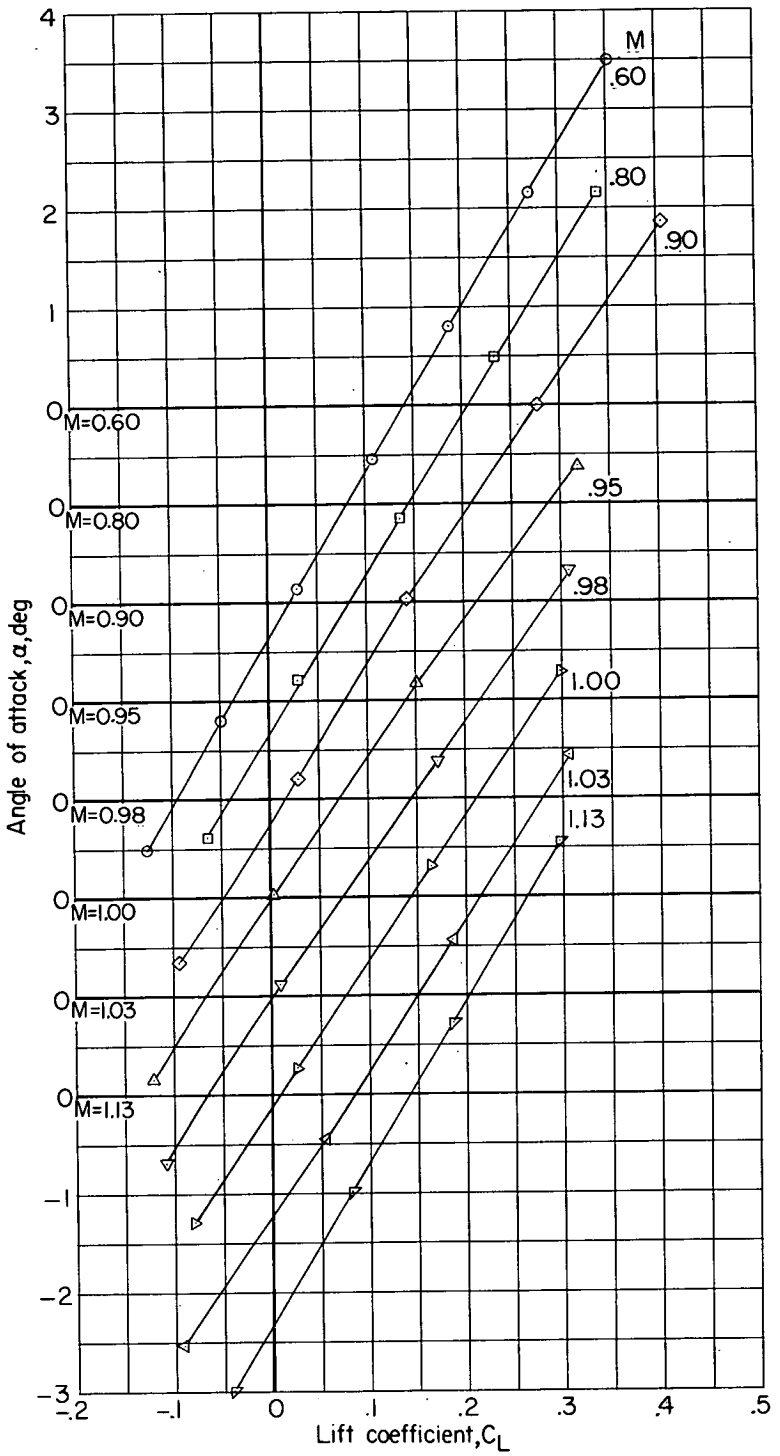

(a) Angle of attack.

Figure 18.- Aerodynamic characteristics of nose-inlet configuration with wing tip floats off. $\delta_s = 0^o$.

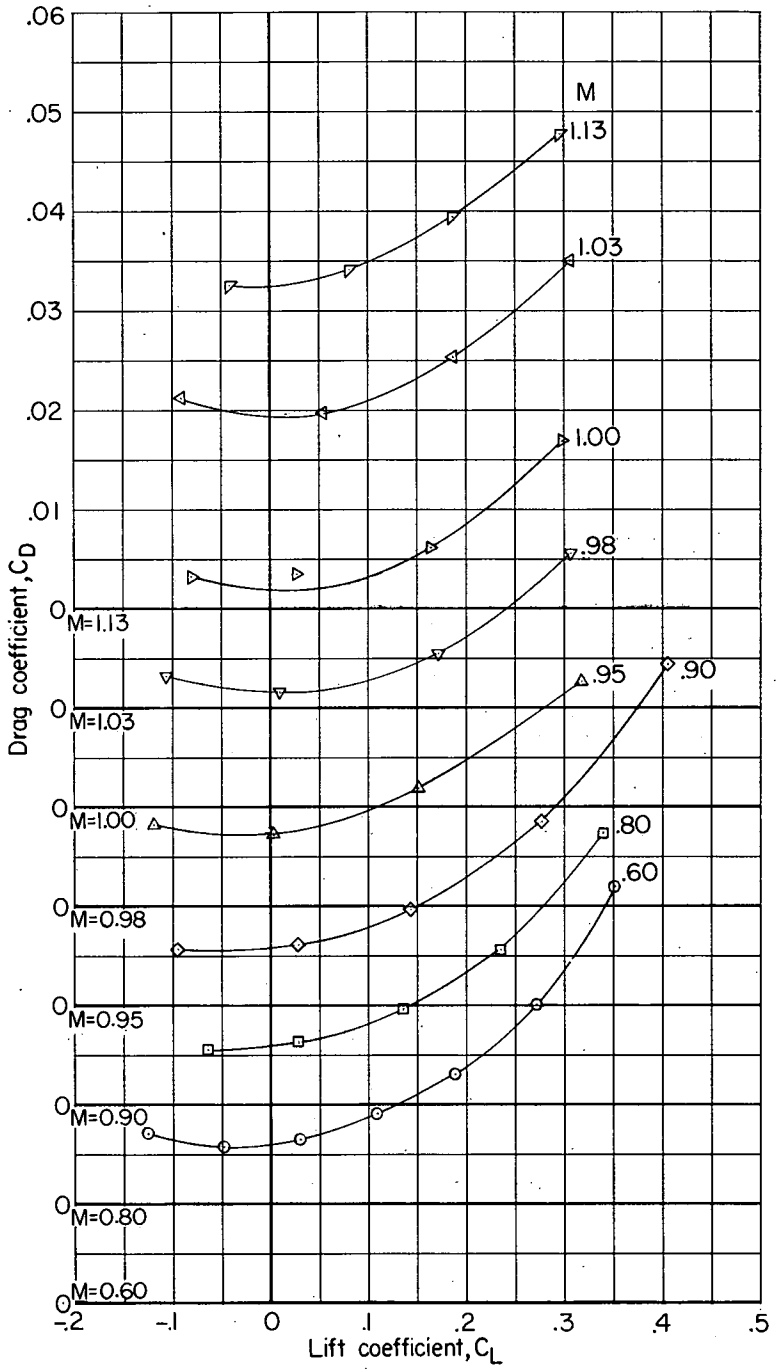

(b) Drag coefficient.

Figure 18.- Continued.

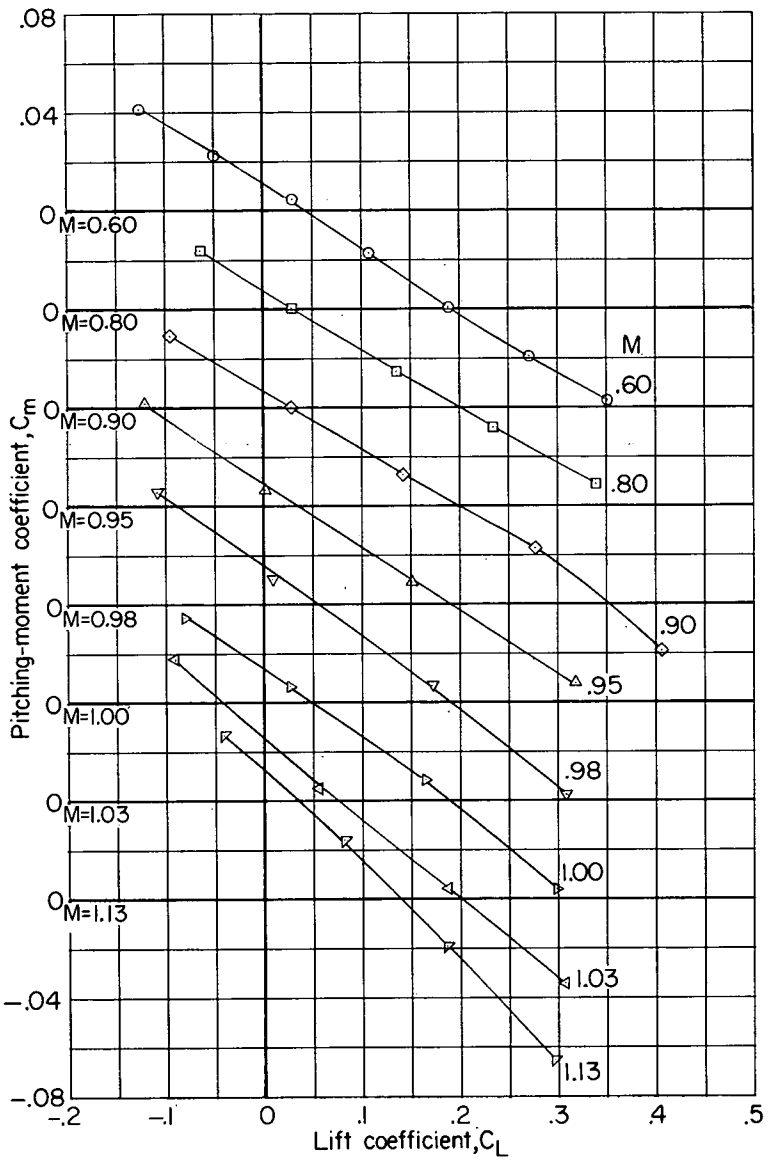

(c) Pitching-moment coefficient.

Figure 18.- Concluded.

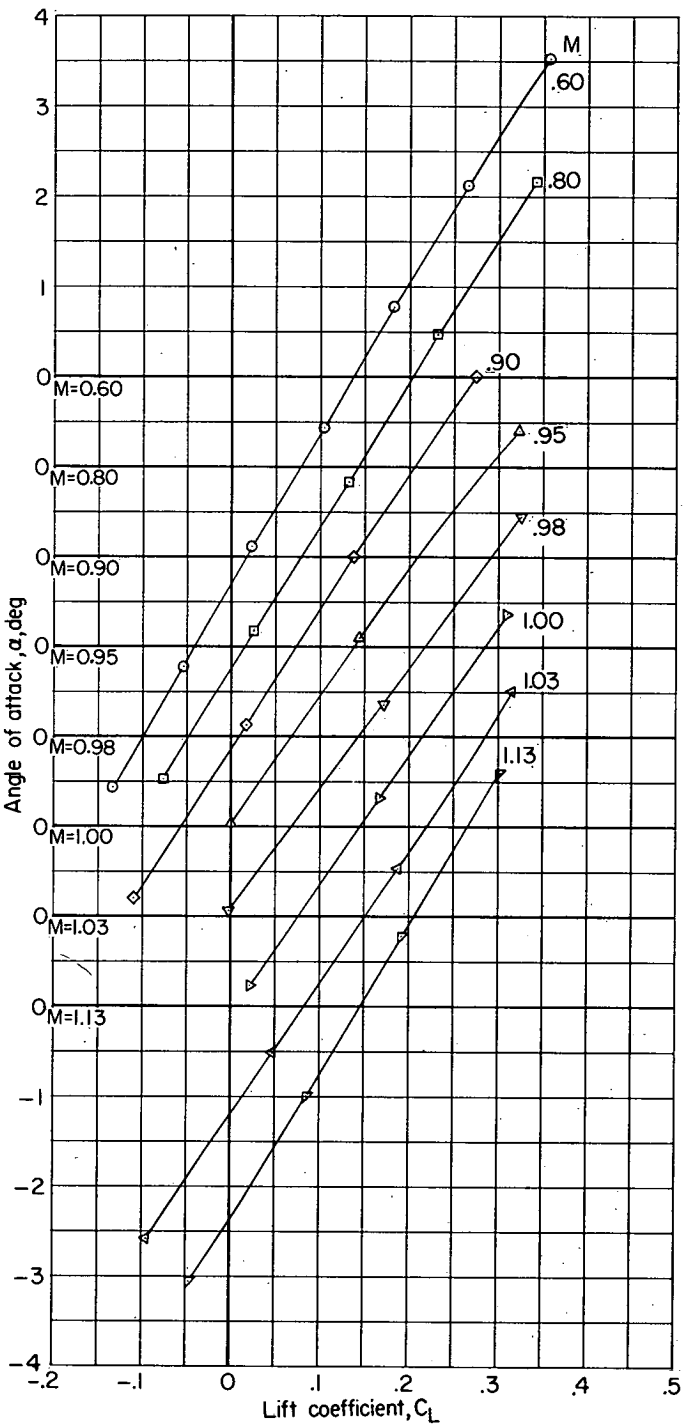

(a) Angle of attack.

Figure 19.- Aerodynamic characteristics of nose-inlet configurations with wing tip floats off, but with equivalent area of wing tip floats added to hull. $\delta_s = 0^o$.

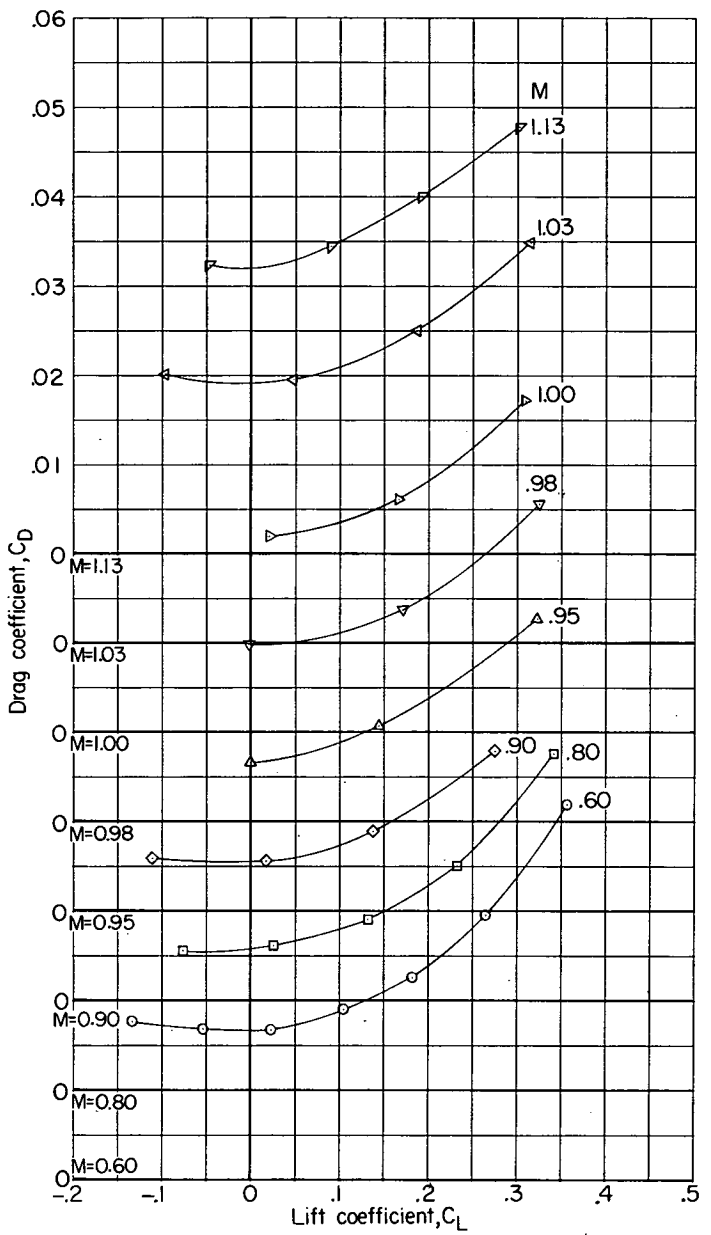

(b) Drag coefficient.

Figure 19.- Continued.

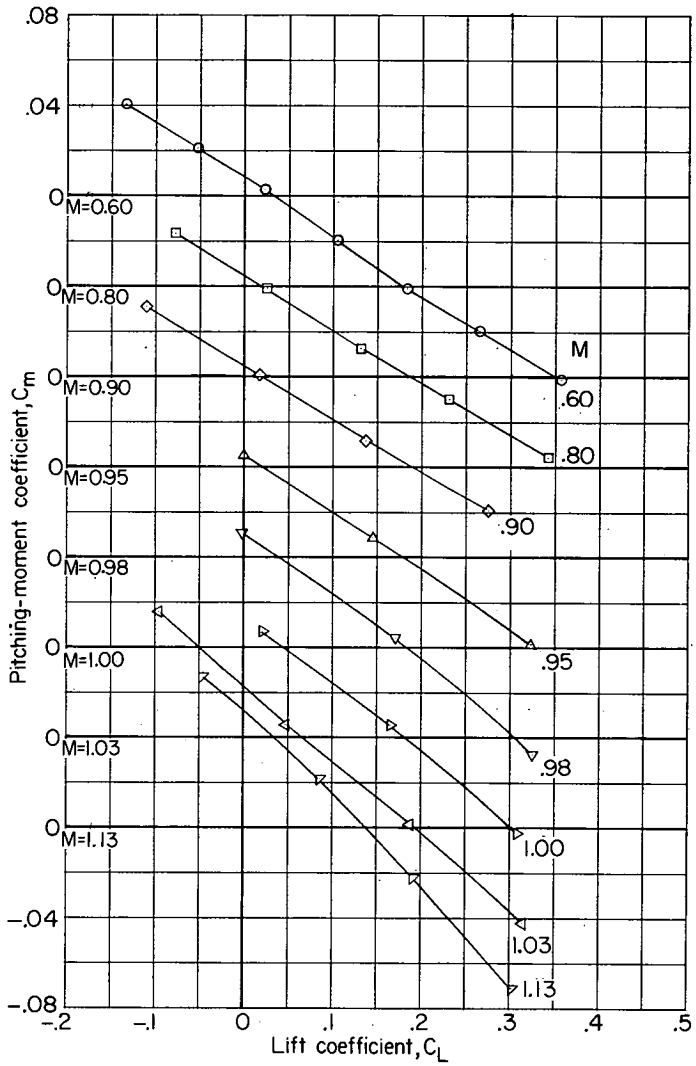

(c) Pitching-moment coefficient.

Figure 19.- Concluded.

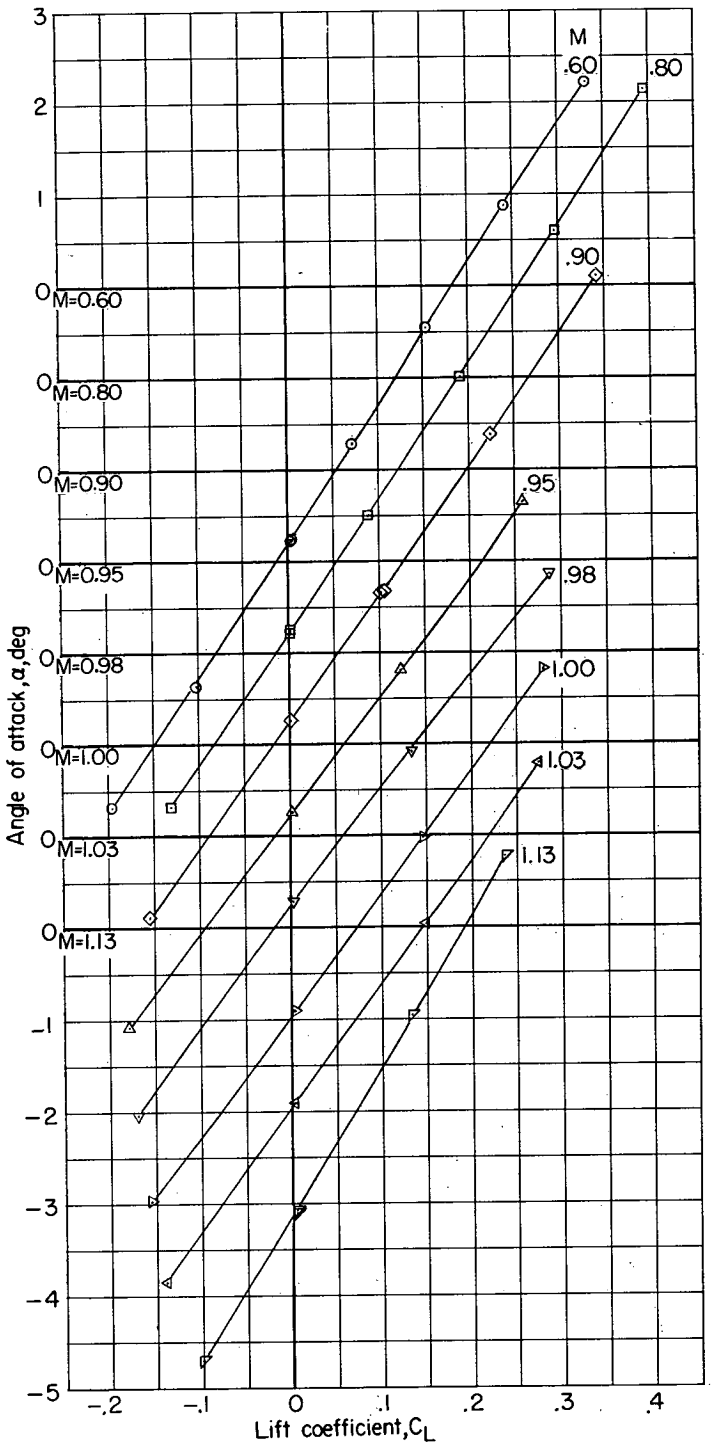

(a) Angle of attack.

Figure 20.- Aerodynamic characteristics of wing-root-inlet configuration. $\delta_s = 0^o$.

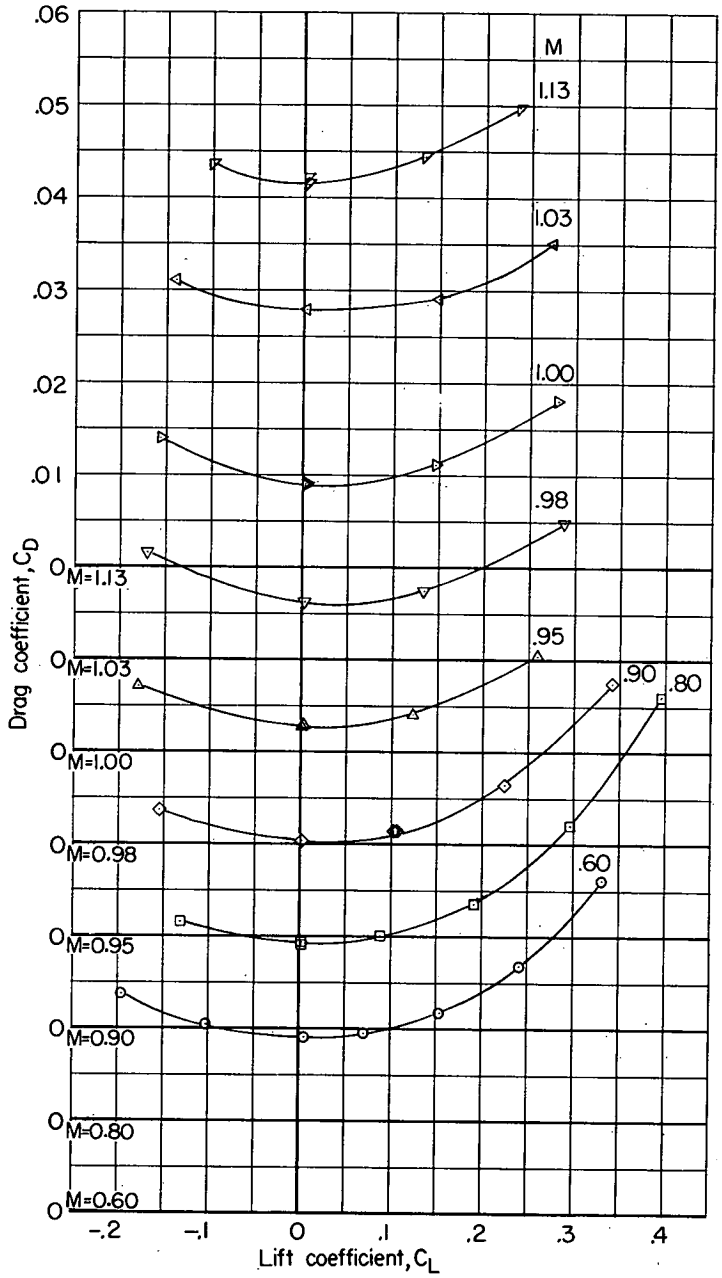

(b) Drag coefficient.

Figure 20.- Continued.

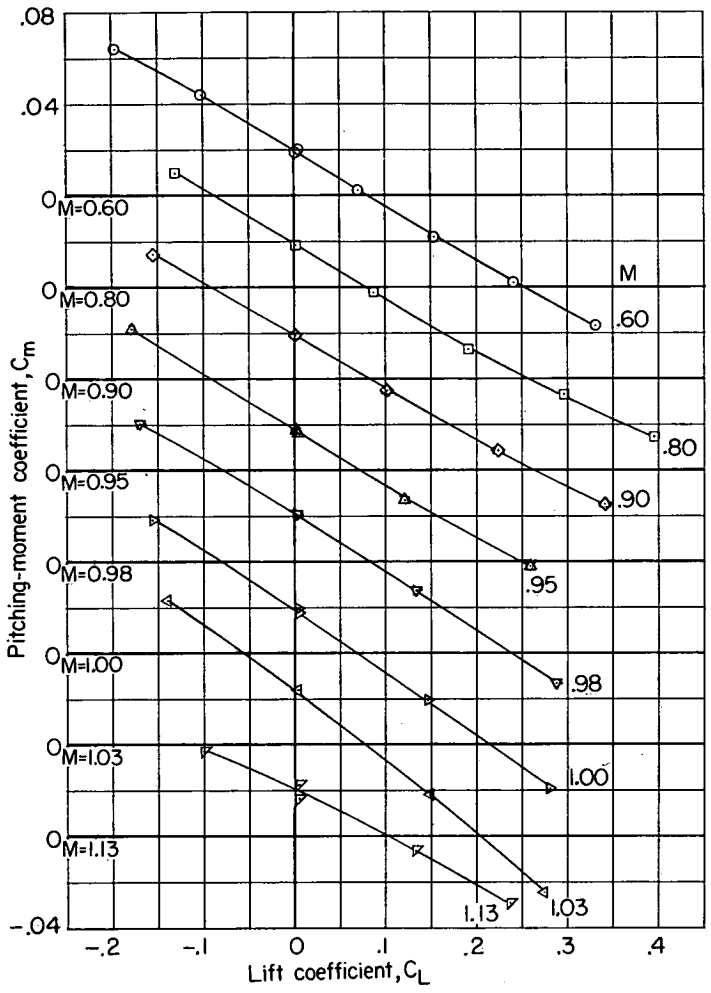

(c) Pitching-moment coefficient.

Figure 20.- Concluded.

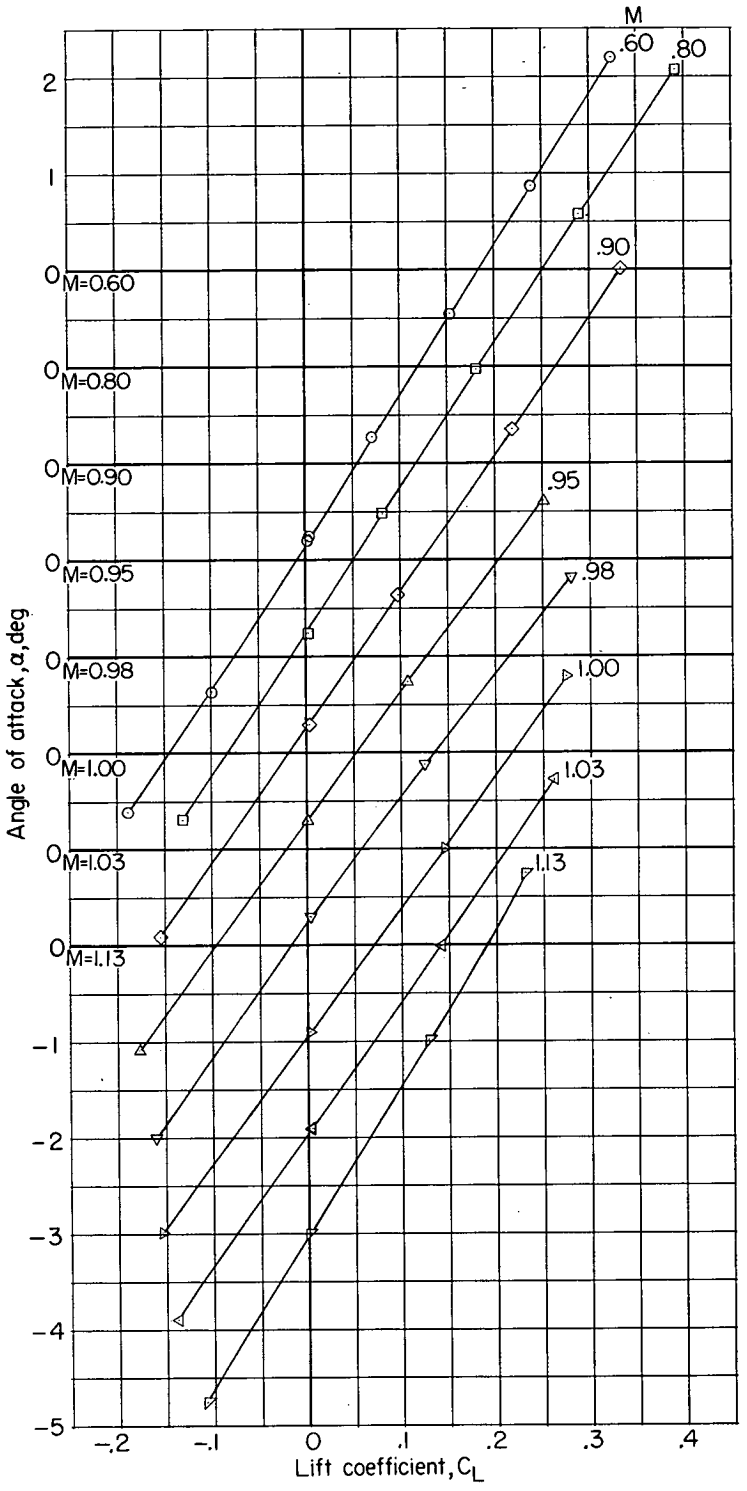

(a) Angle of attack.

Figure 21.- Aerodynamic characteristics of wing-root-inlet configuration with wing tip floats off. $\delta_s = 0^o$.

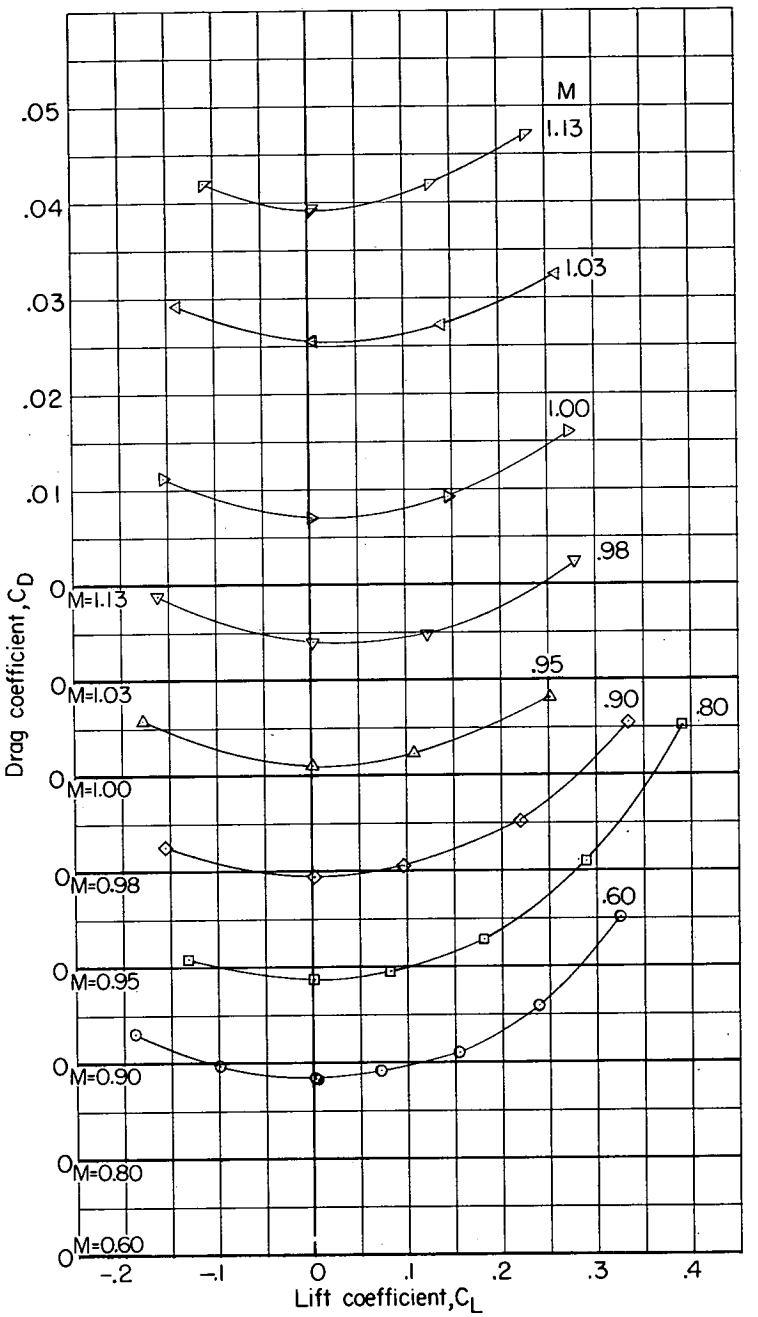

(b) Drag coefficient.

Figure 21.- Continued.

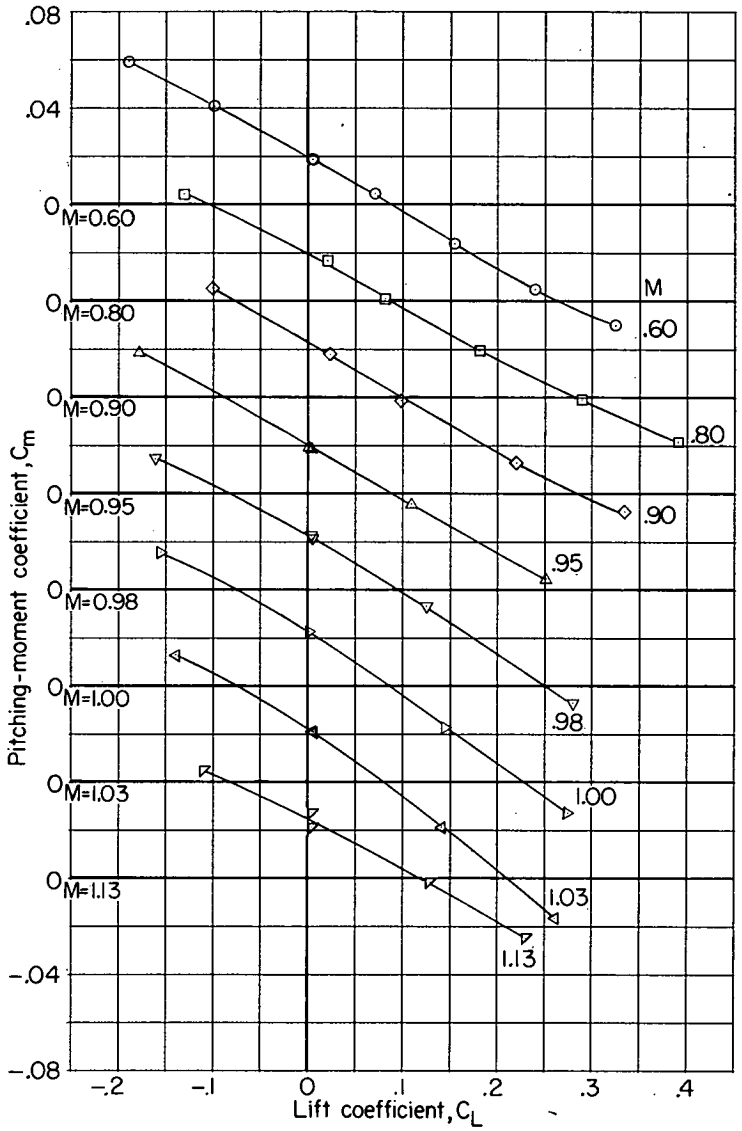

(c) Pitching-moment coefficient.

Figure 21.- Concluded.

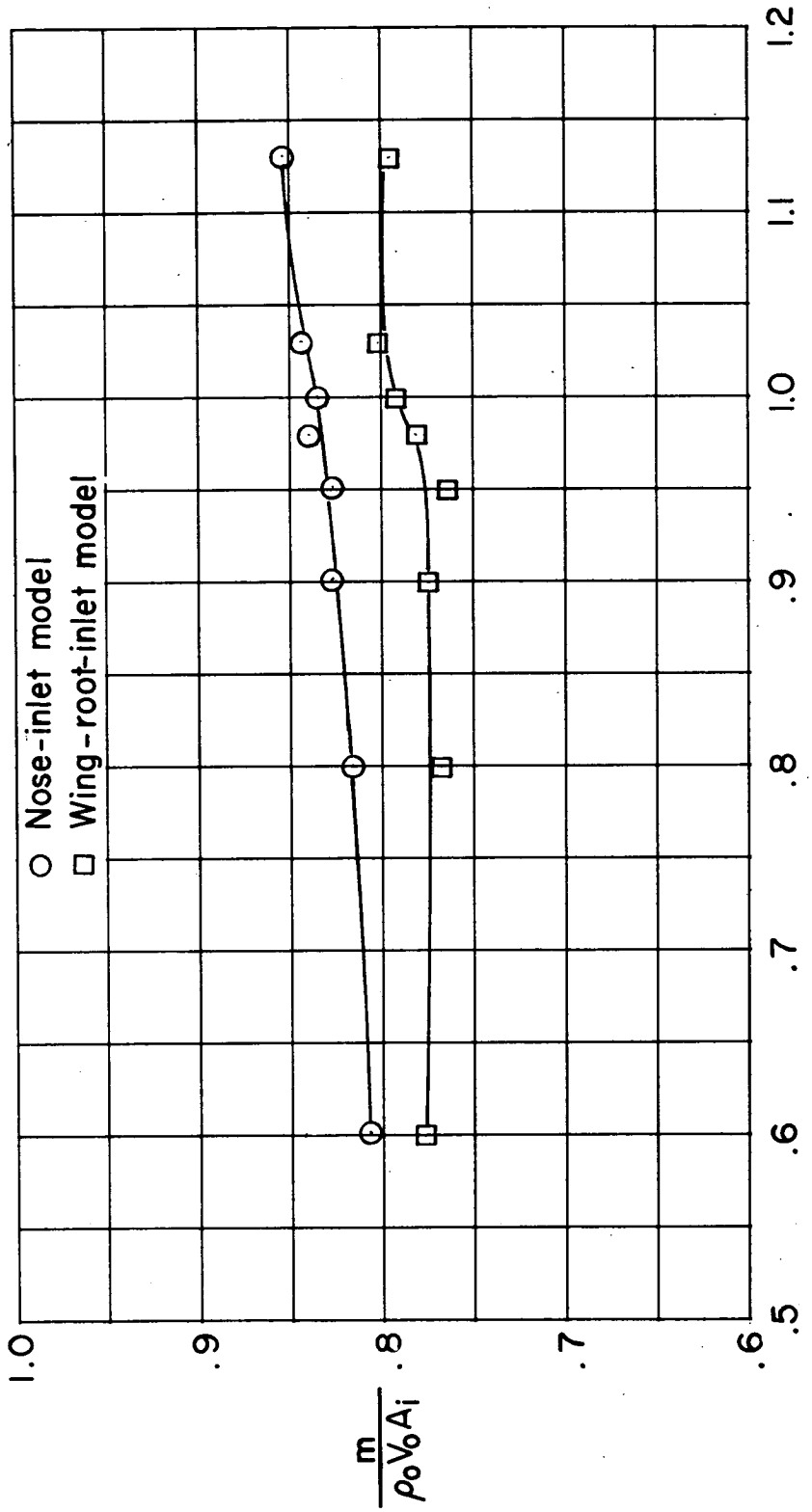

Figure 22.- Variation of mass-flow ratio with Mach number for the two configurations. $\alpha \approx -2.5^\circ$.

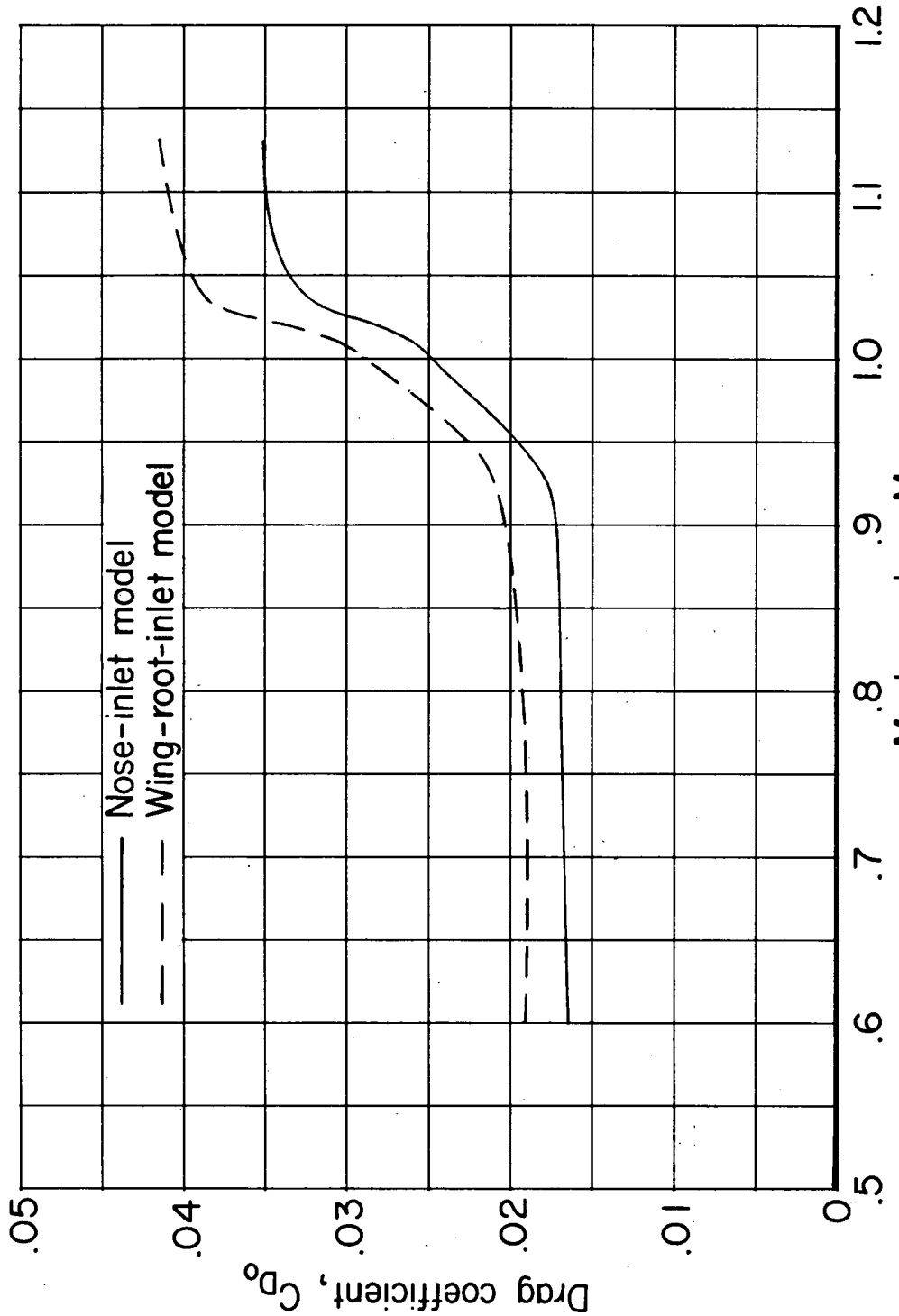

Figure 23.- A comparison of the zero-lift drag coefficients of the two configurations.

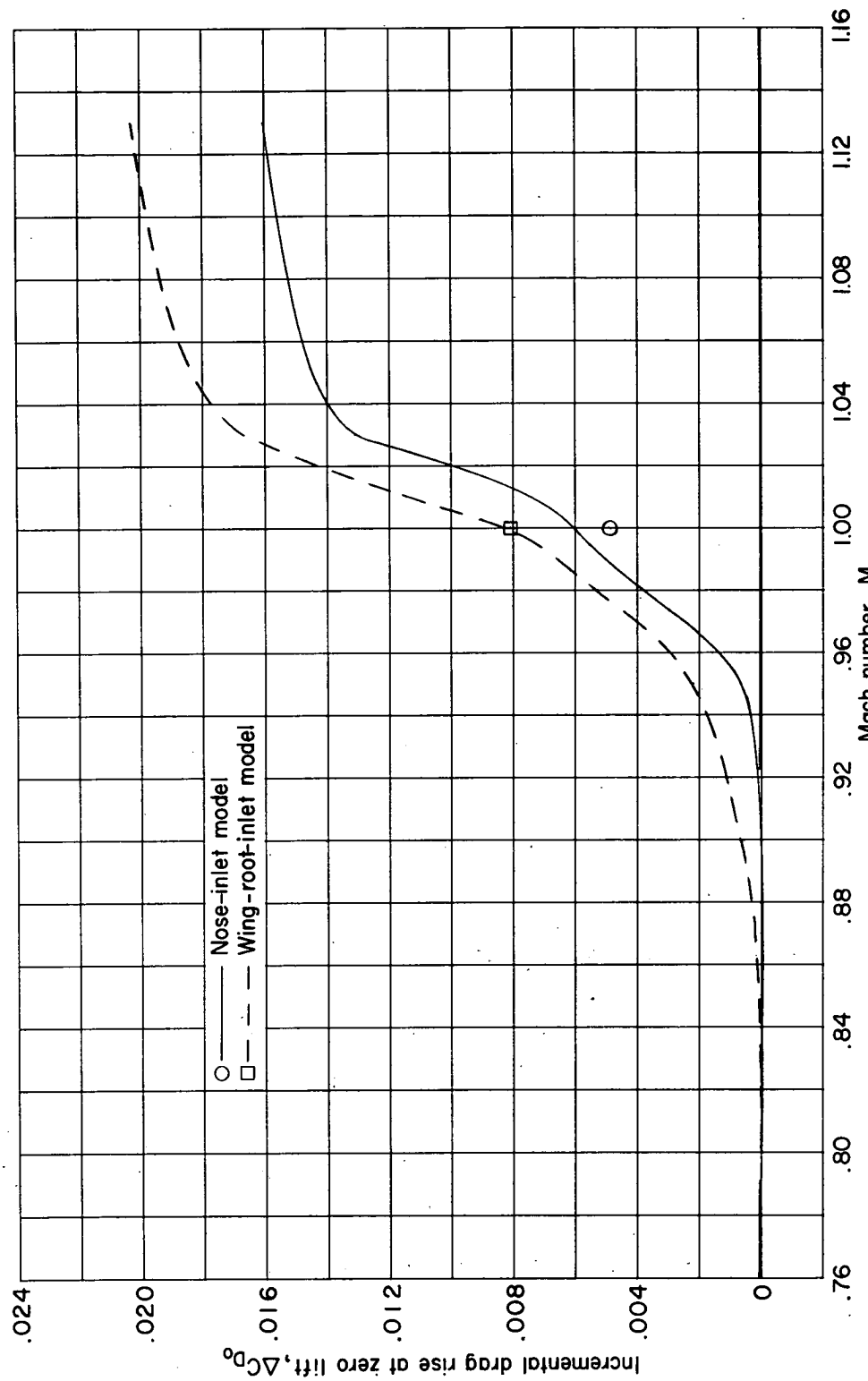

Figure 24.- A comparison of theoretical and experimental zero-lift drag-rise coefficient for the two models without wing-tip floats. (Template symbols represent theoretical data from ref. 12.)

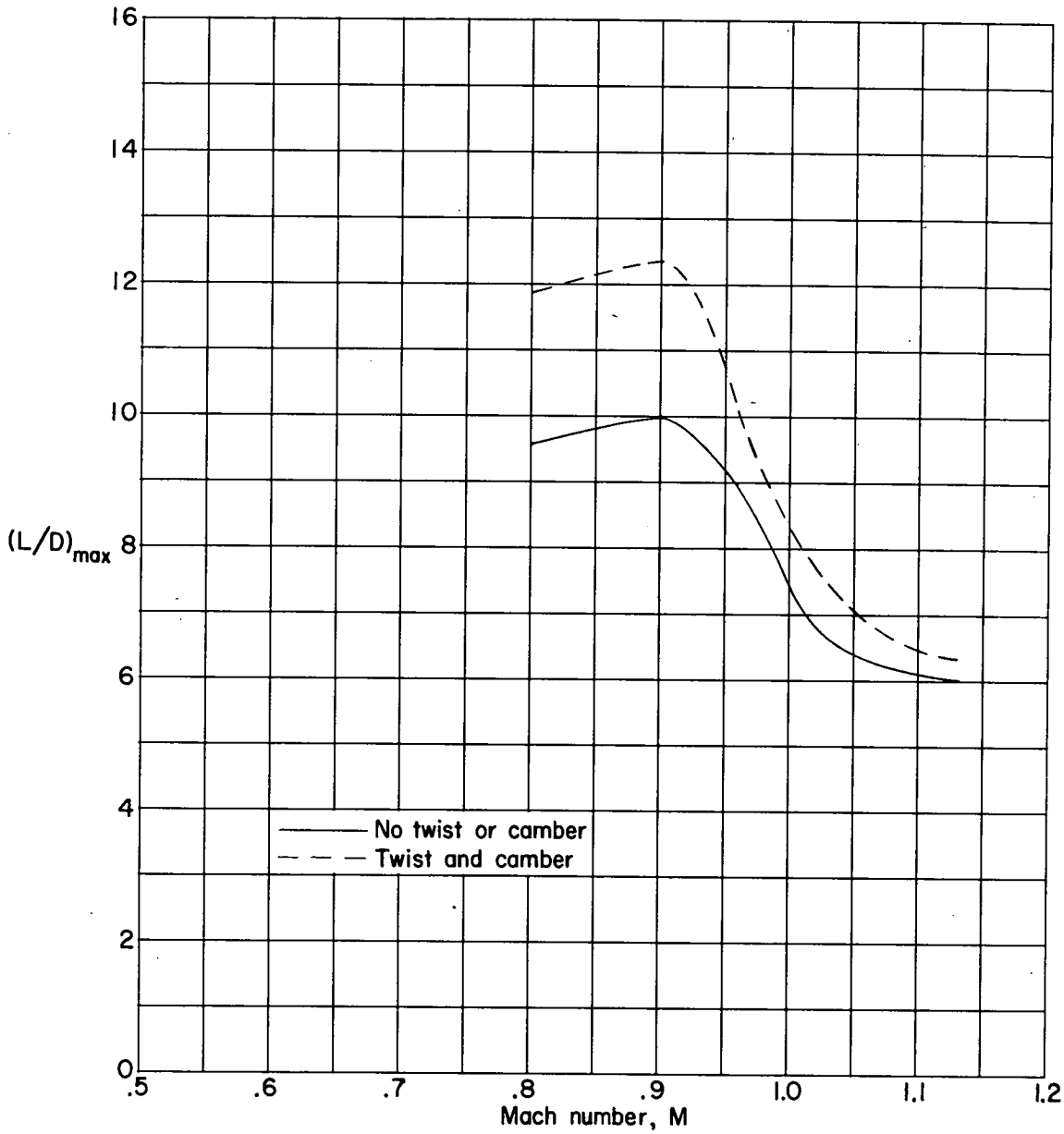

Figure 25.- Variation of maximum lift-drag ratio with Mach number for the nose-inlet configuration.

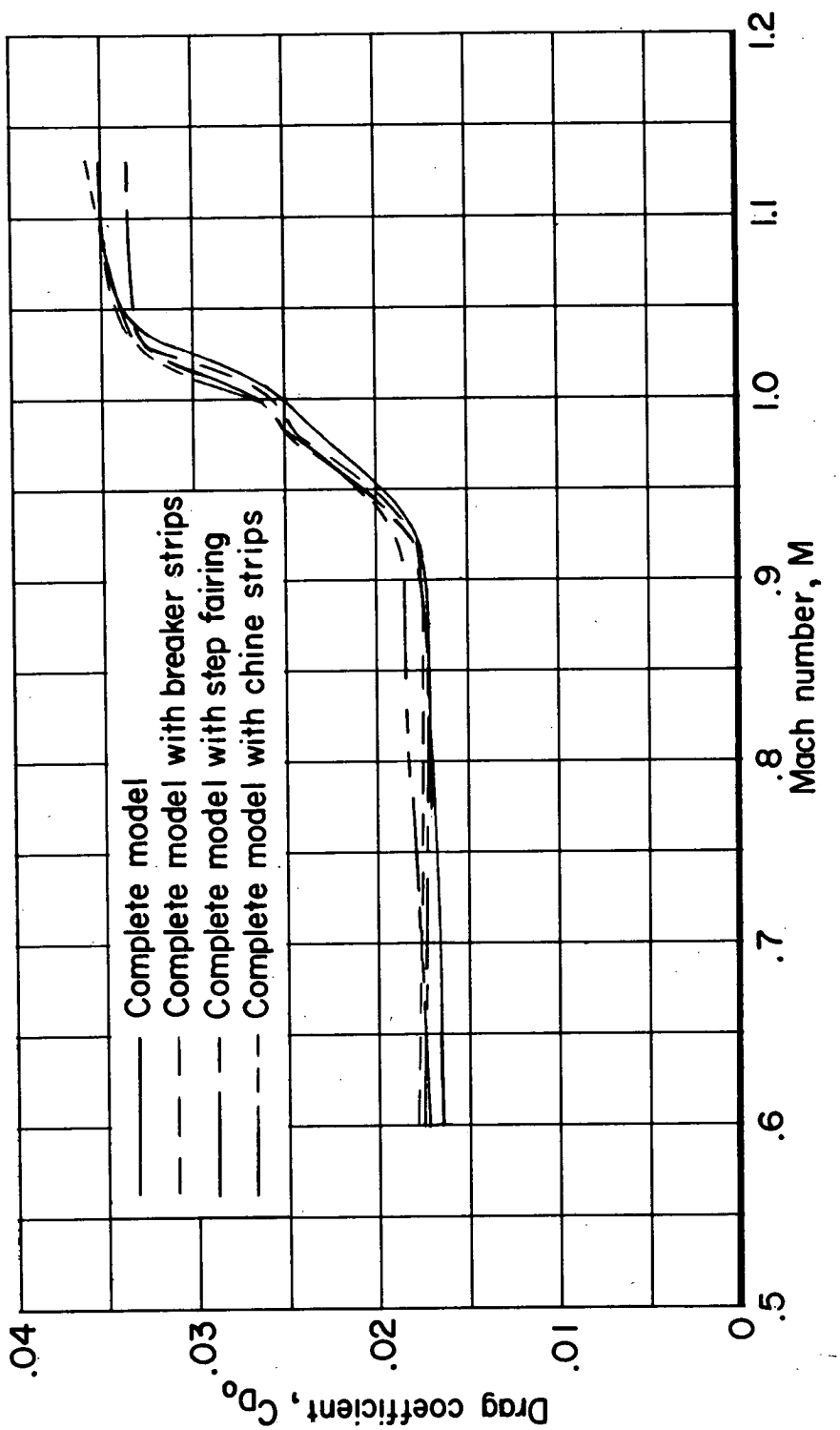

Figure 26.- A comparison of the zero-lift drag coefficients for the nose-inlet configuration with various modifications to hull.

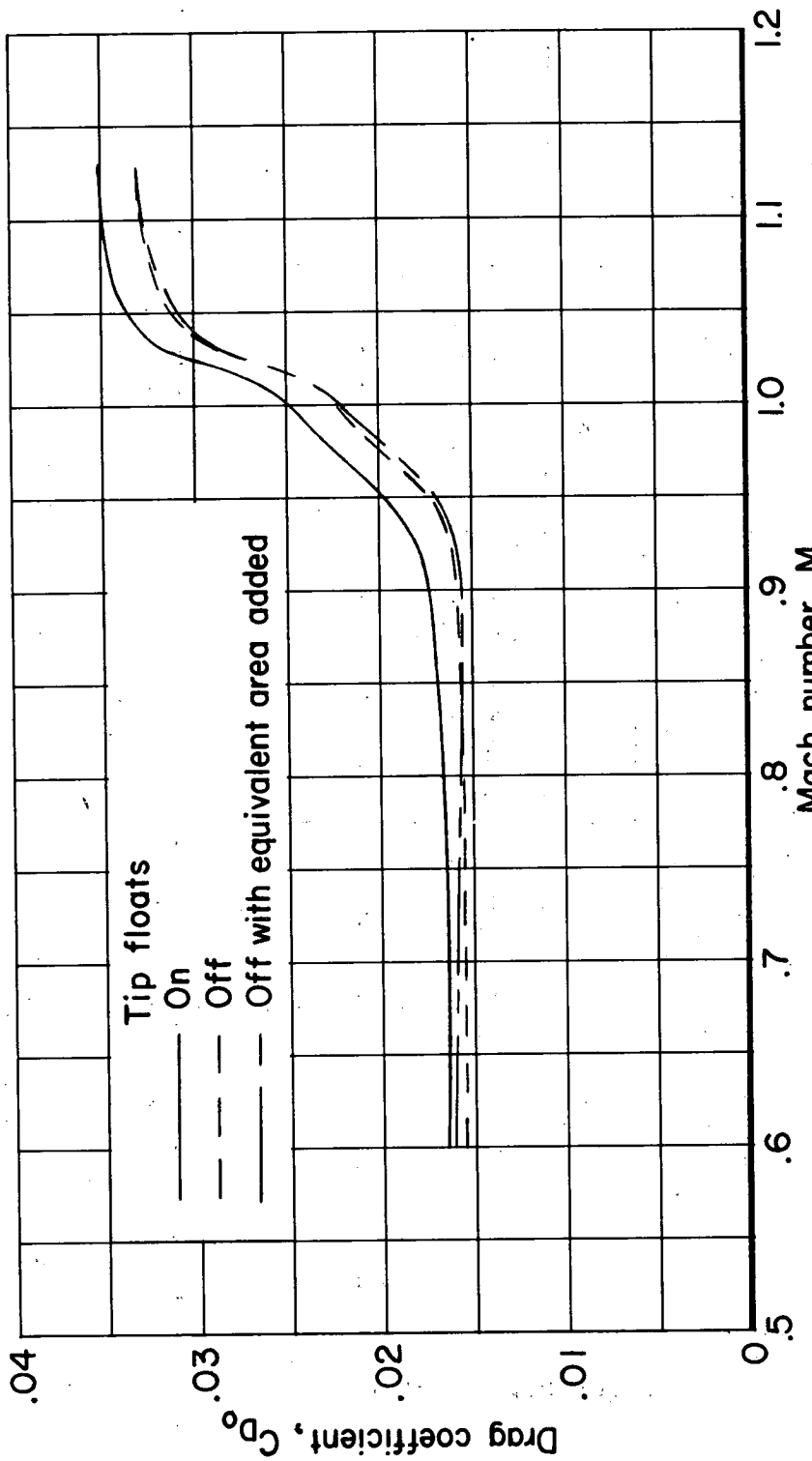

Figure 27.- A comparison of the zero-lift drag coefficients for the nose-inlet configuration with and without wing tip floats.

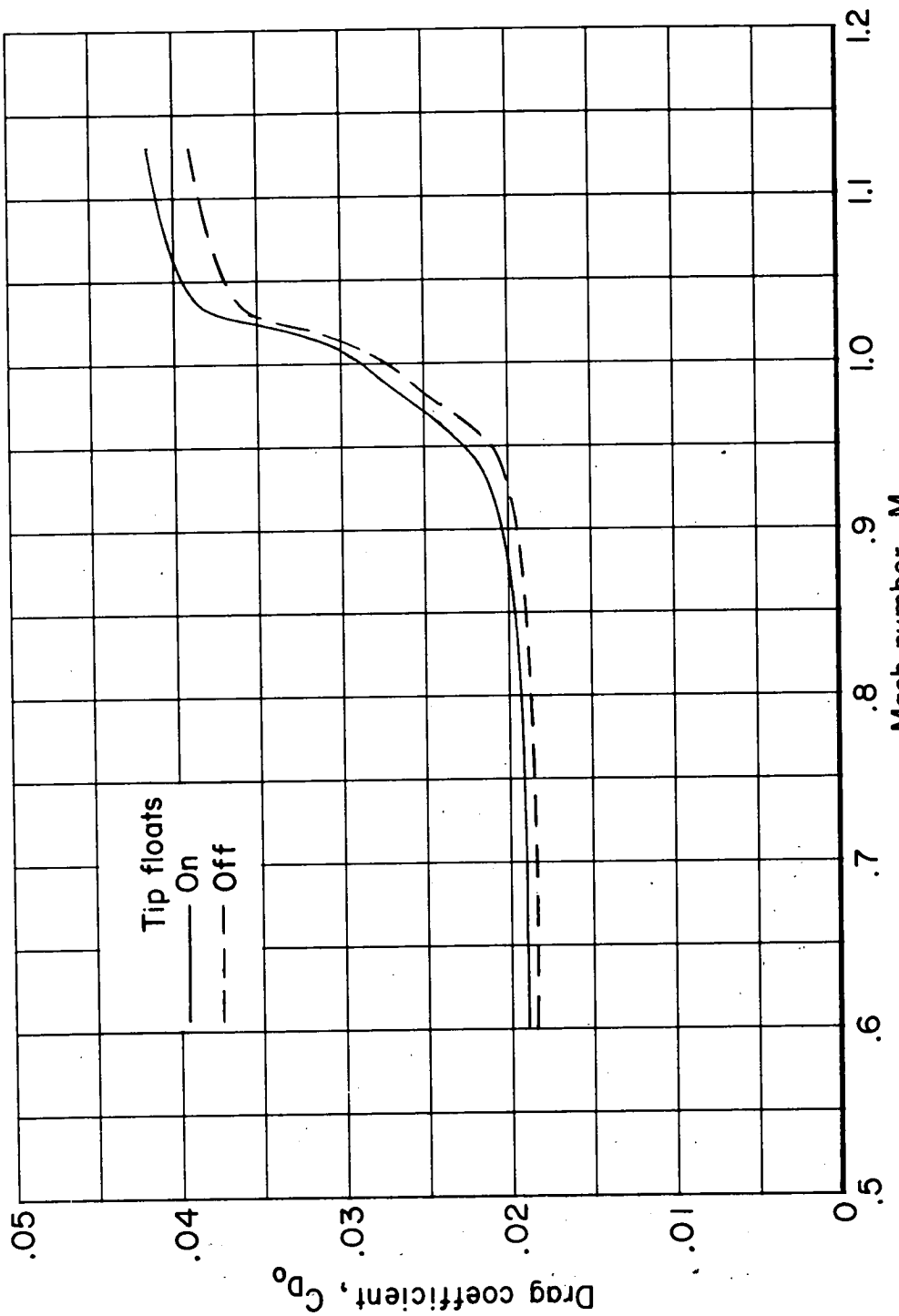

Figure 28.- A comparison of the zero-lift drag coefficients for the wing-root-inlet configuration with and without wing tip floats.

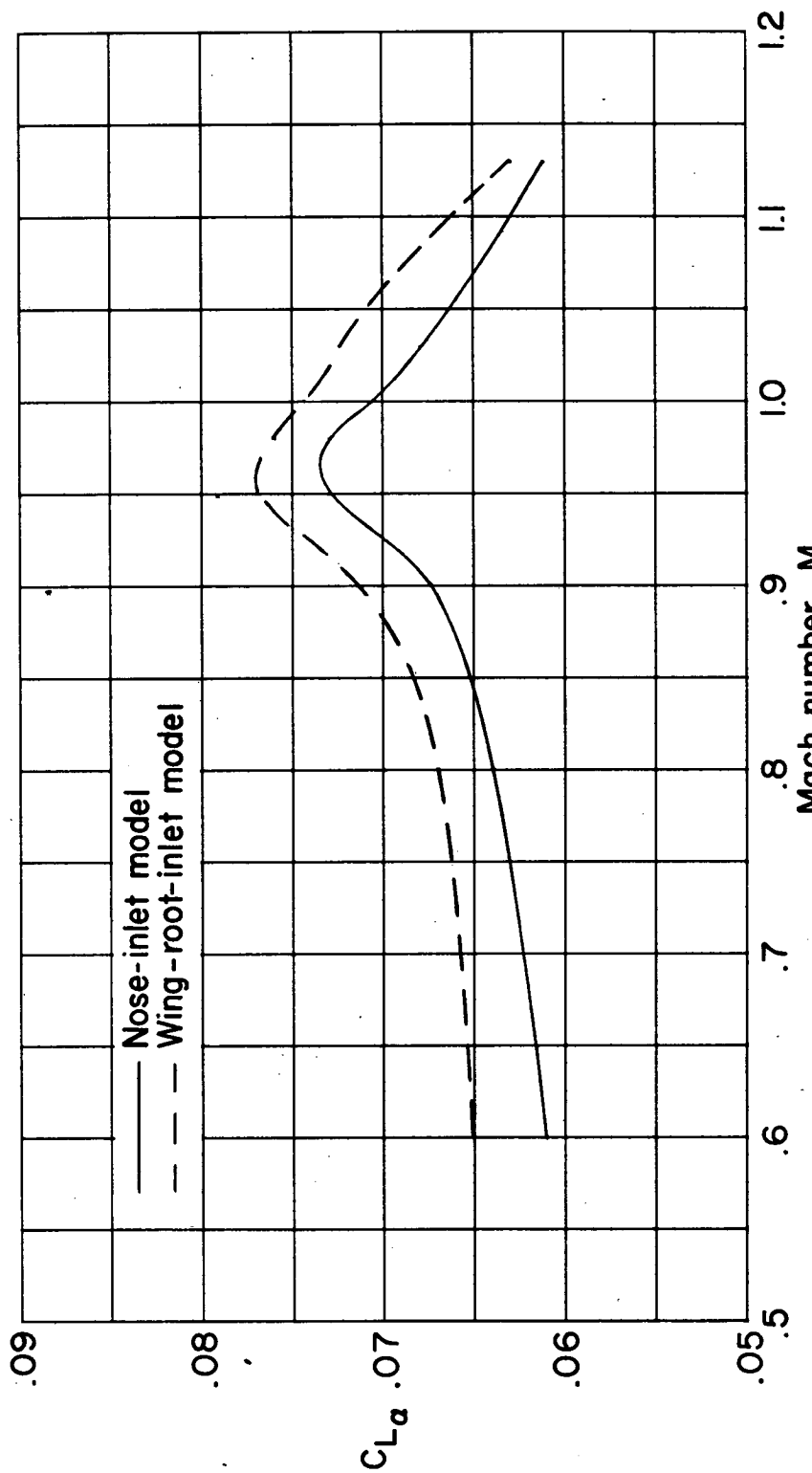

Figure 29.- A comparison of the lift-curve slopes of the two configurations.

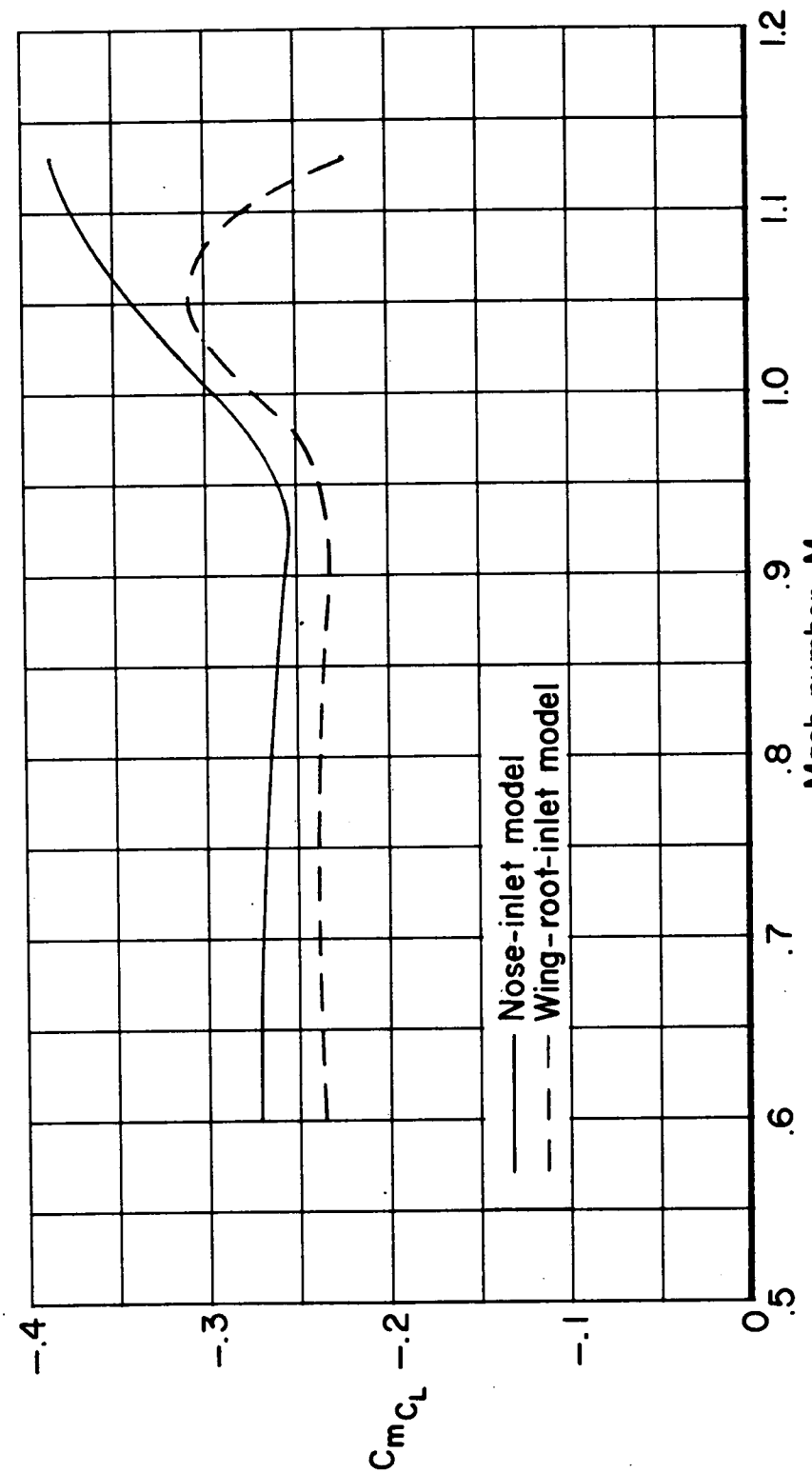

Figure 30.- A comparison of the pitching-moment-curve slopes of the two configurations.

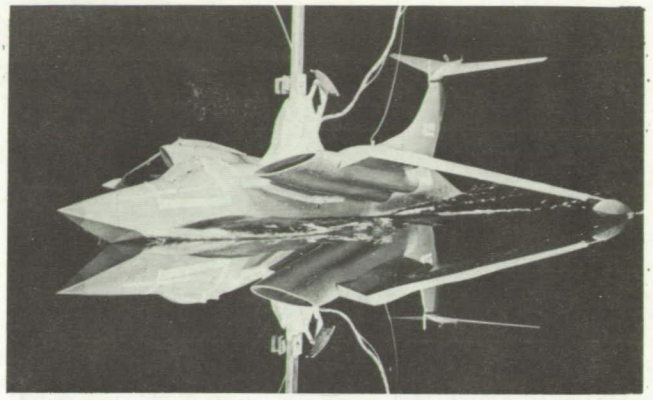

23.4 knots
$\gamma = 2.7^\circ$

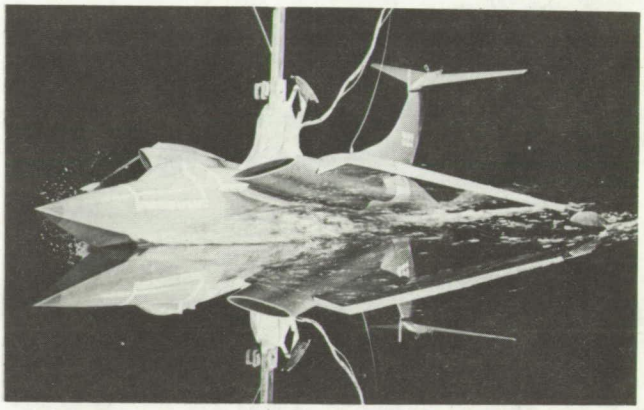

40.3 knots
$\gamma = 3.1^\circ$

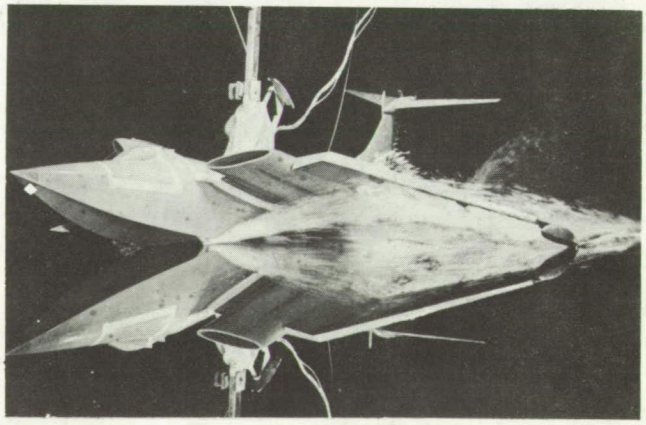

57.4 knots
$\gamma = 6.0^\circ$

L-87534

Figure 31.- Typical spray photographs, wing-root-inlet configuration. $\delta_f = 0^\circ$.

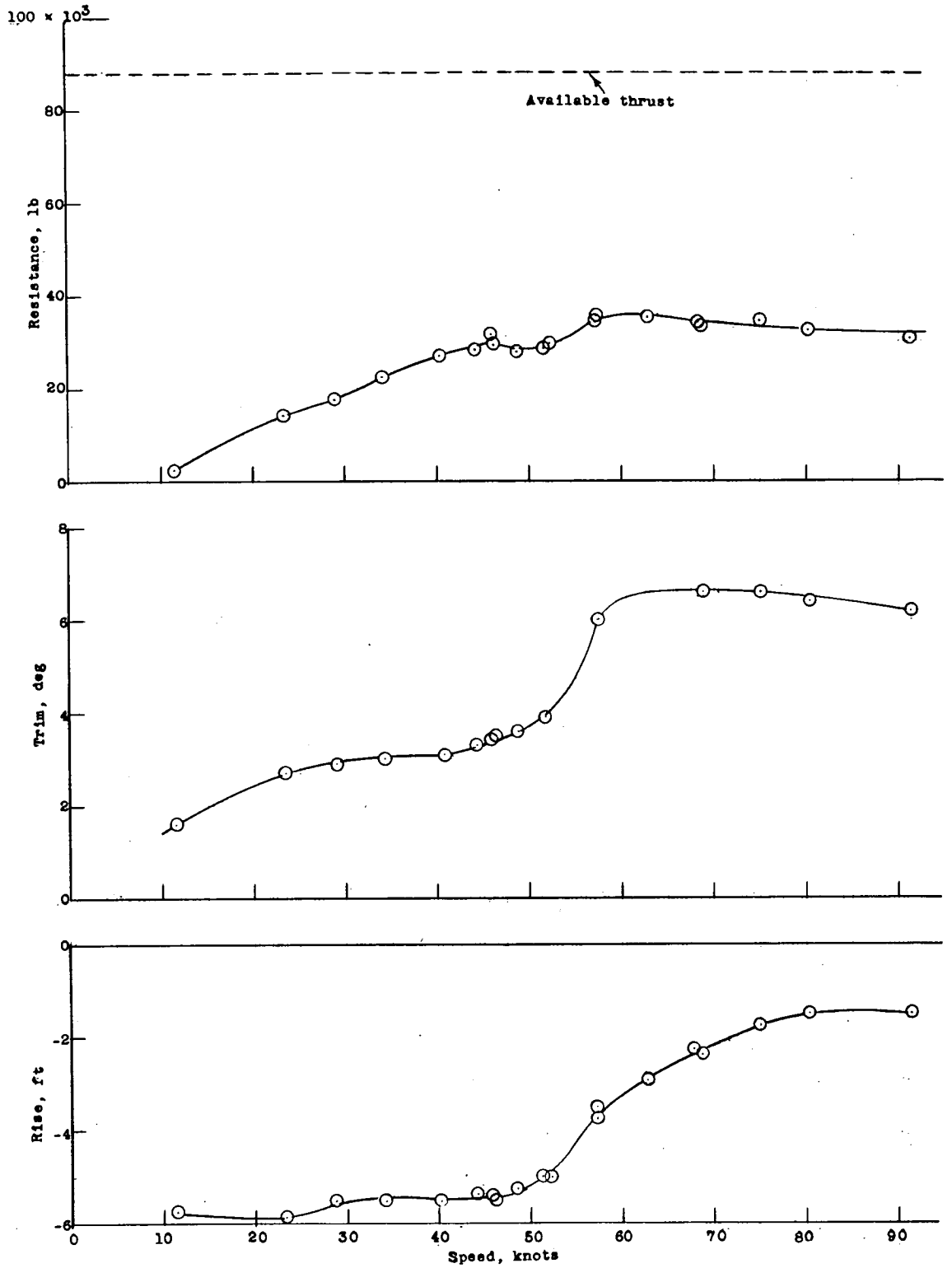

Figure 32.- Total resistance, wing-root-inlet configuration. $\delta_f = 0^\circ$; $\delta_e = 0^\circ$; $\delta_s = -13.5^\circ$.

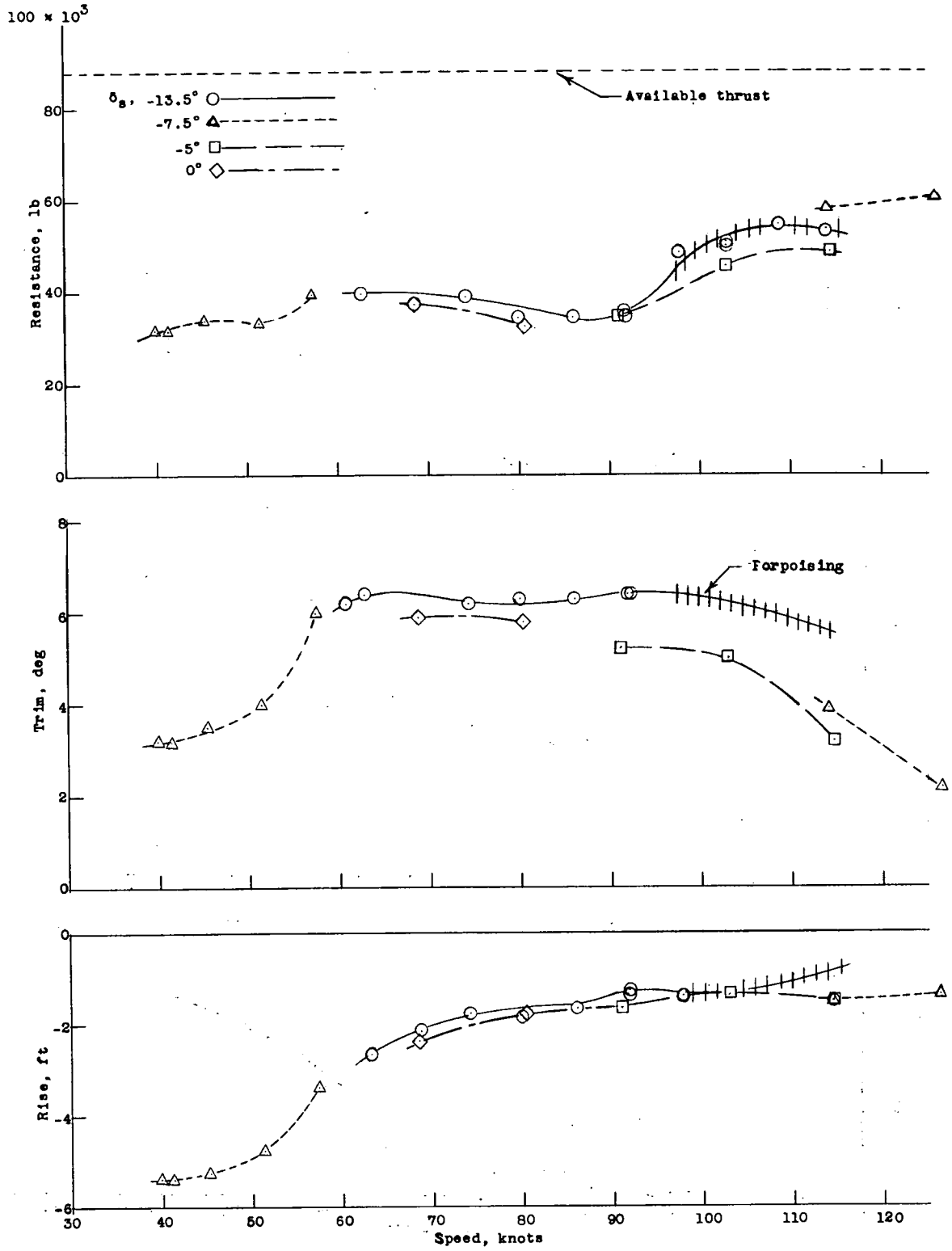

Figure 33.- Total resistance, wing-root-inlet configuration. $\delta_f = 50^\circ$; $\delta_e = -20^\circ$; c.g. = $0.32\bar{c}$.

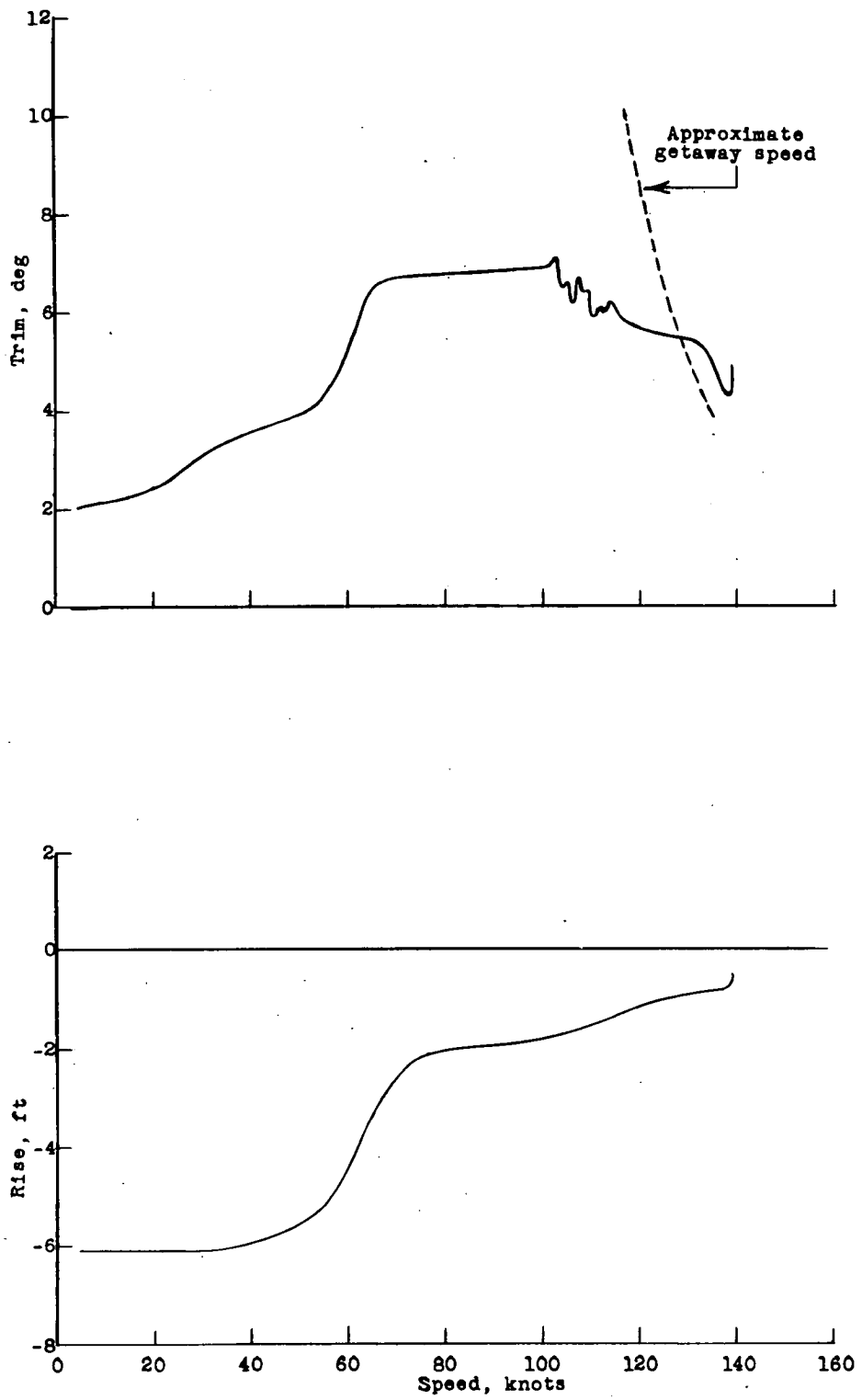

Figure 34.- Typical take-off, wing-root-inlet configuration. $\delta_f = 50^\circ$; $\delta_s = -7^\circ$.

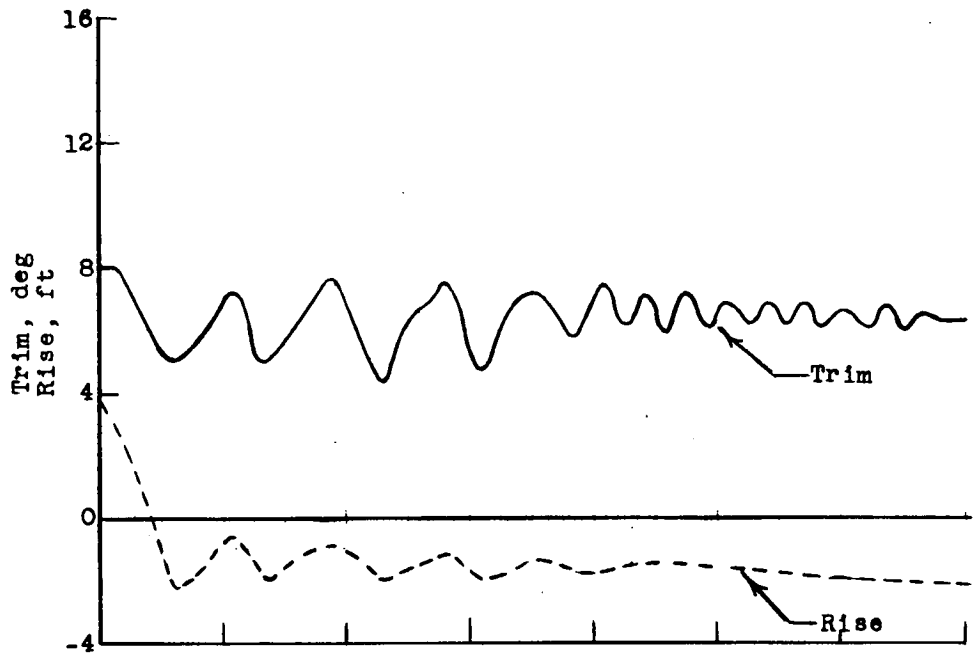

(a) Landing trim, 8°.

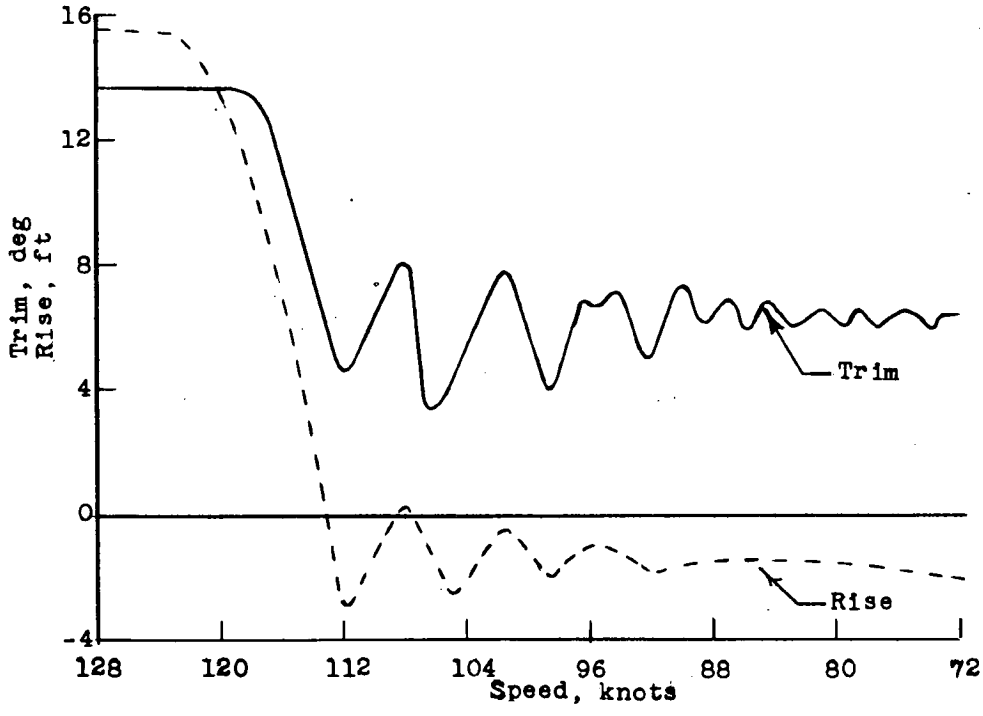

(b) Landing trim, 14°.

Figure 35.- Typical landings, wing-root-inlet configuration. $\delta_f = 50°$.

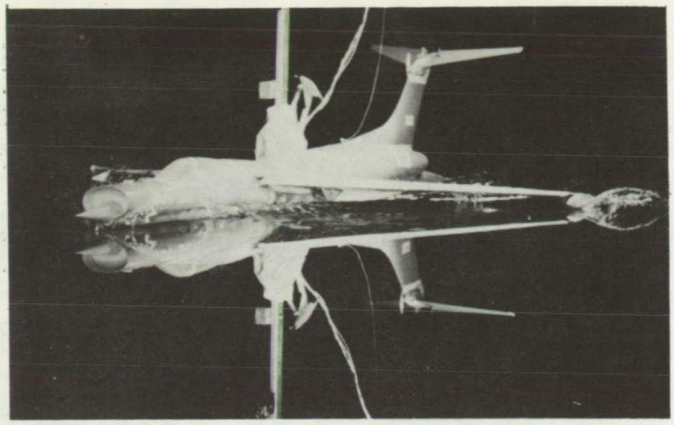

22.9 knots
$\gamma = 1.8^{\circ}$

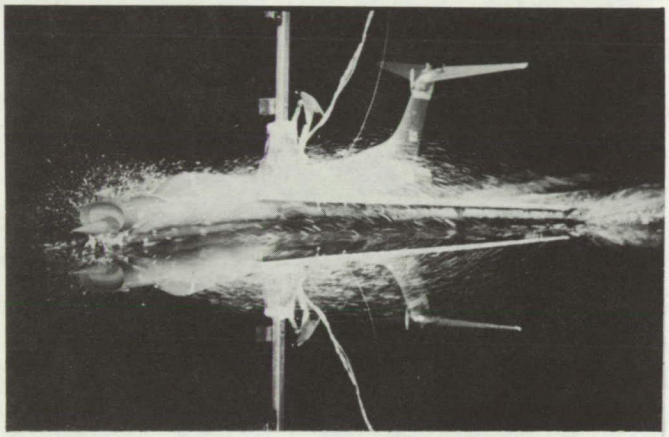

40.1 knots
$\gamma = 2.0^{\circ}$

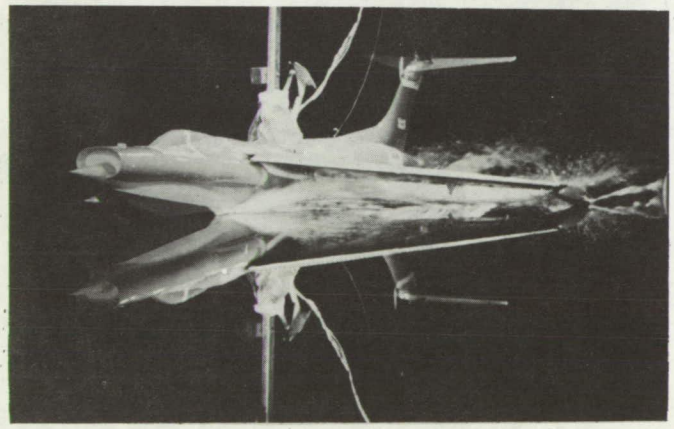

57.2 knots
$\gamma = 5.4^{\circ}$

L-87535

Figure 36.- Typical spray photographs, nose-inlet configuration. $\delta_f = 0^{\circ}$.

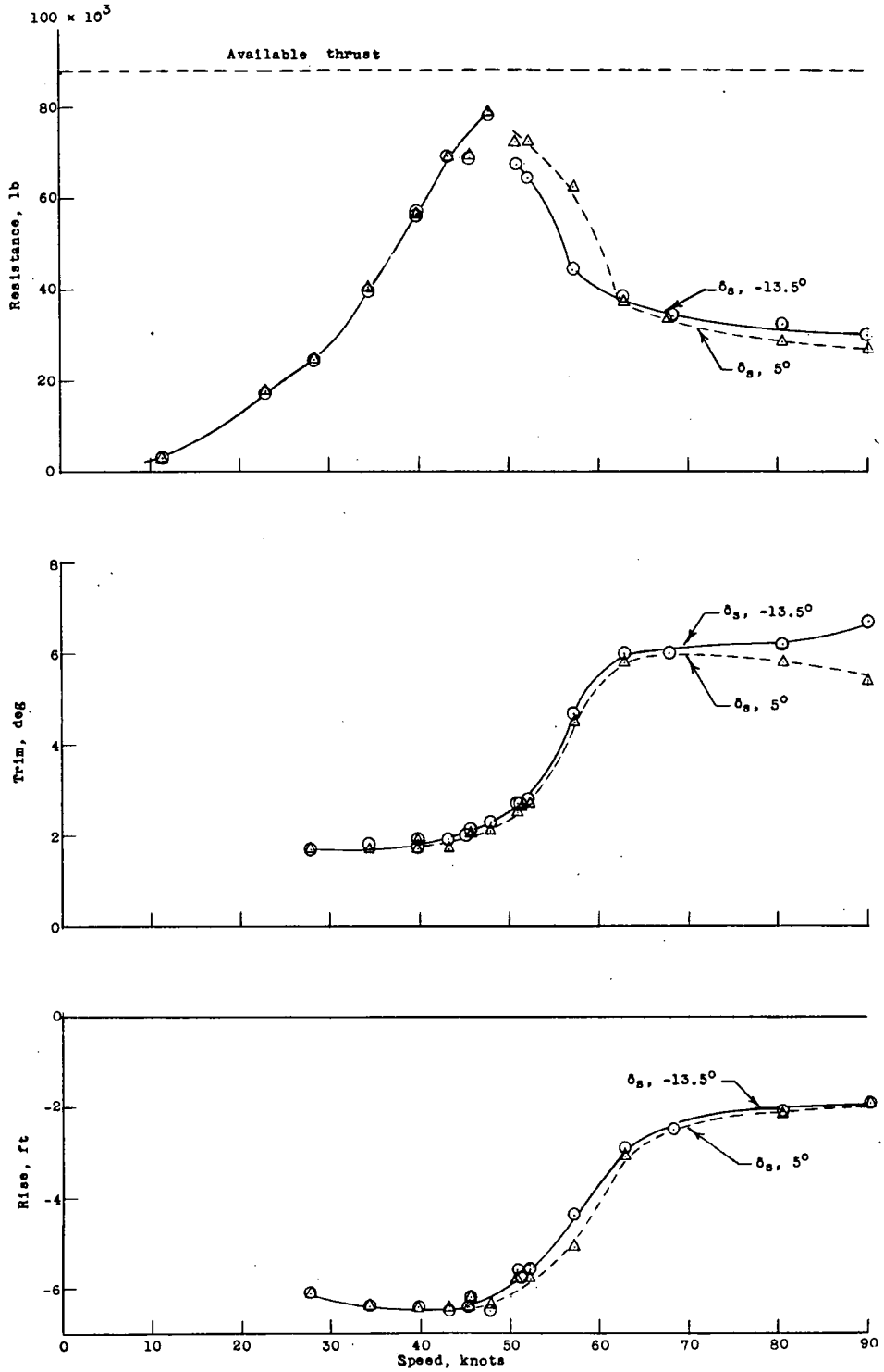

Figure 37.- Total resistance, nose-inlet configuration. $\delta_f = 0^\circ$; $\delta_e = 0^\circ$.

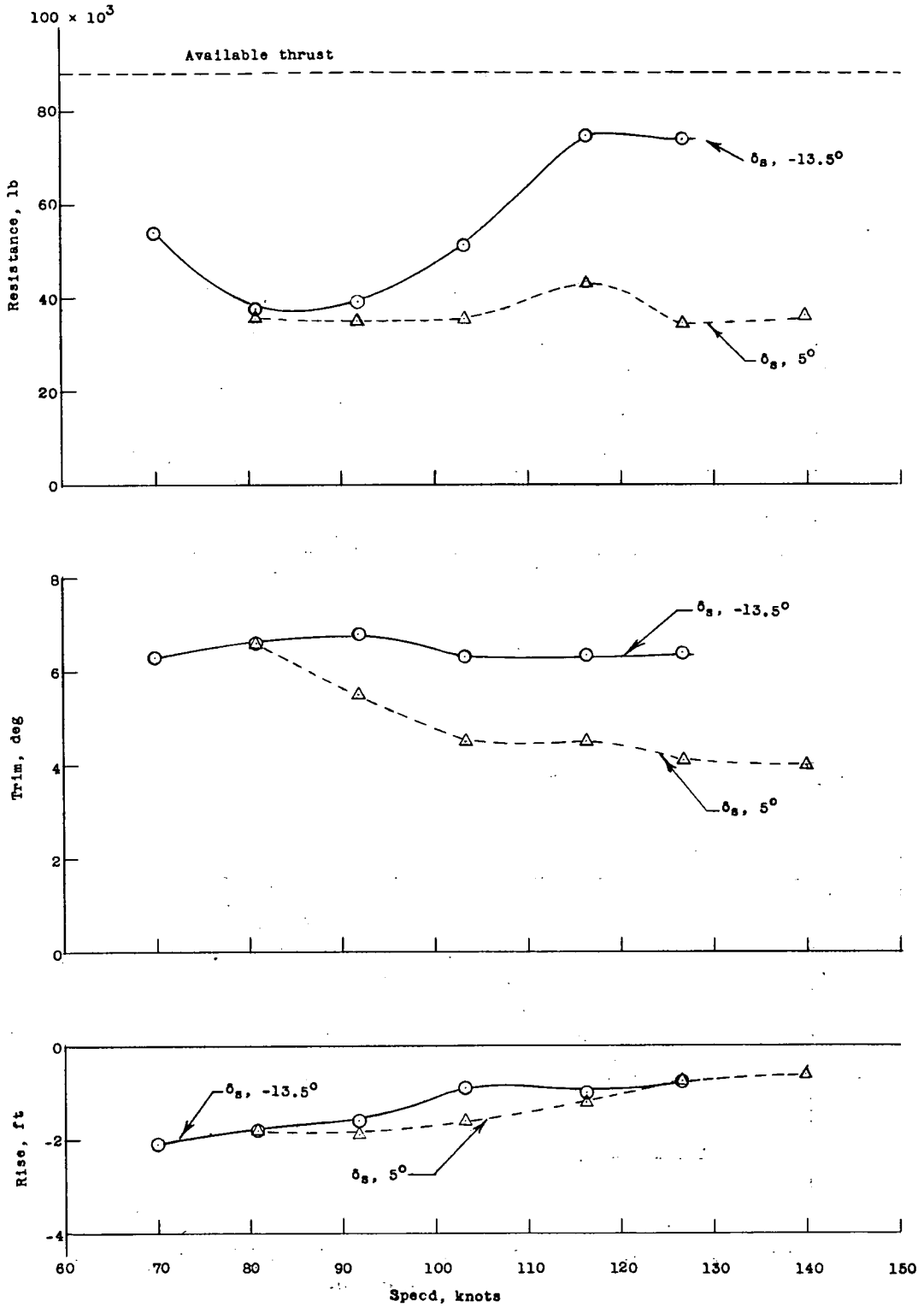

Figure 38.- Total resistance, nose-inlet configuration. $\delta_f = 40^\circ$; $\delta_e = -20^\circ$.

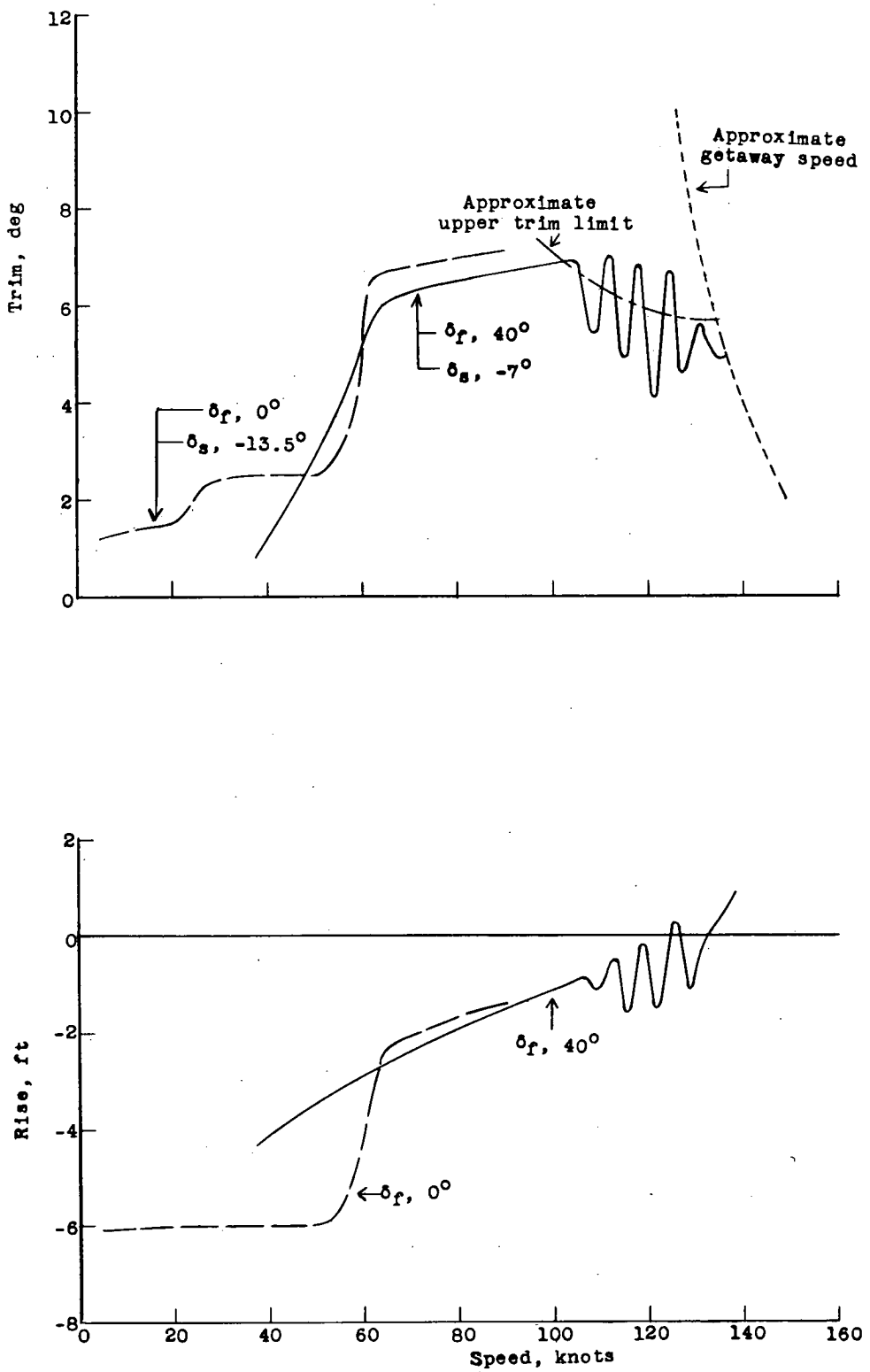

Figure 39.- Typical take-off, nose-inlet configuration.

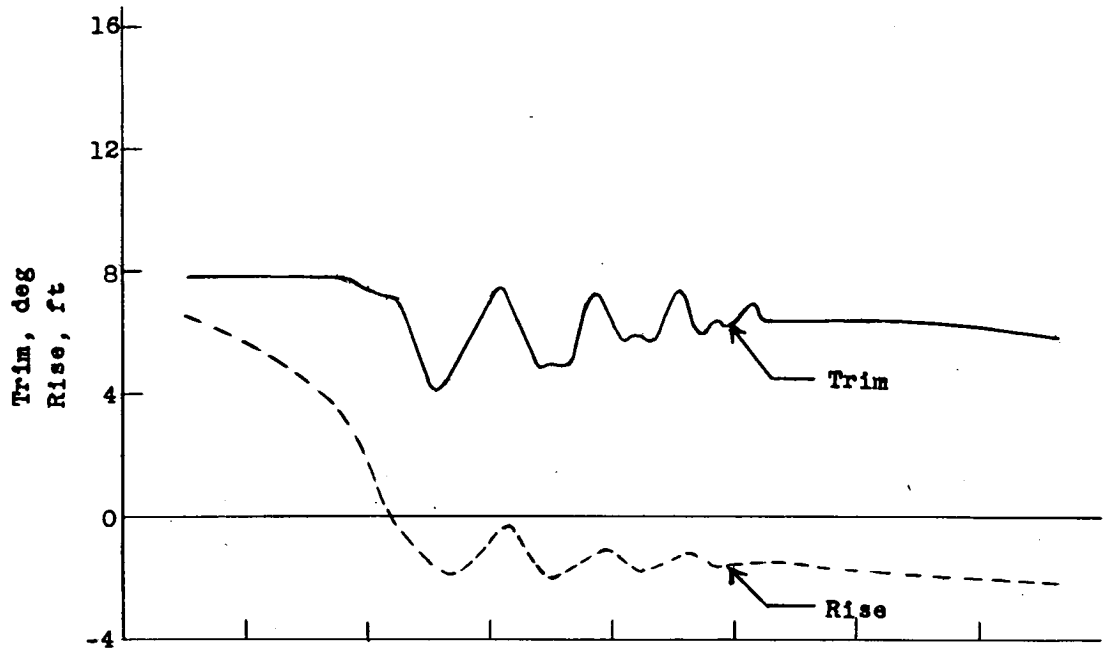

(a) Landing trim, 8°.

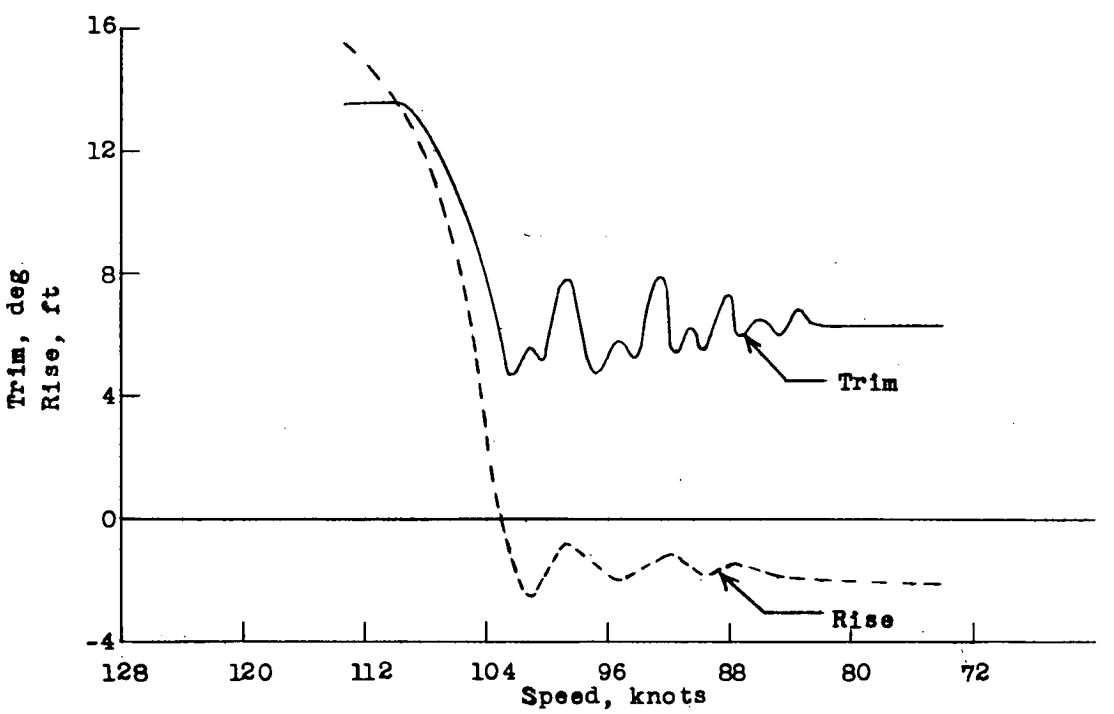

(b) Landing trim, 14°.

Figure 40.- Typical landings, nose-inlet configuration. $\delta_f = 40°$.